Robustness of O(5)/Spin(5) Quantum Numbers in the Interacting Boson (Fermion) Model in Selected Molybdenum and Gold Isotopes

Inaugural-Dissertation

zur

Erlangung des Doktorgrades

der Mathematisch-Naturwissenschaftlichen Fakultät

der Universität zu Köln

vorgelegt von

Tim Thomas

aus Wetzlar

Köln 2014

Berichterstatter: Prof. Dr. Jan Jolie
Prof. Dr. Andreas Zilges

Tag der mündlichen Prüfung: 27.05.2014

Zusammenfassung

Die Beschreibung der Kernstruktur von mittelschweren bis schweren Atomkernen stellt eine große Herausforderung an theoretische Modelle dar. Die große Anzahl und die Komplexität von Nukleon-Nukleon Wechselwirkungen macht insbesondere die Beschreibung von Atomkernen fernab von Schalenabschlüssen sehr schwierig. Um dennoch Aussagen über die Struktur solcher Kerne machen zu können spielen Symmetrieüberlegungen, die zu Verkleinerung des Modellraums führen, eine wichtige Rolle. Im Rahmen dieser Arbeit wurden die gerade-gerade Molybdän Isotope ^{96}Mo und ^{98}Mo, sowie die ungerade-gerade Gold Isotope ^{193}Au und ^{195}Au in Hinblick auf die Erhaltung ihrer O(5) und Spin(5) Quantenzahlen untersucht. Insgesamt wurden dafür vier Experimente an den Tandembeschleunigern der kernpysikalischen Institute in Köln und New Haven durchgefürt.

Die Untersuchung von ^{96}Mo und ^{98}Mo zeigte Signaturen, die mit shape coexistence in Verbindung gebracht werden. Basierend auf mikroskopischen Modellen wurden Berechnungen im Rahmen des Interacting Boson Model 2 durchgeführt, die eine starke Mischung einer vibrationell ähnlichen Konfiguration und einer γ-instabil ähnlichen Konfiguration ergaben. Dies wurde experimentell durch die Quadrupolmomente und β-Deformationen der tiefliegenden 2^+ Zustände bestätigt. Aufgrund der guten Übereinstimmung wurde das verwendete IBM-2 Modell auf den Nachbarkern ^{96}Mo angewendet. Hierbei wurden sowohl Rechnungen mit einer Konfiguration, als auch mit Konfigurationsmischungen durchgeführt. Der Vergleich dieser Rechnungen könnte darauf hinweisen, dass zum Verständnis dieses Kerns shape coexistence notwendig ist. Desweiteren erlauben die Proton-Neutron Freiheitsgrade das Phänomen der gemischt symmetrischen Zustände zu untersuchen. Wegen der strengen O(5) Auswahlregeln, die mit Übergängen dieser Zustände verbunden sind, konnte die Erhaltung der O(5) Quantenzahlen überprüft werden.

Die ungerade-gerade Gold Isotope ^{193}Au und ^{195}Au wurden auf Erhaltung der Spin(5) Quantenzahlen, hervorgerufen durch die Bose-Fermi Symmetrie, untersucht. Insgesamt zeigen die angeregten Zustände und Übergangsstärken einen gleichmäßigen Verlauf, in den sich die Ergebnisse der Experimente gut einfügen. Unter Verwendung der Eigenfunktion der Bose-Fermi Symmetrie lässt sich der Verlauf durch lediglich vier Parameter darstellen.

Abstract

The nuclear structure of medium and heavy nuclei represent a huge challenge for theories dealing with nucleon-nucleon interactions. The large number and the complexity of nucleon-nucleon interactions make the description of nuclei far away from closed shells rather difficult. In order to understand the structure of such nuclei, symmetry considerations leading to a reduction of the model space play a major role.

In this work the even-even molybdenum isotopes ^{96}Mo and ^{98}Mo and the odd-even gold isotopes ^{193}Au and ^{195}Au were investigated with special regard to the goodness of the O(5) and Spin(5) quantum numbers. Therefore, four in-beam experiments have been performed at the tandem accelerator facilities in Cologne (IKP) and in New Haven (WNSL).

The investigation of ^{96}Mo and ^{98}Mo revealed that these nuclei exhibit complex nuclear structures associated with shape coexistence. Based on microscopic considerations the calculations of ^{98}Mo in the framework of the Interacting Boson Model 2 showed a strong mixing of a U(5)-like normal configuration and an O(6)-like intruder configuration. This is experimentally confirmed by quadrupole moments, and the β deformation of the first excited 2^+ states. The successful calculation of ^{98}Mo was extended to ^{96}Mo. The comparison of calculations with single configuration and configuration mixing indicated that the nuclear structure of ^{96}Mo can be understood in terms of shape coexistence. The neutron-proton degree of freedom of the IBFM-2 allowed to understand the mixed symmetry states in the vicinity of configuration mixing and offered a crucial test for the goodness of the O(5) quantum number.

In the framework of the Interacting Boson Fermion Model ^{193}Au and ^{195}Au were investigated to test the goodness of the Spin(5) quantum numbers induced by the Bose-Fermi symmetry. The obtained data of the low spin states in ^{193,195}Au fits well to the overall smooth evolution of level energies and transition strengths in the odd-even gold isotopes. This allows to use a simple four-parameter expression based on the eigenfunction of the Bose-Fermi symmetry to describe more than 54 states confirming the conservation of the Spin(5) quantum number.

Contents

Chapter 1

Introduction

> "Since the beginning of physics, symmetry considerations have provided us with an extremely powerful and useful tool in our effort to understand nature."
> — Tsung-Dao Lee [1]

Since the fundamental work from Emmy Noether which is known as Noether's theorem [2] we recognize the encompassing importance of symmetries and the conservation laws associated with symmetries. The Noether's theorem formulates, that for every transformation which leaves a system unchanged, an observable exist which is preserved. One conclusion is that in contained, isotropic physical systems the energy, momentum and angular momentum is preserved. In classical mechanics, this is expressed by $\{f, H\} + \delta f/\delta t = 0$, so the Poisson bracket of an observable f and a Hamiltonian H together with the partial differentiation of the observable in time t equals to zero. In this case the observable f is conserved in terms of the constants of motion. In quantum mechanics, the Poisson bracket is replaced by the Commutator $\{f, H\} \rightarrow -i/\hbar[\hat{f}, \hat{H}]$, where observables are now operators and the Ehrenfest Theorem must be fulfilled for the operator to be a constant of motions [3].
In quantum mechanics, the concept of symmetries introducing invariants is of major importance. On the very basic level of particle physics, these symmetries hint on fundamental laws in nature. In the following table 1.1, an example of conserved quantum numbers are given, together with the group associated with the invariant transformation [4]. One interesting aspect of some examples given in table 1.1 is, that while the symmetry might be broken, the quantum numbers are still preserved. A famous example for this is the isospin. Based on the discovery of neutrons [5, 6] and the almost identical mass between protons and neutrons, Werner Heisenberg [7] introduced the concept that protons and

conserved quantity	invariance
conservation of charge C	U(1)
conservation of the number of baryons B	SU(3)
conservation of the number of leptons L	U(1)
conservation of color	SU(3)
cnoservation of isospin I	SU(2)

Table 1.1: conservations of quantum numbers and the associated groups

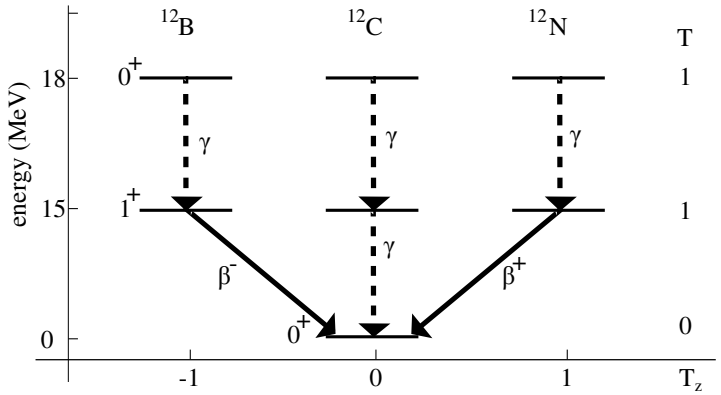

Figure 1.1: A schematic figure showing degenerate states with same isospin for ^{12}C and its isobaric neighbors.

neutrons share the same spin $1/2$ but have different projections. This concept is based on the assumption, that the nuclear force does not distinguish between the two particles and thus is invariant with respect to transformations from neutrons to protons.

Here, briefly some concepts essential for this thesis are introduced on the example on isospin, which are discussed in much more detail in Ref. [8,9]. One can define infinitesimal transformations between a proton and neutron by the operators $\hat{t}_x$, $\hat{t}_y$, $\hat{t}_z$, which fulfill the following relations $[\hat{H}, \hat{t}_z] = [\hat{H}, \hat{t}_\pm] = 0$ and $[\hat{t}_i, \hat{t}_j] = 2i\epsilon_{ijk}\hat{t}_k$, where $\hat{t}_z$ is the infinitesimal transformation around a specific axis z and $\hat{t}_\pm = \hat{t}_x \pm i\hat{t}_y$ the raising and lowering operator and $i, j, k = x, y, z$. These expressions can be expanded for more Nuclei, in which case the total isospin operator $\hat{T}$ and its projection ($\hat{T}_z$) to the z-axis $M_T = (Z - N)/2$, with Z being the number of protons and N the number of neutrons. The operators together with the commutator form the Lie-algebra SU(2). Since there is a direct relationship between the terms "Lie-algebra" and "group" within this thesis, these terms are used synonymously. The interesting aspect of the SU(2) algebra associated with isospin is, that the SU(2) algebra is isomorphic to the O(3) algebra, which gives rise to angular momentum quantum number.

The importance of the isospin formalism is easily observed on the example of

$^{12}_{6}$C^{6} [10]. From the independent shell model perspective, the ground state of ^{12}C is formed by 4 protons and 4 neutrons in a $p_{3/2}$ orbital ahich are coupled to spin 0. For convenience only a two nucleon system is considered . Together, they can form states associated with T =0, 1. As a antisymmetric T=0 state is energetically favored, the ground state has T=0, while another state with spin 0 and T=1 must exist at higher energies as well as T=1 states with higher spin. In the neighboring isobaric nuclei $^{12}_{7}$N^{5} and $^{12}_{N}$B^{7} the first excited state with spin 0 is associated with isospin T=1. This is schematically shown in Fig. 1.1, where energy (excitation energy and binding energy) of the states are plotted relative to the ground state in ^{12}C. The degenerate energies of the T=1 triplet states suggest, that the nuclear force can be assumed to be charge independent in the first order and the isospin a conserved quantity. This is confirmed by inelastic scattering experiments with deuterons on ^{12}C. A deuteron with isopin T=0 cannot excite the ground state T=0 to excited T=1 states without breaking isospin conservation, thus this reaction is isospin forbidden [11].
As mentioned before, the electromagnetic interaction breaks the isospin symmetry, so states with the same T quantum number in different nuclei are not degenerate as shown schematically in Fig. 1.1. Using first order perturbation theory to estimate the energy shift of a given state $|\eta T T_z\rangle$ (with η being an additional label to distinguish states with same T, T_Z), one can calculate the diagonal matrix elements and rewrite the Coulomb interaction to [8]

$$V \approxeq \hat{V} \equiv \kappa_0 + \kappa_1 \hat{T}_z + \kappa_2 \hat{T}_z^2, \tag{1.1}$$

This way, even while the symmetry induced by the SU(2) algebra is broken, its quantum number T is retained. Analogue to the expression in Eq. (1.1), this can also be written in terms of nested algebras:

$$\begin{array}{ccc} \text{SU(2)} & \supset & \text{SO(2).} \\ [T] & & [M_T] \end{array} \tag{1.2}$$

with the eigenfunction

$$E(M_T) = \kappa_0 + \kappa_1 M_T + \kappa_2 M_T^2. \tag{1.3}$$

The constructed algebraic chain given in Eq. (1.2) forms a dynamical symmetry, and M_T follows the reduction rule $M_T = -T, ..., T$. Equation (1.3) can now be applied to predict the binding energy (hence mass) of an isospin triplet, if parameters κ_0, κ_1, κ_2 are known. Thus, Eq. (1.3) is also called the isobaric-

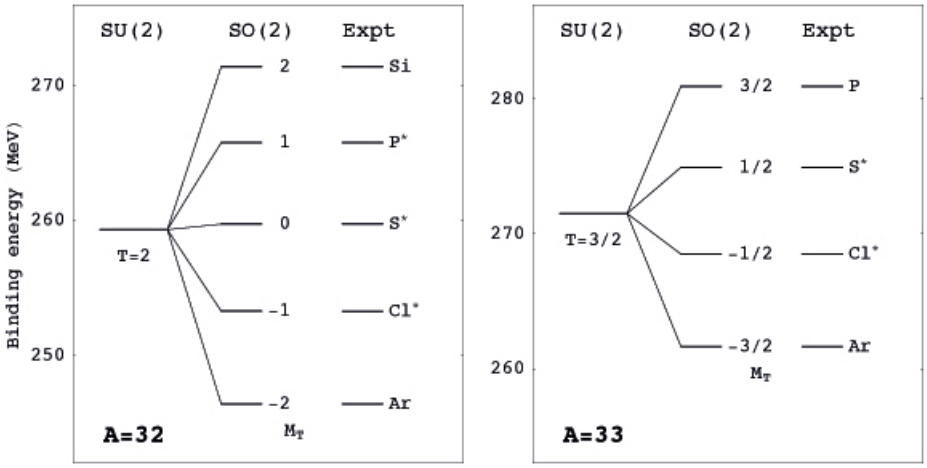

Figure 1.2: A schematic figure showing the splitting of degenerate states with the same isospin T=1 and T=3/2 in terms of binding energies. This figure is adopted from Ref. [8].

multiplet mass equation (IMME) and was first proposed by Wigner [12]. Figure 1.2 shows an example for the splitting of the T=2 multiplet (on the left hand side) and the T=3/2 multiplet (on the right hand side). Experimental data was taken from Refs. [13, 14] and are reproduced within an error of 1 keV. So the isospin quantum number is still preserved, even though a breaking of the symmetry occurs. This is called "dynamical symmetry" breaking. Operators, which produce such a symmetry breaking are called Casimir operators.

1.1 IBM

The concept of symmetry breaking is also applied in the Interacting Boson Model (IBM-1). A just brief introduction is given here. For detailed information, the interested reader is referred to Ref. [9, 15–18].
The prediction of calculated states tend to become uncomputable for microscopic models (ie. shell model [19–21]) with increasing mass A and away from the so-called magic numbers. Especially the Geometric Collective Model (GCM) [22, 23] and its simplifications turned out to be successful for nuclei exhibiting substantial deformation. The geometric model deals with the collective motion of nucleons in type of surface vibrations and rotations rather than with the individual nucleon. While this models describes rotational bands of deformed nuclei with a large set of nucleons accurately, problems arise for

nuclei situated closer to shell closure. The IBM-1 is motivated to account for both approaches. To avoid computational problems, the number of nucleons are drastically reduced by considering only valence nucleons. Using a concept well known in solid state physics, the number of nucleons is still reduced by combining nucleon pairs to so-called Cooper pairs (BCS pairs) [24, 25] with angular momentum $l = 0$ (s bosons) and $l = 2$ (d bosons). In second quantization, the corresponding boson creation and annihilation operators can be used to construct the generators of a U(6) algebra. Note, the IBM-1 does not distinguish between proton bosons and neutron bosons. The possibilities to form a chain of nested algebras is limited, since it is sensible to require that the angular momentum is conserved. Only three algebra chains can be formed:

$$
\begin{array}{lccccccc}
 & \mathrm{U}(6) & \supset & \mathrm{U}(5) & \supset & \mathrm{O}(5) & \supset & \mathrm{O}(3) \\
\mathrm{U}(5) - Symmetrie: & \downarrow & & \downarrow & & \downarrow & & \downarrow \\
 & [N] & & \{n_d\} & & (\nu) & & L
\end{array}
$$

$$
\begin{array}{lccccc}
 & \mathrm{U}(6) & \supset & \mathrm{SU}(3) & \supset & \mathrm{O}(3) \\
\mathrm{SU}(3) - Symmetrie: & \downarrow & & \downarrow & & \downarrow \\
 & [N] & & (\lambda, \mu) & & L
\end{array}
$$

$$
\begin{array}{lccccccc}
 & \mathrm{U}(6) & \supset & \mathrm{O}(6) & \supset & \mathrm{O}(5) & \supset & \mathrm{O}(3) \\
\mathrm{O}(6) - Symmetrie: & \downarrow & & \downarrow & & \downarrow & & \downarrow \\
 & [N] & & \{\Sigma\} & & (\tau) & & L
\end{array}
$$

These algebraic chains are also called dynamical limits. As already discussed for the isospin, the symmetry of the embedding algebra can be broken by the Casimir operators of the nested algebra. However, the Casimir operators of the nested algebras commute with the embedding algebra, thus the quantum numbers are preserved. The Hamiltonians of the dynamical limits can be written amongst others (multipole form) as linear combination of Casimir operators, allowing to use eigenfunctions to determine the energy for a given set of quantum numbers associated with that state.
The nuclei discussed in this thesis don't exhibit strong deformation of the nuclear shape, so the SU(3) limit will be neglected. Instead, the focus of this work will be whether the O(5) quantum numbers are preserved. In the following a brief introduction to the groups essential for this thesis is discussed.

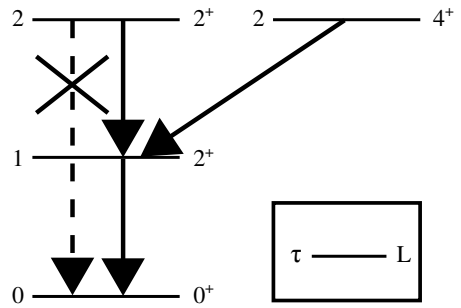

Figure 1.3: A schematic figure showing a level scheme using the dynamical O(6) limit and the corresponding reduction rules (see text). All states share the same $\sigma = 2$ quantum number. Labeling is given in the box. All the shown arrows are $E2$ transition.

1.2 O(5) group

The O(5) group is part of the algebraic chain of the U(5) limit and the O(6) limit. In the two limits, they are denoted with different quantum numbers, however in a purely bosonic system the simple relation is $\tau = \nu$. The eigenfunction of the second order Casimir operator $\hat{C}_2$[O(5)] is defined as [9]

$$E(\mathrm{O}(5)) = \tau(\tau + 3). \tag{1.4}$$

The τ quantum number induced by the O(5) group is also called seniority. The seniority can be understood when applying the Casimir operator $\hat{C}_2$[O(5)] on a given state with good O(5) quantum number, which is directly related to the number of d bosons which do not belong to pairs coupled to zero. In Fig. 1.3 an exemplary level scheme is given specifically for the O(6) limit. For clarity, only a system with two nucleon bosons $N = 2$ is considered. In that figure all states belong to the highest $\sigma = 2$ multiplet.

The reduction rule for O(6) $\supset$ O(5) is $\tau = 0, 1, ..., N = \sigma$, where N is the number of valence bosons. The angular momentum L is obtained for O(5) $\supset$ O(3) with the reduction rule $\tau = 3n_\Delta + \mu$ and $L = \mu, \mu + 1, ..., 2\mu - 2, 2\mu$. Using the reduction rules for the algebraic chain, all possible sets of quantum numbers are derived. For the ground state all d bosons are coupled to zero, thus seniority $\tau = 0$. To construct a $L = 2^+$ state, one d boson pair must be coupled to 2. In this way a level scheme can be constructed. An important experimental observable in order to verify τ quantum numbers are to observe $E2$ transitions. In the IBM-1, $E2$ transition operator is defined as

$$\hat{T}^{E2}_\mu = \epsilon_b[s^\dagger \times \widetilde{d} + d^\dagger \times \widetilde{s}]^{(2)}_\mu + \chi\, \epsilon_b[d^\dagger \times \widetilde{d}]^{(2)}_\mu, \tag{1.5}$$

where ϵ_b is the effectiv boson charge and χ some deformation parameter. In the O(6) limit the second term in Eq. (4.3) does not contribute to the transition strength due to symmetry considerations. Furthermore, the tensor properties of $d^\dagger_m$,$\tilde{d}_m$ operator applied on the states in the O(6) limit the selection rule for $E2$ transitions $\Delta\tau = \pm 1$ is obtained [9]. The arrows in Fig. 1.3 correspond to transition fulfilling (solid arrow) or breaking (dashed arrow) the selection rule. Consequently, beside exact B($E2$) values a simple way to test the goodness of the τ quantum number is to observe whether forbidden transitions occur.

1.3 Spin(5) group

The IBM-1 can be extended to the so-called Interacting Boson-Fermion Model (IBFM). Hereby, a fermion is coupled to a bosonic system. Specifically, in this thesis the focus is on a fermion in a $2d_{3/2}$ proton orbital coupled to a IBM-1 Hamiltonian in the O(6) limit. The corresponding group chain is [26]

$$\begin{array}{ccccccccc} \mathrm{U}^B(6) \otimes \mathrm{U}^F(4) & \supset & \mathrm{SO}^B(6) \otimes \mathrm{SU}^F(4) & \supset & \mathrm{Spin}^{BF}(6) & \supset & \mathrm{Spin}^{BF}(5) & \supset & \mathrm{Spin}^{BF}(3). \\ [N_B] \quad [1^{N_F}] & & \langle\sigma\rangle \quad \langle\alpha_1,\alpha_2,\alpha_3\rangle & & \langle\sigma_1,\sigma_2,\sigma_3\rangle & & (\tau_1,\tau_2) & & J \end{array} \tag{1.6}$$

The crucial part of the algebraic chain is that the fermionic group and the bosonic group can be combined to one group, the $\mathrm{Spin}^{BF}(6)$, thus inducing the so-called Bose-Fermi symmetry. This can be done as the SO^B and the $\mathrm{SU}^F(4)$ are isomorphic. This reduces significantly the number of parameters needed to construct a level scheme.
The $\mathrm{Spin}^{BF}(5)$ group is similar to the O(5) group, however it contains half-integer quantum numbers. As discussed above, again electromagnetic selection rules can be used to investigate the goodness of τ_1, τ_2 quantum numbers.

1.4 F-spin

Mixed-symmetry states [27] including the scissors mode [28], as well as other phenomenon such as giant dipole resonances [29] or pygmy resonances [30], involve the collective motion of neutrons against protons which essentially depend on the strength of the fundamental proton-neutron interaction. However, especially mixed-symmetry states are observed in the lower energy region at energies usually similar to or lower than needed to separate a proton or neutron pair. It turns out that the Interacting Boson Model 2 (IBM-2) [15] can describe the out-of-phase vibrations of valence neutrons and protons well.

In framework of IBM-2 one can introduce the so-called F-spin in analogue to the isospin, which is applied for proton and neutron bosons instead of particles. Hereby, the fully symmetric states are states with $F = F_{max} = 1/2(N_\pi + N_\nu) = F_{max}$, where N_π, N_ν is the number of proton, neutron bosons, respectively. The mixed symmetry states are associated with F quantum number $\neq F_{max}$. A detailed discussion about the F-spin is found Ref. [27].
The F-spin symmetric algebraic chain of the IBM-2 can be written as

$$\begin{array}{c} \mathrm{U(12)} \\ [N] \end{array} \begin{cases} \supset \mathrm{U(6)} \otimes \mathrm{U(2)} & \supset & \mathrm{U(6)} & \otimes & \mathrm{SU(2)}, \\ [N_1, N_2] \;\; [N_1, N_2] & & [N/2+F, N/2-F] & & [F] \\ \supset \mathrm{U}^\pi(6) \otimes \mathrm{U}^\nu(6) \supset \mathrm{U}^{\pi\nu}(6), & & & & \\ [N_\pi] \qquad [N_\nu] \quad [N/2+F, N/2-F] & & & & \end{cases} \tag{1.7}$$

where N, N_π and N_ν corresponds to the number of nucleon, proton and neutron bosons, respectively. In the first chain of Eq. (1.7) the quantum number associated with SU(2) is called the F-spin quantum number, which explains the analogue between F-spin and isospin. The two algebraic chains lead to the same irreducible representations (irreps), thus the F labeling can be transferred between the nested algebras and the F-spin quantum number obeys the reduction rule $1/2|N_\pi - N_\nu| \leq F \leq 1/2(N_\pi + N_\nu) = F_{max}$. States with maximum F-spin F_{max} are known as the fully symmetric states while states with $F \neq F_{max}$ are denoted as mixed symmetry states.

1.5 shape coexistence

The Interaction Boson Model and its extensions can also be used to describe a phenomenon known as shape coexistence [31, 32]. Shape coexistence is associated with two or more configurations exhibiting distinguishable nuclear shapes and are often understood in terms of (sub-)shell closures and cross-(sub-)shell excitations of protons and/or neutrons. In the A=100 mass region, several nuclei are known which have been discussed in the framework of shape coexistence [33–36]. It turns out, that this concept is needed in order to describe the molybdenum isotopes.
Here we employ the method of Ref. [37], the basic idea of which is that the parameters of the IBM-2 Hamiltonian are obtained by the mapping from the microscopic potential energy surface onto the expectation value of the equivalent boson Hamiltonian in the boson condensate state [38] (For details, see Refs. [37, 39]). Recently, the method of [37] has been extended to include the

mixing of the different configurations associated to the different shape intrinsic shapes. Hereby, we first perform a set of constrained Hartree-Fock-BCS calculations using the Skyrme functional SLy6 [40] using the code ev8 [41] to obtain the potential energy surface for a given nucleus. The constraint imposed here is for mass quadrupole moments, associated to the deformation parameters β and γ of the geometrical model [42]. The density-dependent pairing interaction is used for the pairing correlation in the BCS approximation, with its strength being the fixed value of V_0=1000 MeV, and Lipkin-Nogami prescription is taken for the treatment of the particle number. For the review on the self-consistent mean-field approach, the reader is referred to [43].

For the boson part, the following Hamiltonian is used for each configuration:

$$\hat{H} = \epsilon_\nu \hat{n}_{d\nu} + \epsilon_\pi \hat{n}_{d\pi} + \kappa \hat{Q}_\nu \cdot \hat{Q}_\pi + \hat{M}_{\pi\nu}, \tag{1.8}$$

where the first term

$$\hat{n}_{d\rho} = \sum\nolimits_{\rho,m} d^\dagger_{\rho,m} d_{\rho,m}, \quad \rho = \pi,\, \nu \tag{1.9}$$

stand for the d boson number operator. ϵ_ρ is the single proton or neutron boson energy, and is assumed to be the same between protons and neutrons, $\epsilon_\nu = \epsilon_\pi \equiv \epsilon$. The second term in (1.8) is the quadrupole-quadrupole interaction between the proton and the neutron bosons, with the quadrupole operator $\hat{Q}_\rho$ being

$$\hat{Q}_\rho = d^\dagger_\rho s_\rho + s^\dagger_\rho \tilde{d}_\rho + \chi_\rho [d^\dagger_\rho \times \tilde{d}_\rho]^{(2)}. \tag{1.10}$$

In the above equation, κ and χ_ρ stand for the strength parameter and the parameter which determines whether the nucleus is prolate or oblate.

The fourth term in Eq. (1.8) represents the so-called Majorana term which renders the symmetric states energetically favored:

$$\hat{M}_{\pi\nu} = \tfrac{1}{2}\xi_2 (d^\dagger_\pi s^\dagger_\nu - s^\dagger_\pi d^\dagger_\nu) \cdot (\tilde{d}_\pi s_\nu - s_\pi \tilde{d}_\nu) + \textstyle\sum_{\lambda=1,3} \xi_\lambda (d^\dagger_\pi d^\dagger_\nu)^{(\lambda)} \cdot (d^\dagger_\pi d^\dagger_\nu)^{(\lambda)}. \tag{1.11}$$

$\xi_{1,2,3}$ are the strength parameters, which are normally determined so that the mixed symmetry states are higher enough in energy.

Since the Majorana terms do not influence the boson energy surface, provided that the equal deformations between proton and neutron are assumed, the only parameters which are to be extracted by mapping from the microscopic potential energy surface are ϵ, κ, χ_π, and χ_ν.

The full Hamiltonian is given as

$$\hat{H} = \hat{P}_{nor} \hat{H}_{nor} \hat{P}_{nor} + \hat{P}_{intr} (\hat{H}_{intr} + \Delta) \hat{P}_{intr} + \hat{H}_{mix}, \tag{1.12}$$

where $\hat{H}_{nor}$ ($\hat{H}_{intr}$) and $\hat{P}_{nor}$ ($\hat{P}_{intr}$) represent the Hamiltonian of and the projection operator onto the normal (intruder) configuration space, respectively, and Δ specifies the energy shift between the configurations. The mixing of configurations is defined as

$$\hat{H}_{mix} = \omega_1(s_\pi^\dagger \cdot s_\pi^\dagger + d_\pi^\dagger \cdot d_\pi^\dagger) + \omega_2(s_\pi \cdot s_\pi + \tilde{d}_\pi \cdot \tilde{d}_\pi). \tag{1.13}$$

For simplicity, the mixing strength is set to $\omega_1 = \omega_2 \equiv \omega$.

1.6 Structure of this thesis

The primary aim of this work is to test how robust the O(5)/Spin(5) quantum number are within the evolution of nuclear shapes and with increasing number of neutrons. The odd-even gold isotopes in the A=200 were selected to investigate the Spin(5) symmetry. This is motivated by the occurrence of the well known supermultiplets around ^{194}Pt and ^{196}Pt, in which the Bose-fermi symmetry is embedded for the odd-A nuclei. The very gradual change apparent for the odd-even gold isotopes allows to test the preservation of the Spin(5) quantum number for a long chain of gold isotopes. Furthermore, the challenge is to test whether the switch of the ground state from spin $1/2$ to $3/2$ is reproducible for the Interacting Boson Fermion Model.
The molybdenum isotopes in the A=100 mass region provides a even greater challenge, since the nuclear shape in that mass region tends to change rather abruptly. Based on the concept of shape coexistence, the even-even molybdenum isotopes can be used to test the goodness seniority in the harsh condition of configuration mixing. Especially the mixed symmetry states provide a stringent test whether the selections rules can be still applied for shape coexistence in these nuclei.
First, some advances in the evaluation technique are presented, followed by papers dealing with the Bose-Fermi symmetry in the odd-even gold nuclei. Then the results of experiments in the even-even molybdenum isotopes condensed in two more publications are presented. Finally, the results are summarized and an outlook for further research is given.

Chapter 2

Method

In this thesis only data obtained from in-beam experiments were evaluated. The data of ^{96}Mo, ^{193}Au, and ^{195}Au originate from in-beam experiments performed at the Cologne FN-Tandem accelerator by using the Osiris spectrometer for ^{96}Mo and the Horus spectrometer for ^{193,195}Au. ^{98}Mo was measured in the last experimental campaign at the ESTU-Tandem accelerator at the Wright Nuclear Structure Lab (WNSL) at Yale University before the permanent shutdown of the accelerator in June, 2011.
In general, the advantage of in-beam experiments is that $\gamma\gamma$ coincidences in relation to the angle of the detectors provide angular correlations to test spin hypotheses and multipole mixing ratios. The angular correlation analysis together with the coincidence technique is extensively covered in the literature [44–46] and will not be discussed any further in this thesis. The angular correlation analysis was performed with the computer code CORLEONE [47, 48].
However, for the calculation of branching ratios the previous technique is improved to include the angular correlation analysis and is discussed in the following section.

2.1 Case study 1

In Fig. 2.1 the exemplary decays A, B, C are shown. Transition A with the γ energy $E_{\gamma,A}$ feeds a state, which is depopulated by the transition B and C. In this section the calculation of the relative γ intensity $I(B, C)$ (or branching ratio) between the transitions B and C is explained by using a gate set on the energy of transition A:

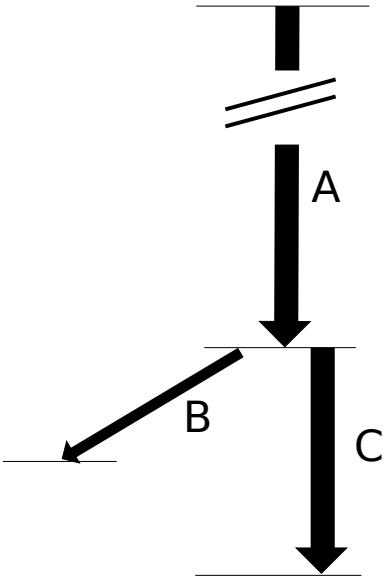

Figure 2.1: Two exemplary ($\gamma\gamma$) cascades (A,B) and (A,C) are show. The width of arrows correspond to the relative γ intensity between transition B and C. The two parallel lines symbolize the gate set at the energy of transition A.

$$[h] \quad \begin{aligned} b_1 &= b \cdot \omega_1 \cdot \epsilon_1 \\ b_i &= b \cdot \omega_i \cdot \epsilon_i \\ &\vdots \\ b_k &= b \cdot \omega_k \cdot \epsilon_k \end{aligned} \tag{2.1}$$

with

k=number of correlation groups
i=denominates the correlation group (from 1,..k)
b_i=volume of transition B in coincidence with transition A in correlation group i
$\omega(\sigma, \delta, J)$=angular correlation in correlation group i
ϵ_i=efficiency of correlation group i

The volume b of transition B denotes the volume after the correction due to angular correlations and efficiency. Thus, the total volume b_{tot} (the sum of all $\gamma\gamma$ coincidences) of transition B in coincidence with transition A is:

$$b_{tot} = \sum_{i=1}^{k} b_i = \sum_{i=1}^{k} b \cdot \omega_i \cdot \epsilon_i = b \underbrace{\sum_{i=1}^{k} \cdot \omega_i \cdot \epsilon_i}_{V(\omega,\epsilon)_b} \tag{2.2}$$

$$\Rightarrow b = \frac{b_{tot}}{V(\omega,\epsilon)_b} \tag{2.3}$$

analogue for the $\gamma\gamma$ cascade (A,C):

$$c = \frac{c_{tot}}{V(\omega,\epsilon)_c} \tag{2.4}$$

$$I(B,C) = \frac{b}{c} = \frac{b_{tot}}{c_{tot}} \cdot \frac{V(\omega,\epsilon)_c}{V(\omega,\epsilon)_b} \tag{2.5}$$

The corresponding error Δb (Δc) is derived from error propagation:

$$\Delta b = b_{tot} \cdot \sqrt{\left(\frac{\Delta b_{tot}}{b_{tot} \cdot V(\omega,\epsilon)_b}\right)^2 + \sum\nolimits_i \left(\frac{\omega_i \cdot \Delta\epsilon_i}{V(\omega,\epsilon)_b^2}\right)^2 + \sum\nolimits_i \left(\frac{\epsilon_i \cdot \Delta\omega_i}{V(\omega,\epsilon)_b^2}\right)^2} \tag{2.6}$$

The errors in the correlation groups depends on the deviation from one spin hypothesis to another in the corresponding correlation group. However, in case of a 4π detector array the sum over the different angular correlations is the same. Since not all angles are covered by detectors, the sum over different spin hypothesis differ, which is denoted as $\Delta\omega$. This leads to the following simplification:

$$\sum\nolimits_i \left(\frac{\epsilon_i \cdot \Delta\omega_i}{V(\omega,\epsilon)_b^2}\right)^2 = \left(\frac{\epsilon_{tot} \cdot \Delta\omega}{V(\omega,\epsilon)_b^2}\right)^2 \tag{2.7}$$

The error propagation of Eq. (2.5) and formula (2.6) leads to

$$\Delta I(B,C) = I(B,C) \cdot \sqrt{\left(\frac{\Delta b}{b}\right)^2 + \left(\frac{\Delta c}{c}\right)^2} \tag{2.8}$$

2.2 Case study 2

In the prior section the coincidences of one feeding transition A were used to investigate the relative γ intensity of the depopulating transitions B and C. Alternatively, instead of using a feeding transition one can use coincident depopulating transitions to calculate the relative γ intensity $I(B,C)$. In Fig. 2.2 a schematic level scheme is shown. The total volume b_{tot} (the sum of all $\gamma\gamma$ coincidences) of transition B is obtained by using coincidences with transition D (gate on the energy of transition D). However, b_{tot} has to be corrected for the

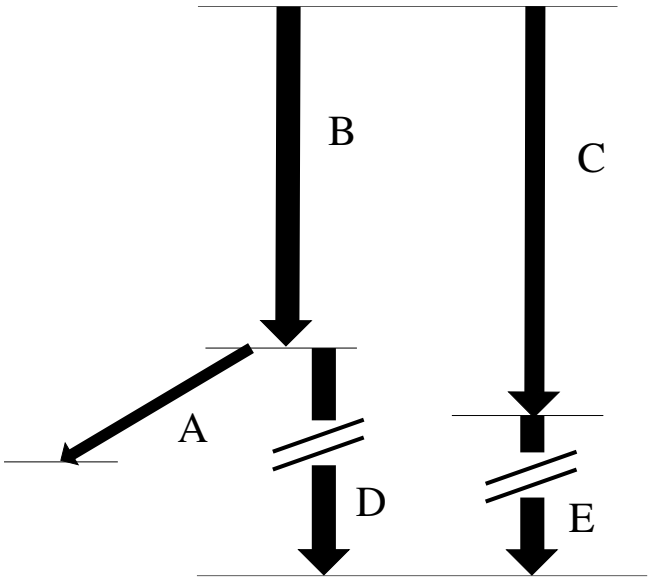

Figure 2.2: Exemplary $\gamma\gamma$ cascades (B,A), (B,D) and (C,E) are show. The two parallel lines symbolize the consecutive gates set at the energy of transition D and E, respectively. See text for detail.

alternative (B,A) $\gamma\gamma$ cascade. Thus, b is defined as:

$$b = \frac{b_{tot} \cdot \left(\frac{d}{d} + \frac{a \cdot (1+\alpha_A)}{d}\right)}{V(\omega,\epsilon)_b}, \tag{2.9}$$

with $a = \frac{a_{tot}}{V(\omega,\epsilon)_a}$, $d = \frac{d_{tot}}{V(\omega,\epsilon)_d}$ and α_A being the conversion coefficient of transition A. For the total volume c_{tot}, coincidences with transition E are used. Thus, for the calculation of errors additional terms with errors of the relative intensity for other depopulating transitions have to be included. The computer code MAMMEL [49] employs Eqs. (2.5-2.9) and was used to calculate the relative γ intensities.

Chapter 3

The gold isotopes

Available online at www.sciencedirect.com

ScienceDirect

Nuclear Physics A 922 (2014) 200–224

NUCLEAR PHYSICS A

www.elsevier.com/locate/nuclphysa

The structure of ^{193}Au within the Interacting Boson Fermion Model

T. Thomas [a,b,*], C. Bernards [a,b], J.-M. Régis [a], M. Albers [a], C. Fransen [a], J. Jolie [a], S. Heinze [a], D. Radeck [a], N. Warr [a], K.-O. Zell [a]

[a] *Institute for Nuclear Physics, University of Cologne, Zülpicher Straße 77, D-50937 Köln, Germany*
[b] *WNSL, Yale University, P.O. Box 208120, New Haven, CT 06520-8120, USA*

Received 7 November 2013; received in revised form 5 December 2013; accepted 7 December 2013

Available online 13 December 2013

Abstract

A $\gamma\gamma$ angular correlation experiment investigating the nucleus ^{193}Au is presented. In this work the level scheme of ^{193}Au is extended by new level information on spins, multipolarities and newly observed states. The new results are compared with theoretical predictions from a general Interacting Boson Fermion Model (IBFM) calculation for the positive-parity states. The experimental data is in good agreement with an IBFM calculation using all proton orbitals between the shell closures at $Z = 50$ and $Z = 126$. As a dominant contribution of the $d_{3/2}$ orbital to the wave function of the lowest excited states is observed, a truncated model of the IBFM using a Bose–Fermi symmetry is applied to the describe ^{193}Au. Using the parameters of a fit performed for ^{193}Au, the level scheme of ^{192}Pt, the supersymmetric partner of ^{193}Au, is predicted but shows a too small boson seniority splitting. We obtained a common fit by including states observed in ^{192}Pt. With the new parameters a supersymmetric description of both nuclei is established.

Keywords: NUCLEAR REACTIONS ^{194}Pt(p, 2n), $E = 14$ MeV; Measured E_γ, I_γ, $\gamma\gamma$-coin, $\gamma(\theta)$, using HORUS spectrometer. ^{193}Au; Deduced levels, J, π, branching and mixing ratios, B(M1), B(E2); Comparison with IBFM calculations

1. Introduction

The low-lying levels of the odd–even Au isotopes were studied, in the early 1970s, to address the question, whether theories coupling phonons to a proton are able to describe these

* Corresponding author.
E-mail address: tim.thomas@ikp.uni-koeln.de (T. Thomas).

0375-9474/$ – see front matter
http://dx.doi.org/10.1016/j.nuclphysa.2013.12.004

nuclei [1–3]. The measurement of conversion electrons and γ rays following the β decay from ^{193}Hg enabled Fogelberg et al. [1] to obtain the M1 and E2 transition strengths of several γ transitions in ^{193}Au. Half-life measurements were done via electron–electron coincidences. The aim was to describe the nucleus either in terms of a pairing-plus-quadrupole force model or in terms of a core-excitation model. Although both models described the energies of the low-lying states, the known transition strengths of the three lowest levels were not reproduced satisfactorily.

In 1980, Iachello introduced dynamical supersymmetries to describe bosonic and fermionic systems [4]. In the following year, the Interacting Boson Fermion Model (IBFM), an extension of the Interacting Boson Model (IBM), was applied to the positive-parity states of the nucleus ^{193}Au by Wood [5]. Theoretical transition strengths were calculated and compared them to experimental values, showing for the first time that the IBFM was able to describe this Au isotope.

In 1984, Van Isacker et al. [6] introduced the so-called extended supersymmetry by including the proton-neutron degree of freedom and, thus, were able to describe sets of four neighboring nuclei: even–even ^{196}Pt, odd-neutron ^{197}Pt, odd-proton ^{197}Au, and odd–odd ^{198}Au. Such a supermultiplet is also called *magical quartet* or *magical square*. Members of a supermultiplet are all described by the same algebraic Hamiltonian and by the same total number $\mathcal{N}_\rho = N_\rho + M_\rho$ of particles with N_ρ the number of bosons (or boson holes) and M_ρ the number of fermions (or fermion holes) with $\rho = \nu, \pi$ ($\nu =$ neutrons, $\pi =$ protons). The total number of particles, used for the description of the supermultiplet including ^{196,197}Pt and ^{197,198}Au, is $\mathcal{N}_\nu + \mathcal{N}_\pi = 6$. About 15 years later, experimental evidence was found for a new neighboring magical quartet consisting of ^{194,195}Pt and ^{195,196}Au [7–9]. Recently, the supersymmetric description was used to extend the magical quartets to quintets by including the nuclei ^{196}Hg and ^{198}Hg [10,11].

As these magical quartets consist of nuclei in the gold–platinum mass region, it is of interest whether ^{193}Au can be described by the Interacting Boson Fermion Model, and if a common description of the isotones ^{193}Au and ^{192}Pt in the supersymmetric O(6) limit is feasible.

In the following section, the Interacting Boson Fermion Model is introduced. A truncation of this model using only the $d_{\pi,3/2}$ orbital and in the O(6)-limit, the Bose–Fermi symmetry, is described in Section 3. Section 4 describes the experiment, and the results are presented. In Section 5, we discuss the implications of the new data to our understanding of the nucleus, as well as compare the data to theoretical predictions of the IBFM. Finally, the parameters of the fit are used to predict states in the neighboring ^{192}Pt nucleus.

2. Interacting Boson Fermion Model

The IBM was introduced, in order to describe collective behavior of even–even nuclei within an algebraic framework. This model was extended to the Interacting Boson Fermion Model 1 [12,13] (IBFM-1) by coupling one fermion to a bosonic system.

$$H = H_{\mathrm{sd}} + H_{\mathrm{F}} + V_{\mathrm{BF}}, \tag{1}$$

where H_{sd} represents the pure bosonic part of the Hamiltonian, while

$$H_{\mathrm{F}} = \sum_{k=1}^{5} \mathrm{PEN}(k)\hat{n}_k \tag{2}$$

is the Hamiltonian for the single nucleon degrees of freedom. The parameters PEN(k) denote the quasi-particle energies and $\hat{n}_k = -\sqrt{2j_k+1}[a_k^\dagger \times \tilde{a}_k]_0^{(0)}$ with j_k being the spin of the orbital k. The boson-fermion Interaction strength V_{BF} in its general [14] form can be reduced on basis of microscopic arguments [15] to

$$V_{\mathrm{BF}} = \sum_{\substack{k,k'=1,\\ k\leqslant k'}}^{5} \mathrm{BFQJ}(N_{kk'})\left\{\left(Q^{(2)}\cdot\left(a_k^{\dagger}\times\tilde{a}_{k'}\right)^{(2)}\right)+\mathrm{h.c.}\right\}$$
$$+\sum_{k,k'=1}^{5}\sum_{k''}\Lambda_{kk'}^{k''}\frac{1}{\hat{j}_k''}:\left[\left[d^{\dagger}\times\tilde{a}_k\right]^{(j_{k''})}\times\left[\tilde{d}\times a_{k'}^{\dagger}\right]^{(j_{k''})}\right]_0^{(0)}:$$
$$+\sum_{k=1}^{5}\mathrm{BFMJ}(k)\hat{n}_d\hat{n}_k, \tag{3}$$

where : : represents the normal ordering, $\hat{n}_d=\sqrt{5}[d^{\dagger}\times\tilde{d}]_0^{(0)}$, the fermion annihilation operator defined as $\tilde{a}_{km}=(-1)^{j_k-m}a_{k-m}$, and

$$Q^{(2)}=\left(s^{\dagger}\times\tilde{d}+d^{\dagger}\times\tilde{s}\right)^{(2)}+\chi\left(d^{\dagger}\times\tilde{d}\right)^{(2)}, \tag{4}$$

$$\Lambda_{kk'}^{k''}=-\sqrt{5}\,\mathrm{BFE}\left\{(u_{k'}v_{k''}+v_{k'}u_{k''})Q_{k'k''}\beta_{kk''}+(u_kv_{k''}+v_ku_{k''})Q_{kk''}\beta_{k'k''}\right\}, \tag{5}$$

$$\beta_{kk'}=\begin{cases}\beta'_{kk'}, & k\leqslant k',\\ (-1)^{j_k-j_{k'}}\beta'_{kk'}, & k'\leqslant k,\end{cases} \tag{6}$$

with $v_k=\sqrt{\mathrm{VSQ}(k)}$, $u_k=\sqrt{1-\mathrm{VSQ}(k)}$, and $\mathrm{VSQ}(k)$ being the occupation probability of the orbital k. The coefficients $\beta_{kk'}$ can be related to the microscopic structure of the d-boson. Under the assumption that the $|D\rangle$-state absorbs the full E2-strength, it can be shown that:

$$\beta'_{kk'}=\frac{1}{\mathrm{PEN}(k)+\mathrm{PEN}(k')-\Omega}(u_kv_{k'}+u_{k'}v_k)Q_{kk'}, \tag{7}$$

where Ω denotes the energy of the $|D\rangle$-state relative to the $|S\rangle$-state. Ω can be obtained from the excitation energy of the 2_1^+ state in a semimagic nucleus.

The monopole and quadrupole force can be simplified assuming independence of the orbit

$$\mathrm{BFQJ}(N_{kk'})=\mathrm{BFQ}(u_ku_{k'}-v_kv_{k'})Q_{kk'},\quad k\leqslant k', \tag{8}$$

$$\mathrm{BFMQJ}(k)=\mathrm{BFM}. \tag{9}$$

Summarizing, the boson-fermion interaction given by Eqs. (3)–(9) is fully specified by the three interaction strengths BFQ, BFE, BFM, the parameter in the quadrupole operator, χ, the occupation probabilities $\mathrm{VSQ}(k)$ of the different orbitals, and the quasi-particle energies $\mathrm{PEN}(k)$.

3. Bose–Fermi symmetry and supersymmetry

Since ^{193}Au is located in the proximity of the supermultiplets, the Interacting Boson Fermion Model 1 (IBFM), in the O(6) limit [16], seems to be an appropriate choice for the description of this nucleus. Hereby, a fermion in the $J^{\pi}=3/2^+$ orbital is coupled to a system of seven bosons using the $\mathrm{U^B}(6)\otimes\mathrm{U^F}(4)$ algebra. Isomorphisms in the sub-algebra structure of $\mathrm{U^B}(6)\otimes\mathrm{U^F}(4)$ can be found between the boson and fermion algebras. Such an isomorphism exists between $\mathrm{U^B}(6)\supset\mathrm{SO^B}(6)$ and $\mathrm{U^F}(4)\supset\mathrm{SU^F}(4)\simeq\mathrm{Spin^F}(6)$ groups. The generators, g_k, of these subgroups, $\mathrm{SO^B}(6)$ and $\mathrm{SO^F}(6)$ commute and a linear combination of these generators closes under commutation, and thus, form a boson-fermion algebra $\mathrm{Spin^{BF}}(6)$. This is the so-called Bose–Fermi symmetry and is discussed in more detail in Refs. [17,18], while only equations essential for this work are given here.

The group chain of the Hamiltonian in the O(6) limit is:

$$\begin{array}{ccccccccccc} \mathrm{U^B}(6) & \otimes & \mathrm{U^F}(4) & \supset & \mathrm{SO^B}(6) & \otimes & \mathrm{SU^F}(4) & \supset & \mathrm{Spin^{BF}}(6) & \supset & \mathrm{Spin^{BF}}(5) \supset \mathrm{Spin^{BF}}(3), \\ [N_\mathrm{B}] & & \left[1^{N_\mathrm{F}}\right] & & \langle\sigma\rangle & & \langle\alpha_1,\alpha_2,\alpha_3\rangle & & \langle\sigma_1,\sigma_2,\sigma_3\rangle & & (\tau_1,\tau_2) \qquad J \end{array} \tag{10}$$

where we have indicated under each group the quantum number classifying the irreducible representation. The number of fermions is $N_\mathrm{F} = 1$ in the case of the odd A nucleus and N_B denotes the number of bosons. Other quantum numbers of the nested algebras are determined by reduction rules (see Ref. [16]). The Hamiltonian written in the form of a linear combination of Casimir operators corresponding to the group chain, neglecting constant terms that only contribute to the binding energy, is:

$$\begin{aligned} H = {} & D \cdot C_2\big[\mathrm{SO^B}(6)\big] + A \cdot C_2\big[\mathrm{Spin^{BF}}(6)\big] \\ & + B \cdot C_2\big[\mathrm{Spin^{BF}}\ (5)\big] + C \cdot C_2\big[\mathrm{Spin^{BF}}(3)\big]. \end{aligned} \tag{11}$$

Where $C_2[X]$ is the second order Casimir operator of the given algebra. The corresponding energy eigenfunction of the Hamiltonian can be derived from the eigenfunction of the Casimir operators of the subgroups:

$$\begin{aligned} E = {} & D\sigma(\sigma+4) + A\big(\sigma_1(\sigma_1+4) + \sigma_2(\sigma_2+2) + \sigma_3^2\big) \\ & + B\big(\tau_1(\tau_1+3) + \tau_2(\tau_2+1)\big) + C\big(J(J+1)\big). \end{aligned} \tag{12}$$

For this Hamiltonian, it is possible to find an embedding superalgebra to the Bose–Fermi symmetry [18]. The generators of this supersymmetry consist of mixed boson-fermion creation and annihilation operators, and therefore, do not form a Lie algebra, but a superalgebra. While the Bose–Fermi symmetry preserves the boson and fermion numbers separately, the supersymmetry only preserves the total number of particles $\mathcal{N} = N_\mathrm{B} + N_\mathrm{F}$. The embedding algebra of $\mathrm{U^B}(6) \otimes U^\mathrm{F}(4)$ is:

$$\begin{array}{ccc} \mathrm{U}(6/4) & \supset & \mathrm{U^B}(6) \otimes \mathrm{U^F}(4). \\ \downarrow & & \downarrow \\ [\mathcal{N}] & & [N_\mathrm{B}, 1^{N_\mathrm{F}}] \end{array} \tag{13}$$

In the case that a fermion is annihilated and a boson created, the number of fermions is $N_\mathrm{F} = 0$ and the problem can be described within the Interacting Boson Model (IBM). The eigenvalues of the IBM-1 in the O(6) limit are [18]

$$E = \bar{A}\sigma(\sigma+4) + B\tau(\tau+3) + CJ(J+1), \tag{14}$$

with $\bar{A} = A + D$. Note, that in this work the IBFM with a $J = 3/2$ particle in the O(6) limit is referred to as the U(6/4) limit.

4. Experimental results

The experiment was performed at the Cologne tandem accelerator by impinging a 14 MeV proton beam onto a 1.3 mg/cm^2 ^{194}Pt target. In the primary reaction channel, ^{193}Au was produced via a ^{194}Pt(p, 2n) reaction. The expected cross section for this reaction is predicted around 700 mbarn, calculated with the computer code CASCADE [19]. The code also predicts a grazing angular momentum transfer of about $3.5\hbar$. We have used the HORUS spectrometer [20], an array equipped, during this experiment, with 12 high-purity germanium detectors on the edges and the

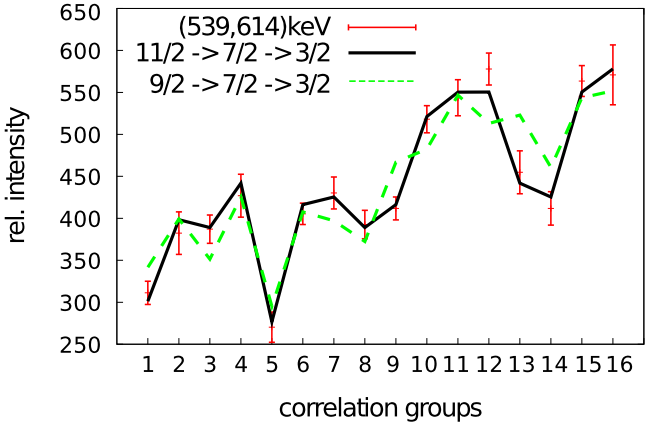

Fig. 1. (Color online.) Comparison of theoretical angular correlation with different spin hypotheses (black solid and green dashed line) with relative intensities obtained from 16 correlation groups for the 539–614 keV $\gamma\gamma$ coincidence.

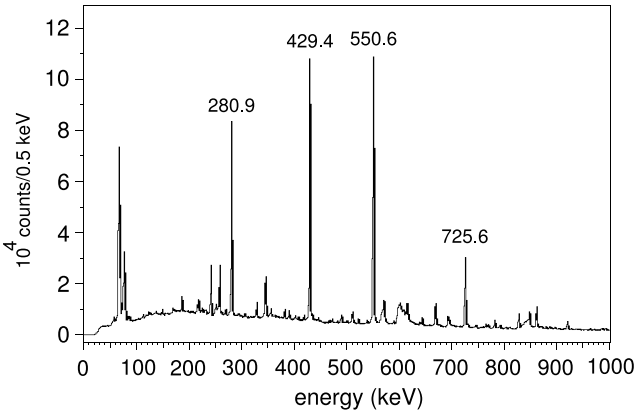

Fig. 2. $\gamma\gamma$ coincidence spectrum energy-gated on the 258.0 keV transition in ^{193}Au from $J^\pi = 5/2^+_1$ state to the ground state. The energies of the strongest transitions in coincidence with the 258.0 keV transition are given.

faces of a cube, to detect γ transitions of excited states in ^{193}Au. The setup of the spectrometer allows the analysis of $\gamma\gamma$ angular correlations. We sorted the data in so-called correlation group matrices, which consist of detector pairs defined by specific angles. This way the experimental angular correlation of two correlated γ transitions is determined. The method, using the HORUS spectrometer is described in more detail in the Refs. [10,20]. By fitting a spin hypothesis $J_1 \xrightarrow{E_A,\delta_A} J_2 \xrightarrow{E_B,\delta_B} J_3$, described in Refs. [21,22], to the data, spins of the initial E_{inital} and final state E_{final} and multipole mixing ratios, $\delta_{A,B}$, are obtained. The fit is performed with the computer code CORLEONE [23]. Fig. 1 shows an exemplary $\gamma\gamma$ angular correlation analysis for the spin hypotheses $11/2 \xrightarrow{614} 7/2 \xrightarrow{539} 3/2_{gs}$ (black solid line) and $9/2 \xrightarrow{614} 7/2 \xrightarrow{539} 3/2_{gs}$ (green dashed line). The spin hypothesis $11/2 \xrightarrow{614} 7/2 \xrightarrow{539} 3/2_{gs}$ fits the data best. Thus, the spin for the state at 1153 keV was determined to be 11/2. In Appendix A (see Figs. A.1–A.6), more angular correlation plots are shown.

Although ^{193}Au has been measured in in-beam experiments [2,24–26] previously, this is the first time that an experiment with small momentum transfer was chosen, in order to observe low-energy positive-parity states. An example of a γ-ray coincidence spectrum, with a gate on the 258.0 keV transition of the $J^\pi = 5/2^+_1$ state to the ground state, is shown in Fig. 2. By analyzing the $\gamma\gamma$ coincidence matrices, we identified numerous new transitions and states. The spins of all known low-lying positive-parity states were determined, except for a state at 38 keV.

Our results are listed in Table 1. Unless stated otherwise, corrections of the level energies or transition energies, given in Table 1, are due to the improved capability to detect γ rays. All those values differing from the results of this work, are based on the observations of Ref. [3]. Three Ge(Li) detectors were used to observe γ decays in Ref. [3], whereas in this work, an array of 12 high purity Ge detectors was applied, resulting in a superior absolute efficiency [20].

In the case that new states are observed with only one depopulating transition, coincidence spectra with a gate on the depopulating transition as well as a gate on a coincident transition is given (see Figs. A.7, A.8 in Appendix A). In Table A.1, additional coincident γ transitions are listed.

In the following section, some states in ^{193}Au are discussed in more detail, in order to clarify experimental observation, especially if the experimental results of this work are in conflict with literature:

38.2 keV, $(1/2)^+$. The transition to the ground state is not observed, due to the low energy of the γ ray. The experimental setup was optimized to detect γ energies between $E_\gamma =$ 180–1000 keV. The spin of this state was not determined in this experiment, but is adopted from Ref. [3].

290.2 keV, $11/2^-$. This level is known as an isomeric state with $\tau = 5.6(4)$ s [27]. No γ transitions are observed, since the 290.2 keV state decays dominantly via conversion electrons. The spin of this state was not determined in this experiment, but is adopted from Ref. [3].

381.6 keV, $5/2^+$. The $\gamma\gamma$ angular correlation analysis yields two possible multipole mixing ratios, $\delta = -2.93^{+45}_{-62}$ and $\delta = -0.07(5)$, for the 381.6 keV transition to the ground state. In Ref. [3], a multipole mixing ratio of $\delta = 1.2^{+5}_{-3}$ was determined by measuring conversion electrons, for the 381.6 keV transition, with a magnetic Siebahn–Svartholm $\pi\sqrt{2}$ spectrometer. Since a strong E2 characteristic seems to be more likely from the conversion electron measurement, the multipole mixing ratio closer to zero is ruled out, and $\delta = -2.93^{+45}_{-62}$ is given in Table 1 for this transition.

828.0 keV, $3/2^+$. Our data do not agree with the assignment of the transition at 289.0 keV, from [3], to this level. This supports the statement in the NDS [28], that the placement of this γ decay is not clear, suggesting it belongs to ^{193}Hg. Furthermore, the strongest transition at 789.21(20) keV in Ref. [3] turns out to be a doublet, and is corrected to 789.7(2) keV. The transition at 827.81(20) keV, in Ref. [3], is observed at 828.0(2) keV, as this γ line turned out to be a triplet. Distinguishing these multiplets is possible with the newly observed γ decays at 277.9, 488.9, 635.1 and 750.0 keV, feeding the state at 828.0 keV. Using these feeding transitions and the newly observed decay at 603.2 keV depopulating this state, new branching ratios are established. The spin of this state could be established, due to angular correlation of the (446, 381) keV cascade (see Fig. A.5).

1106.0 keV, $7/2^+$. The angular correlation analysis of transitions depopulating this newly observed state show, that either spin $J = 7/2$ or $9/2$ can be assigned to this state. However, we observe a 277.9 keV transition, populating the 828 keV state with spin $J = 3/2^+$, so the spin hypothesis $J = 9/2^+$ is discarded.

1119.0 keV, $3/2^+$. The angular correlation analysis of this state yields the spin $J = 3/2$ (cf. A.6) for this state, with two possible multipole mixing ratios $\delta_{861} = 0.35(8)$ and $\delta_{861} = 1.33(40)$. While the experimental $K/L_{1,2} = 6.1(13)$ ratio [3] is reproduced by the theoretical ratios $K/L_{861,\delta=0.35} = 6.2(3)$ and $K/L_{861,\delta=1.33} = 5.9(3)$ [47], the conversion coefficient for the larger multipole mixing ratio ($\alpha_{K,\delta=0.35} = 0.0161(6)$ and

Table 1
Results of this work compared to the literature values from Nuclear Data Sheets (NDS) [28]. States discussed in Section 4 are labeled with $^{\#}$. Newly observed states are labeled with * and newly observed transitions with †. Transitions given in NDS, but whose placement in the level scheme do not agree with data from this experiment, are discussed in Section 4 and the branching ratios are labeled with ♯. Furthermore, branching ratios of transitions, that are listed in NDS but not observed due to the sensitivity limit of the detector system or background, are labeled with −. States whose spin assignment was obtained from selection rules of γ transitions are labeled with ‖. If the spin of a state is adopted from NDS it is labeled with ** while spins taken from Ref. [26] are labeled with ††. If multiple spins can be assigned to a state due to angular correlation analysis, those spins are labeled with ‡‡. If an angular correlation analysis is not feasible but selection rules suggest the multipole characteristic of the γ transition, the multipolarity is given in parentheses. The multipole mixing ratio is given in parenthesis, when the angular correlation analysis does not yield a distinct δ value.

E_{level} [keV]	J^{π}_{initial}	E_{γ} [keV]	I_{γ}	$I_{\gamma,\text{NDS}}$	δ this work	δ [28]	E_{final} [keV]	J^{π}_{final}
0.0	$3/2^{+}$							
38.2(1)$^{\#}$	$(1/2)^{+**}$	38.2		100		0.42^{+5}_{-4}	0.0	$3/2^{+}$
224.8(1)	$3/2^{+}$	186.6(2)	100(10)	100(10)	+0.11(15)	0.26(5)	38.2(1)	$(1/2)^{+}$
		224.8(2)	5(1)	6.8(14)		(E2)	0.0	$3/2^{+}$
258.0(1)	$5/2^{+}$	219.8(2)	6(1)	5.7(3)	+0.02(59)	(E2)	38.2(1)	$(1/2)^{+}$
		258.0(1)	100(10)	100	−0.75(11)	0.62(4)	0.0	$3/2^{+}$
290.2(2)$^{\#}$	$11/2^{-**}$					(M4)		
381.6(1)$^{\#}$	$5/2^{+}$	156.8(2)†	1(1)				224.8(1)	$3/2^{+}$
		343.4(2)†	6(1)		(E2)		38.2(1)	$(1/2)^{+}$
		381.6(1)	100(10)	100	$-(2.93^{+45}_{-62})$	1.2^{+5}_{-3}	0.0	$3/2^{+}$
508.1(2)	$7/2^{-**}$	126.5	5(2)	7(2)	(E1)	E1	381.6(1)	$5/2^{+}$
		218.0(1)	100(10)	100	(E2)	E2	290.2(2)	$11/2^{-}$
538.9(1)	$7/2^{+}$	157.2(2)	2(1)	2.5(5)		(E2)	381.6(1)	$5/2^{+}$
		280.9(2)	26(4)	15(12)	−0.06(3)	(M1, E2)	258.0(1)	$5/2^{+}$
		314.0(2)†	2(1)				224.8(1)	$3/2^{+}$
		538.9(1)	100(10)	100	−0.03(13)	(E2)	0.0	$3/2^{+}$
687.5(1)	$7/2^{+}$	148.5(3)†	1(1)				538.9(1)	$7/2^{+}$
		305.9(2)†	9(1)		$+0.22^{+22}_{-19}$		381.6(1)	$5/2^{+}$
		429.4(1)	100(10)	100	-0.19^{+2}_{-3}		258.0(1)	$5/2^{+}$
		462.6(2)†	13(2)		+0.00(20)		224.8(1)	$3/2^{+}$
		687.5(2)†	27(1)		(E2)		0.0	$3/2^{+}$
697.8(2)	$15/2^{-\dagger\dagger}$	407.6(1)	100	100			290.2(2)	$11/2^{-}$
790.0(2)	$9/2^{-**}$	251.0(2)†	2(2)		(E1)		538.9(1)	$7/2^{+}$
		281.7(2)	20(1)	16.5(20)		0.69(12)	508.1(2)	$7/2^{-}$
		499.8(1)	100(10)	100(13)		1.0(3)	290.2(2)	$11/2^{-}$
808.6(1)	$9/2^{+}$	269.6(2)	3(1)		−0.13(5)		538.9(1)	$7/2^{+}$
		427.0(2)†	3(1)		(E2)		381.6(1)	$5/2^{+}$
		550.6(1)	100(10)		−0.03(2)	E2	258.0(1)	$5/2^{+}$
828.0(1)$^{\#}$	$3/2^{+**}$	289.0♯		25(12)			538.9(1)	$7/2^{+}$
		446.4(2)	52(9)	15(5)	−0.30(7)		381.6(1)	$5/2^{+}$
		603.2(3)†	100(10)		$(+0.50^{+36}_{-28})$		224.8(1)	$3/2^{+}$
		789.7(2)	54(4)	100		(M1)	38.2(1)	$(1/2)^{+}$
		828.0(2)	81(23)	88(15)	$+0.78^{+81}_{-45}$	(E2)	0.0	$3/2^{+}$
863.4(2)	$(13/2)^{-**}$	165.6(5)	>1	0.28 (7)			697.8(2)	$15/2^{-}$
		573.2(2)	100(10)	100		0.36(7)	290.2(2)	$11/2^{-}$
890.8 (1)	$9/2^{-**}$	382.5(2)	100(10)	100(21)		M1	508.1(2)	$7/2^{-}$
		600.6(1)	84(17)	100(11)		1.4^{+4}_{-3}	290.2(2)	$11/2^{-}$
929.1(1)	$9/2^{+}$	241.7(3)	39(10)		−0.12(5)		687.5(1)	$7/2^{+}$
		390.1(3)†	29(2)	40(9)	+0.03(8)	(M1)	538.9(1)	$7/2^{+}$

Table 1 (*continued*)

E_{level} [keV]	J^{π}_{initial}	E_{γ} [keV]	I_{γ}	$I_{\gamma,\text{NDS}}$	δ this work	δ [28]	E_{final} [keV]	J^{π}_{final}
		547.5(1)	100(10)	100(26)	−0.03(7)	(E2)	381.6(1)	$5/2^+$
		638.9(2)†	14(5)		(E1)		290.2(2)	$11/2^-$
983.6(2)*	$7/2^+$	155.6(4)†	2(1)				828.0(1)	$3/2^+$
		444.6(4)†	100(10)				538.9(1)	$7/2^+$
		725.6(2)†	100(10)		$+2.54^{+30}_{-25}$		258.0(1)	$5/2^+$
		758.8(2)†	56(4)		0.02(21)		224.8(1)	$3/2^+$
1085.3*(2)	$(7/2)^+$	295.4(3)†	100 (10)		(E1)		790.0(2)	$9/2^-$
		577.1(2)†	23(3)		(E1)		508.1(2)	$7/2^-$
		703.7(2)†	37(4)		$(+0.36^{+21}_{-19})$		381.6(1)	$5/2^+$
		827.5(3)†	40(5)		(+0.48(16))		258.0(1)	$5/2^+$
		860.5(3)†	63(8)		(E2)		224.8(1)	$3/2^+$
1089.6(3)		581.4(2)	100	100			508.1(2)	$7/2^-$
1106.0(2)*,#	$7/2^+$	277.9(2)†	20 (4)		(E2)		828.0(1)	$3/2^+$
		567.1(3)†	59(12)		$+0.32^{+22}_{-19}$		538.9(1)	$7/2^+$
		724.3(2)†	100(10)		+0.40(11)		381.6(1)	$5/2^+$
		847.8(3)†	35(7)		+0.28(5)		258.0(1)	$5/2^+$
1119.0(2)#	$3/2^+$	861.0(2)	100	100(17)	+1.33(40)	E2	258.0(1)	$5/2^+$
		1080.7	–	29(4)			38.2(1)	$(1/2)^+$
		1118.8	–	64(9)		(E2)	0.0	$3/2^+$
1131.8(3)	$7/2^-, 9/2^-, 11/2^{-**}$	341.8(3)	100	100		0.9(3)	790.0(2)	$9/2^-$
1153.5(3)	$11/2^+$	344.9(3)	63(13)	91(39)	−0.02(5)		808.6(1)	$9/2^+$
		614.7(3)	100(10)	100(16)	+0.03(9)	(E2)	538.9(1)	$7/2^+$
1194.3(3)	$(9/2^-, 11/2^-, 13/2^-)^{**}$	404.3(3)	100	100		(E2)	790.0(2)	$9/2^-$
1243.6(3)*	$(1/2 \text{ to } 9/2^+)^{\parallel}$	962(3)†	19(6)				381.6(1)	$5/2^+$
		1085.7(2)†	100(10)				258.0(1)	$5/2^+$
1284.8(3)	$9/2, 11/2^{-**}$	394.0(3)	100	100		0.59(23)	890.8(1)	$9/2^-$
		776.6(2)	35(7)	26(10)			508.1(2)	$7/2^-$
		994.9(2)	54(11)	61(7)			290.2(2)	$11/2^-$
1297.6(3)*	$(3/2 \text{ to } 11/2)^{\parallel}$	207.7(3)†	19(4)				1089.6(3)	
		789.1(2)†	100(10)				508.1(2)	$7/2^-$
1300.4(3)*	$(3/2 \text{ to } 11/2^+)^{\parallel}$	215.1(3)†	100(10)				1085.3(2)	$7/2^+$
		612.9(3)†	13(5)				687.5(1)	$7/2^+$
1330.9(2)*	$9/2^+$	347.3(3)†	100(10)		−0.20(13)		983.6(2)	$7/2^+$
		401.8(3)†	95(19)				929.1(1)	$9/2^+$
		522.3(3)†	53(11)				808.6(1)	$9/2^+$
		643.5(3)†	89(18)				687.5(1)	$7/2^+$
		949.3(3)†	28(6)				381.6(1)	$5/2^+$
1372.9(3)	$15/2, 17/2^-$	675.1(3)	100	100		1.5^{+11}_{-5}	697.8(2)	$15/2^-$
1379.9(2)#	$11/2^+$	516.7(3)¤		52(15)			863.4(2)	$(13/2)^-$
		571.3(2)†	100(10)		+0.05(7)		808.6(1)	$9/2^+$
		692.5(3)	98(20)	97(30)	−0.05(8)	(E2)	687.5(1)	$7/2^+$
		840.9(3)	77(15)	100(21)	(E2)		538.9(1)	$7/2^+$
1398.4(3)	$(13/2)^{-**}$	535.1(3)	100(10)	100(20)		1.4^{+12}_{-5}	863.4(2)	$(13/2)^-$
		608.70(10)	–	4.7(3)			790.0(2)	$9/2^-$
		700.8(3)	49(20)	15(3)		1.2^{+9}_{-5}	697.8(2)	$15/2^-$
1400.4(3)	$11/2^{-**}$	509.43(6)	–	37(18)			890.8(1)	$9/2^-$
		537.0(3)	100	100(13)		0.8^{+5}_{-4}	863.4(2)	$(13/2)^-$
		1109.80(17)	–	32(5)			290.2(2)	$11/2^-$

(*continued on next page*)

Table 1 (*continued*)

E_{level} [keV]	J^{π}_{initial}	E_{γ} [keV]	I_{γ}	$I_{\gamma,\text{NDS}}$	δ this work	δ [28]	E_{final} [keV]	J^{π}_{final}
1418.0(3)*	$(5/2, 7/2)^{+\parallel}$	434.4(3)†	58(12)				983.6(2)	$7/2^{+}$
		488.9(3)†	64(13)				929.1(1)	$9/2^{+}$
		590.0(3)†	67(17)				828.0(1)	$3/2^{+}$
		609.3(3)†	32(6)				808.6(1)	$9/2^{+}$
		879.1(3)†	100(10)				538.9(1)	$7/2^{+}$
1419.1(3)	$19/2^{-}$††	721.3(3)	100	100	+0.09 (12)	E2	697.8(2)	$(15/2)^{-}$
1463.1(4)*	$(1/2 \text{ to } 7/2^{+})^{\parallel}$	572.3(3)†	100(10)		(E1)		890.8(1)	$9/2^{-}$
		635.1(3)†	21(5)				828.0(1)	$3/2^{+}$
1477.0(3)#	$9/2^{+}, 11/2^{+}, 13/2^{+}$	668.4(2)	100				808.6(1)	$9/2^{+}$
1496.1(3)	$(9/2)^{-}$**	364.3(3)	100(10)	100(11)	-0.53^{+10}_{-11}	1.3^{+5}_{-4}	1131.8(3)	$11/2^{-}$
		706.2(3)	32(6)	39(18)		(E2)	790.0(2)	$9/2^{-}$
		957.42(25)	–	13(3)		(E1)	538.9(1)	$7/2^{+}$
		1205.3(6)	–	1.3(5)			290.2(2)	$11/2^{-}$
1526.7(4)*	$(9/2, 7/2^{+})^{\ddagger\ddagger}$	987.9(3)†	100				538.9(1)	$7/2^{+}$
1571.8(3)*		274.4(3)†	100(10)				1297.6(3)	$(3/2^{+} \text{ to } 11/2^{+})$
		482.1(3)†	17(3)				1089.6(3)	
1575.7(3)	$11/2^{-}, 13/2^{-}$**	290.8(3)†	30(6)	40(8)		M1	1284.8(3)	$9/2, 11/2^{-}$
		444.0(4)	–	3.5(10)			1131.8(3)	$7/2^{-}, 9/2^{-}, 11/2^{-}$
		684.77(12)	–	29(12)		(E2)	890.8(1)	$9/2^{-}$
		712.5(3)	10(3)	17(3)		(E2)	863.4(2)	$(13/2)^{-}$
		877.9(3)	100(10)	100(13)		E2	697.8(2)	$(15/2)^{-}$
		1285.20(20)	–	29(4)		(E2)	290.2(2)	$11/2^{-}$
1578.0(3)*	$(5/2, 7/2)^{+\ddagger\ddagger}$	472.1(2)†	100(10)				1106.0(2)*	$7/2^{+}$
		750.0(2)†	17(6)				828.0(1)	$3/2^{+}$
1598.7(4)*		404.3(3)†	100				1194.3(3)	$(9/2^{-}, 11/2^{-}, 13/2^{-})$
1630.4(4)	$11/2^{-}, 13/2^{-}$**	274.95(7)	–	0.56(14)		1.2^{+9}_{-4}	1355.31(8)	$(11/2 \text{ to } 15/2^{-})$
		345.46(4)	–	8.6(9)		0.37^{+13}_{-1}	1284.8(3)	$9/2, 11/2^{-}$
		739.47(17)	–	1.3(8)			890.8(1)	$9/2^{-}$
		766.97(20)	–	3.1(6)			863.4(2)	$(13/2)^{-}$
		932.6(3)	100	100(10)		(E2)	697.8(2)	$15/2^{-}$
1655.4(4)*	$(3/2 \text{ to } 11/2^{+})^{\parallel}$	726.3(3)†	100				929.1(1)	$9/2^{+}$
1658.5 (4)	$(1/2^{+} \text{ to } 9/2^{+})^{\parallel}$	1276.9(3)	100			(E2)	381.6(1)	$5/2^{+}$
1678.8(3*)	$(3/2^{+} \text{ to } 11/2^{+})^{\parallel}$	695.2(2)†	100(10)				983.6(2)	$7/2^{+}$
		870.2(3)	68(18)				687.5(1)	$7/2^{+}$
1733.3(3)	$(15/2)^{-}$**	360.5(4)	30 (8)	14 (4)		1.0^{+6}_{-4}	1372.9(3)	$(17/2)^{-}$
		869.9(3)	100(10)	100(14)		(E2)	863.4(2)	$(13/2)^{-}$
		1035.9(3)	60(12)	62(10)		(E2)	697.8(2)	$15/2^{-}$
1745.1(3)*		1236.8(3)†	100				508.1(2)	$7/2^{-}$

$\alpha_{K,\delta=1.33} = 0.0101(20)$) fits better the observed value, $\alpha_{K,\text{exp}} = 0.0061(16)$. Thus, in Table 1, only the larger multipole mixing ratio is given. Note, that the angular correlation analysis from this experiment does also support a spin hypothesis of $J = 7/2$ with $\delta_{861} = -2.28^{+49}_{-75}$, but this spin, together with the positive-parity, does not fit to the observed log(ft) value and thus is discarded.

1379.9 keV, $11/2^{+}$. Considering the branching ratios in [3], our data does not support the assignment of the transition with 516.7 keV to this level, as no transition with about 50% intensity with respect to the 840.9 keV transition is observed in the $\gamma\gamma$ coincidence

Table 2
The first two rows compare single-particle energy (SPE) in MeV, given in Ref. [30] for A = 207, with SPEs adjusted for ^{193}Au for a orbital k. The next rows show the parameters PEN in MeV and VSQ in percentage of the orbitals derived with the BCS formalism from the $\mathrm{SPEs}_{193\mathrm{Au}}$. Note that the PENs and VSQs are calculated for proton-holes.

	$g_{7/2}$	$d_{5/2}$	$h_{11/2}$	$d_{3/2}$	$s_{1/2}$
$\mathrm{SPE}_{[30]}$ (MeV)	0.0	0.80	2.10	2.60	2.95
$\mathrm{SPE}_{193\mathrm{Au}}$ (MeV)	0.0	0.80	2.10	2.60	3.05
PEN (MeV)	2.881	2.090	0.842	0.449	0.415
VSQ (%)	0.4	0.8	5.0	21.3	73.1

spectra. Our sensitivity allows the detection of peaks with intensities of at least 5% of the 840.9 keV transition.

1477.0 keV, $9/2^+, 11/2^+, 13/2^+$. In Ref. [3], a 668.48 keV γ transition depopulating the state at 1477.17(12) keV was reported. The analyses of conversion electrons suggest E1 characteristics for this transition; thus the possible spins of this state are $(7/2, 9/2, 11/2)^-$. In Refs. [24,25], a state at 1478.4(3) keV with a depopulating 669.8(3) keV γ transition was observed and the spin was assumed to be (13/2). Our $\gamma\gamma$ coincidence spectra show a 668.4(2) keV transition, without a broadened peak width, depopulating the state at 1477 keV. In Fig. A.1, different spin hypotheses for the (668, 550) γ cascade are shown. The possible spins of this state can be limited to 9/2, 11/2 or 13/2. The corresponding multipole mixing ratios are $\delta_{9/2} = +0.28(17)$, $\delta_{11/2} = +0.47(8)$ and $\delta_{13/2} = +0.02(9)$, respectively. While the $13/2 \xrightarrow{668} 9/2_1 \xrightarrow{550} 5/2$ spin hypothesis reproduces the angular correlation best, other spin hypotheses for the 1477 keV state cannot be discarded. The determination of the multipole mixing ratio excludes a pure E1 characteristic for the 668.4 keV transition.

5. Interacting Boson Fermion Model calculation

The nucleus ^{193}Au was first examined within the U(6/4) limit of the IBFM by Wood [5]. In this publication, E2 transition strengths were calculated. Unfortunately, only the lifetimes of the $J^\pi = 1/2^+_1$ state at 38.2 keV, the $J^\pi = 5/2^+_1$ at 258.0 keV and an upper limit for the lifetime of the $J^\pi = 3/2^+_2$ state at 224.8 keV were known (see Ref. [1]). A theoretical level scheme was established for states assigned with the quantum numbers up to $(\tau_1, \tau_2) = (5/2, 1/2)$ of the O(5) symmetry.

Based on the new data (see Table 1), a more detailed discussion of the nucleus becomes feasible. The newly determined states with positive-parity allow an investigation of levels with spin up to $J^\pi = 11/2^+$. In addition, newly assigned spins and new transitions allow an improved assignment of theoretical eigenstates to experimental states. With the new data, we can test the basic assumption used in Ref. [5], that primarily the $d_{3/2}$ orbital contributes to the low-lying excited states in ^{193}Au. Therefore, we performed new calculations within the framework of the IBFM, based on a quasi-particle populating the $g_{7/2}$, $d_{5/2}$, $h_{9/2}$, $d_{3/2}$, $s_{1/2}$ orbitals (see Section 2). Thus, the population of all possible orbitals, between the shell closures at $Z = 50$ and $Z = 82$ for the unpaired proton, are taken into account. Using the BCS formalism [29], the quasi-particle energies PEN(k) and the occupation probabilities VSQ(k) are derived from single-particle energies SPE(k) of the orbitals k. The single-particle energies are based on values for nuclei with mass $A = 207$, given in Ref. [30], and only the energy of the $s_{1/2}$ is slightly modified to accommodate for ^{193}Au (cf. Table 2). For the parametrization of the bosonic core, the IBM-2 calculation of

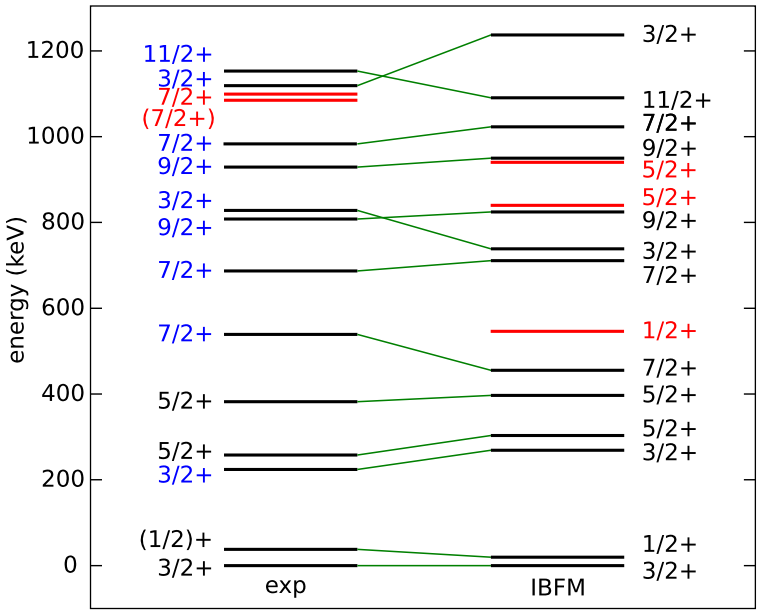

Fig. 3. (Color online.) States predicted in the IBFM (right) compared to the experimental level scheme of ^{193}Au (left). All states have positive parity. Newly determined spins are given in blue. States, either predicted but not observed in experiment or vice versa, are labeled red.

^{194}Hg from Barfield et al. [31] was adopted. In this work two IBM-2 Hamiltonians are coupled, in order to simulate the mixing of 2p–2h intruder states with the 0p–0h configuration in the Hg chain. However, the influence of the intruder configuration can be neglected for the low-lying excited states in ^{194}Hg, thus, the parameters of the 0p–0h configuration are used for the calculation. Similarly to Ref. [13], it is assumed that the parameter χ is the average of the corresponding neutron and proton IBM-2 parameters, χ_ν and χ_π, $\chi = \frac{1}{2}(\chi_\nu + \chi_\pi)$. The IBM-2 Hamiltonian was mapped to the IBM-1 Hamiltonian. Using the *ODDA* code [32], a least squares fit was performed for the pseudo-yrast band of the ^{193}Au nucleus up to spin $J^\pi = 9/2^+$ and the second excited spin $J^\pi = 3/2^+, 5/2^+, 7/2^+$ states, yielding the parameters BFE $= -0.64$, BFQ $= 0.10$, BFM $= -0.14$ MeV for the boson-fermion interaction.

Fig. 3 compares theoretical predictions with experimental results. The predicted states were assigned to observed states with regard to level energy, B(E2) transition strength (see Table 4) and relative B(E2) values (see Table 5). The agreement is very good, even reproducing the ordering of levels, except for the third and fourth $J^\pi = 3/2^+$ state. States predicted by theory, but not observed in experiment, are labeled in red. In the case of the second excited $J^\pi = 1/2^+$ state, reaction kinematics limits the possibility to observe this state. States with spin $J = 7/2$ are most likely populated after the (p, 2n) reaction with a proton beam energy $E_p = 14$ MeV. In the neighboring odd–even gold isotopes ^{191,195}Au a second excited $J^\pi = 1/2^+$ state is either not known or questionable (at 841 keV a state is observed which assigned with spin 1/2 and 3/2 [33], but a new angular correlation measurement confirms a spin of 3/2 for this state [34]), so there is no indication at what energy this state might be observed. Note, that all states predicted by theory, but not observed in experiment, have in the IBFM calculation a considerable contribution of the $s_{1/2}$ orbital in their wave functions. The calculations show, that B(E2) values for transitions connecting these states to states without significant contribution of the $s_{1/2}$ orbital are predicted to be small. Table 3 lists the contributions of all four orbitals with positive parity to states given in Fig. 3. The prediction, that the second excited $J^\pi = 1/2^+$ state, at 530 keV, is the first state with

Table 3
Single-particle contribution of the four orbitals with positive-parity to wave functions of states predicted by the IBFM calculations. States labeled with – were not observed in the experiment.

E_{theo} [keV]	E_{exp} [keV]	J^π	$s_{1/2}$	$d_{3/2}$	$d_{5/2}$	$g_{7/2}$
0	0	$3/2^+$	0.6	95.8	1.5	2.0
19	38	$1/2^+$	0.1	95.1	3.6	1.2
257	224	$3/2^+$	3.9	91.1	4.3	0.7
294	258	$5/2^+$	0.4	96.5	1.7	1.4
395	382	$5/2^+$	0.4	95.3	3.5	0.9
456	539	$7/2^+$	0.6	94.8	1.9	2.6
536	–	$1/2^+$	65.3	33.4	1.0	0.3
703	687	$7/2^+$	4.3	91.2	3.9	0.6
733	828	$3/2^+$	1.1	95.3	2.6	1.0
822	808	$9/2^+$	0.4	96.5	1.8	1.3
871	–	$5/2^+$	38.1	57.5	4.0	0.5
938	–	$5/2^+$	57.3	37.9	3.6	1.2
950	929	$9/2^+$	0.5	95.5	3.2	0.8
1020	983	$7/2^+$	0.5	92.9	3.2	3.4
1081	1153	$11/2^+$	0.6	93.0	2.7	3.8
1224	1119	$3/2^+$	68.5	27.7	2.3	1.5

more than 30% contribution from the $s_{1/2}$ orbital, corresponds to measurements of $s_{1/2}$ transfer strength in ^{196}Au, which revealed that low-lying states exhibit only small contributions of the $s_{1/2}$ orbital [9]. Unfortunately, as no state with considerable contribution of the $s_{1/2}$ orbital is observed, it is difficult to fix the single-particle energy for this orbital. Instead, the chosen single-particle energy $\text{SPE}(s_{1/2}) = 3.05$ MeV is a lower limit. At around 1.1 MeV the fourth and fifth $J^\pi = 7/2^+$ states are observed (see Fig. 3), which are not predicted by the IBFM calculations. Hence, we can assume, that at this energy, admixtures outside of the valence space of the model are becoming increasingly important.

Furthermore, theoretical $B(\text{E2})$ values are calculated using the definition of the transition operator (see Section 7) and compared to experimental values to show, whether the model is able to reproduce wave function sensitive properties of the states. The comparison is given in Table 4 and shows a very good agreement between experiment and theory.

Since both $B(\text{E2})$ values and level energies show, that those states, which are experimentally observed, have mainly contributions from the $d_{3/2}$ orbital, with the noted exceptions, it seems valid to assume the U(6/4) limit for most of the positive-parity states below 1.1 MeV in ^{193}Au.

6. Bose–Fermi symmetry in ^{193}Au

The IBFM in the U(6/4) limit couples seven bosons to a fermion in the $2d_{3/2}$ proton orbital, leading to a Hamiltonian constructed from Casimir operators of the $\text{U}^{\text{B}}(6) \otimes \text{U}^{\text{F}}(4)$ algebra. Only positive-parity states are generated. The group chain in the O(6) limit and the associated eigenfunction are given in Eqs. (10) and (12).

Again, to compare the theory to data, we assigned experimentally observed states to theoretically predicted levels and fitted Eq. (12) to the data by a least-squares fit. The first two experimental states with spins $J^\pi = 3/2^+, 5/2^+, 7/2^+$ and the first $J^\pi = 1/2^+, 9/2^+, 11/2^+$ states were used for the fit. The program code ARBMODEL [35] was employed for performing the

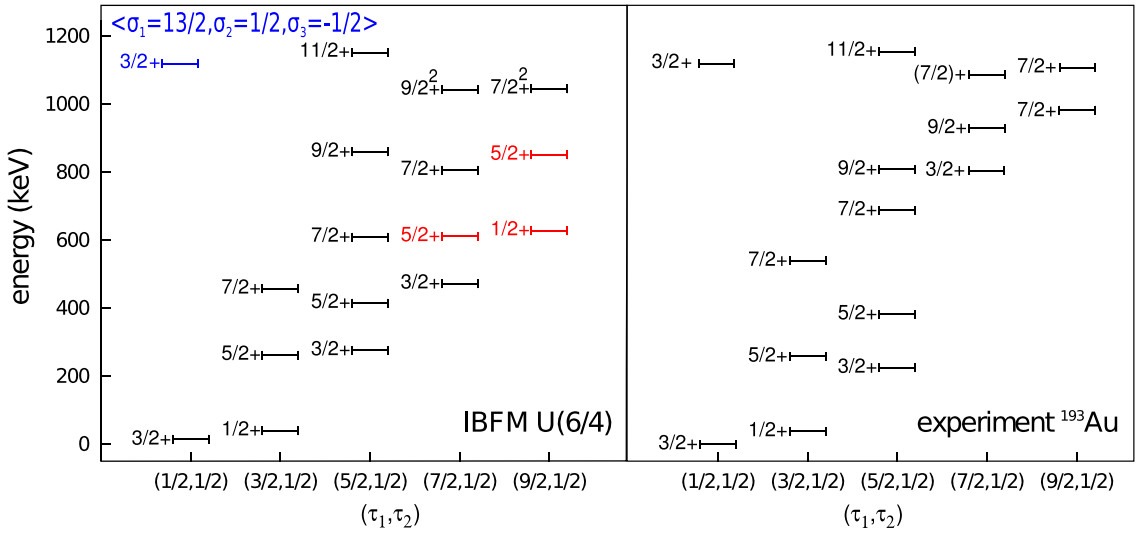

Fig. 4. (Color online.) States predicted in the IBFM compared to the experimental level scheme of ^{193}Au. All states have positive-parity. The spins of the states are given next to the levels. The parameters are $A = -0.0622$, $B = 0.0213$, $C = 0.0289$ MeV. All states are from the same σ_1, σ_2, σ_3 multiplet, except the state assigned to the fourth $3/2^+$ and is labeled in blue. A superscripted two, next to the spins, labels two degenerate states.

calculations. The result is shown in Fig. 4, whereby the parameters $A = -0.0622$, $B = 0.0213$, $C = 0.0289$ MeV were used. The different (τ_1, τ_2) multiplets were chosen for the x axis. All theoretically predicted states have the same σ and $\sigma_1 = 15/2$, $\sigma_2 = 1/2$, $\sigma_3 = 1/2$ quantum numbers, except for the fourth $J^\pi = 3/2^+$ labeled in blue. This assignment represents an upper limit for the O(6) splitting at $A = -0.0622$ MeV and is discussed in Section 7. States labeled in red are predicted in theory but not observed in experiment. Note, that some predicted states are degenerate and indicated with a superscripted two. This refers to a "missing label", which means that two degenerate states are produced by repeated occurrence of an irreducible representation of a sub-algebra in an embedding algebra [18]. Since the used Hamiltonian is a linear combination of Casimir operators with respect to the algebraic chain of Eq. (11), the observed splitting (see the $J^\pi = 7/2_3^+$ and $7/2_5^+$ states in Fig. 4) cannot be reproduced by the calculation. The splitting of the $J^\pi = 7/2^+$ state of the $\tau_1 = 9/2$ multiplet (to simplify matters only τ_1 is mentioned in the following sections, as τ_2 is always equal to $1/2$), and its depopulating transitions, is discussed in more detail in Section 7.

The fit describes the level scheme of the $\tau_1 = 1/2, 3/2, 5/2$ multiplets generally well, considering we are using a two-parameter Hamiltonian only. However, we are not able to reproduce the straggling of the experimental levels within the $\tau_1 = 5/2$ multiplet. That might be due to other effects, not considered within the O(6) limit, such as Coriolis mixing. In the $\tau_1 = 7/2$ multiplet, we observe the order of $J^\pi = 7/2^+, 9/2^+$ to be reversed, with respect to the experimental level scheme, and the predicted energy of the third $J^\pi = 3/2^+$ state to differ significantly from the energy of the observed $J^\pi = 3/2^+$ state. Interestingly, the same problem as in the full IBFM calculation arises, that no candidate is observed for the predicted $J^\pi = 5/2_{3,4}^+$ and $J^\pi = 1/2_2^+$ state. The IBFM calculations, above, show that it is beyond the scope of the U(6/4) limit to correctly predict these states, due to the admixture of the $s_{1/2}$ orbital (see Section 5). Hence the O(6)-symmetry starts to break at $\tau_1 \geqslant 7/2$. To clarify the nature of, in particular, the $\tau_1 = 7/2$ multiplet, we investigate transition strengths and decay characteristics in the following section.

Table 4
Theoretical E2 transition strengths compared to experimental values from [28] and from this work. For the lifetime of the state at 224.8 keV, only an upper limit is known. The angular correlation analysis of the 189.6 keV transition cannot exclude a pure M1 characteristic and is labeled with †.

E_{level} [keV]	E_γ [keV]	$B(\text{E2})_{\text{IBFM}}$ [$e^2\text{b}^2$]	$B(\text{E2})_{\text{U(6/4)}}$ [$e^2\text{b}^2$]	$B(\text{E2})_{[28]}$ [$e^2\text{b}^2$]	$B(\text{E2})_{\text{exp}}$ [$e^2\text{b}^2$]
38.2	38.2	0.304	0.304	0.304(80)	
224.8	189.6	0.057	0.150	> 0.072	$\geqslant 0.0^\dagger$
	224.8	0.065	0	> 0.044	$\geqslant 0.053$
258.0	219.8	0.132	0.108	0.093 (46)	0.101 (2)
	258.0	0.264	0.304	0.205 (93)	0.272 (5)

7. Transition strengths and decay characteristics

In the IBFM, the general E2 transition operator is defined as [14]

$$T^{\text{E2}}_\mu = \alpha_2\big[s^\dagger \times \tilde{d} + d^\dagger \times \tilde{s}\big]^{(2)}_\mu + \beta_2\big[d^\dagger \times \tilde{d}\big]^{(2)}_\mu + \sum_{j \leqslant j'} \frac{\epsilon^2_{jj'}}{1+\delta_{jj'}}\big[\big[a^\dagger_j \times \tilde{a}_{j'}\big]^{(2)}_\mu + (-1)^{j-j'}\big[a^\dagger_{j'} \times \tilde{a}_j\big]^{(2)}_\mu\big], \tag{15}$$

with

$$\epsilon^2_{jj'} = -\frac{f_2}{\sqrt{5}}\left\langle l_j \tfrac{1}{2} j \middle|\middle| T(\text{E2}) \middle|\middle| l_{j'} \tfrac{1}{2} j' \right\rangle, \tag{16}$$

where α_2 and β_2 are the effective boson charge and f_2 is the effective fermion charge. The parameter β_2 is equal to the parameter $\alpha_2 \times \chi$ (see Section 5). The fermion charge was set to $-f_2 = \alpha_2 = 0.06632$ eb, to reproduce the transition strength from the first excited state at 38.3 keV to the ground state. The E2 transition operator for the U(6/4) limit is defined as

$$T^{\text{E2}}_\mu = \alpha_2\big[s^\dagger \times \tilde{d} + d^\dagger \times \tilde{s}\big]^{(2)}_\mu + f_2\big[a^\dagger \times \tilde{a}\big]^{(2)}_\mu, \tag{17}$$

where $B^2_\mu = [s^\dagger \times \tilde{d} + d^\dagger \times \tilde{s}]^{(2)}_\mu$ are generators of the $\text{O}^{\text{B}}(6)$ and $A^2_\mu = [a^\dagger \times \tilde{a}]^{(2)}_\mu$ represent the $\text{SU}^{\text{F}}(4)$ generators [16]. The selection rules for the E2 transition operator are $\Delta\tau_1 = 0, \pm 1$, $\Delta\tau_2 = 0$. As already mentioned, the lifetimes, or the upper limit, are only known for the three lowest states and some isomeric negative-parity states. Again, the $B(\text{E2}, 1/2^+_1 \xrightarrow{38.2} 3/2^+_{\text{gs}})$ value is used to determine the parameters $\alpha_2 = f_2 = 0.1345$ eb.[1] The parameter α_2 is similar to the parameters known in the E2 operators in other Au isotopes [36]. The lifetime of the $J^\pi = 5/2^+_1$ state was taken from Ref. [1], the multipole mixing ratio and the branching ratio from this work. In Table 4, the calculated $B(\text{E2})$ values are compared to transition strengths taken from NDS [28] and from this work. The comparison reveals a good agreement between theoretical and experimental data. Only the presence of E2 strength in the 224.8 keV transition is not reproduced very well.

[1] The following phase convention is used in ARBMODEL [35]: $(-1)^{j+m}c_{j-m}$, where c is a boson or fermion annihilation operator.

Table 5
Experimental relative B(E2) transition strengths compared to theoretical relative B(E2) values. The transition with the largest B(E2) value among the depopulating decays of the same level is normalized to 1. If the multipole mixing ratio is not known but the spin difference between initial and final state is $\Delta l = 2$, a pure E2 characteristic is assumed, and the B(E2) value is labeled with *. Relative B(E2) values labeled with – are forbidden in the U(6/4) limit. No E2 transition strengths from the full IBFM calculation for transitions depopulating the 1085 and 1153 keV states are given as no appropriate candidates are predicted.

E_{initial} [keV]	J^{π}_{initial}	E_{final}	J^{π}_{final}	E_{γ} [keV]	$B(\text{E2})^{\text{IBFM}}_{\text{rel}}$	$B(\text{E2})^{\text{U(6/4)}}_{\text{rel}}$	$B(\text{E2})^{\text{exp}}_{\text{rel}}$
538.9	$7/2^+$	258.0	$5/2^+$	280.9	0.14	0.23	0.02(2)
		0.0	$3/2^+$	538.9	1.00	1.00	1.00
687.5	$7/2^+$	381.6	$5/2^+$	305.9	0.02	0.14	0.42(8)
		258.0	$5/2^+$	429.4	0.08	1.00	0.92(17)
		224.8	$3/2^+$	462.6	1.00	0.07	1.00
		0.0	$3/2^+$	687.5	0.01	–	0.29(5)*
808.6	$9/2^+$	538.9	$7/2^+$	269.6	0.20	0.27	0.07(3)
		381.6	$5/2^+$	427.0	0.38	0.07	0.11(4)*
		258.0	$5/2^+$	550.6	1.00	1.00	1.00
828.0	$3/2^+$	381.6	$5/2^+$	446.4	1.00	0.25	0.28(11)
		224.8	$3/2^+$	603.2	0.02	1.00	1.00
		0.0	$3/2^+$	828.0	< 0.01	–	34(21)
929.1	$9/2^+$	687.5	$7/2^+$	241.7	0.02	0.07	0.28(8)
		538.9	$7/2^+$	390.1	< 0.01	–	0.01(1)
		381.6	$5/2^+$	547.5	1.00	1.00	1.00
983.6	$7/2^+$	258.0	$5/2^+$	725.6	1.00	–	1.00
		224.8	$3/2^+$	758.8	0.06	1.00	0.52(10)
1085.3	$(7/2)^+$	381.6	$5/2^+$	703.7		0.06	0.05(1)
		258.0	$5/2^+$	827.5		–	< 0.01
		224.8	$3/2^+$	860.5		100	1.00*
1106.0	$7/2^+$	828.0	$3/2^+$	277.1		1.00	1.00*
		538.9	$7/2^+$	567.1		–	< 0.01
		381.6	$5/2^+$	724.3		–	< 0.01
		258.0	$5/2^+$	848.2		–	< 0.01
1153.5	$11/2^+$	808.6	$9/2^+$	344.9	0.03	0.11	< 0.01
		538.9	$7/2^+$	614.7	1.00	1.00	1.00

As no further lifetimes are known, an alternative way to test the model is to look at relative transition strengths. The experimental relative strengths are listed in Table 5. The strongest B(E2) value among the depopulating transitions is normalized to 1, and is compared to the other transitions. The relative E2 strengths show good agreement between theoretical and experimental values for transitions of the $\tau_1 = 3/2, 5/2$ multiplets, except for the depopulating transitions of the 687 keV state. Here, the E2 strength of the 429 and the 462 keV are almost equally strong. This cannot be reproduced by the calculations. In fact, the models predict, that either the 429 (IBFM) or the 462 keV transition U(6/4) has the largest B(E2) value. The comparison of the wave functions of the second and third $7/2^+$ states show, that these states are interchanged. The present data does not allow an assessment of the correct assignment for the second and third $7/2^+$. The comparison of the relative B(E2) values favor an assignment of the 1085.3 keV state as a member of the $\tau_1 = 7/2$ multiplet. Interestingly, even though the degenerate $7/2_{4,5}$ states seem to split in experiment, the selection rules predicted by the U(6/4) limit are still fulfilled.

Table 6
Comparison of measured multipole mixing ratios from this work with calculated values derived from the IBFM in U(6/4) limit.

E_{level} [keV]	E_γ [keV]	δ_{theo}	δ_{exp}
258.0	258.0	−0.80	−0.75 (11)
538.9	280.9	−0.22	−0.06 (3)
687.5	305.9	+0.35	$+0.44^{+22}_{-19}$
	429.4	−1.28	-0.19^{+2}_{-3}
808.6	269.6	−0.44	−0.13 (7)
828.0	446.4	+0.15	−0.30 (7)
	603.2	+0.47	$+0.50^{+36}_{-28}$
929.1	241.7	−2.74	−0.12 (5)
1153.5	344.9	−0.19	−0.02 (5)

B(M1) values can also be used to test the model. Again, as no experimental absolute values are available, relative M1 transition strengths might be used. The definition of the M1 operator is as follows [16]:

$$T^{\text{M1}}_{\mu} = \beta_1 \big[d^\dagger \times \tilde{d}\big]^{(1)}_{\mu} + \frac{t_1}{\sqrt{2}} \big[a^\dagger_{\frac{3}{2}} \times \tilde{a}_{\frac{3}{2}}\big]^{(1)}_{\mu}, \tag{18}$$

where the parameters $t_1 = 0.09\mu_N$ and $\beta_1 = 0.662\mu_N$ were obtained by fitting Eq. (18) to the magnetic moment of the ground state [37] ($\mu(\frac{3}{2}^+) = 0.1396\ (5)\mu_N$) and the known M1 fraction of the transition of the $J^\pi = \frac{5}{2}^+_1$ state to the ground state ($B(\text{M1}) = 0.021(16)\mu_N^2$, lifetime adopted from [1]).[2] Both parameters are similar to those given in IBFM calculations for nuclei in this region [16]. Unfortunately, we did not observe sufficient depopulating M1 transitions of the same state to compare among each other, so no conclusions can be drawn. Again, lifetimes are needed to test the predicted M1 transition strengths of the IBFM.

However, with the definition of the M1 operator, the multipole mixing ratio δ can be tested with the following equation [38]:

$$\delta = 0.835 \times E_\gamma(\text{MeV}) \frac{\langle I_f || T(\text{E2}) || I_i \rangle}{\langle I_f || T(\text{M1}) || I_i \rangle}. \tag{19}$$

In Table 6, the theoretical multipole mixing ratios of allowed transitions are compared to our data. Generally, the calculated multipole mixing ratios, and thus, the E2 strength, of a transition are always predicted to be larger than observed in experiment. One major reason might be the overestimation of the effective boson charge. It was chosen to reproduce the B(E2) value of the transition $1/2^+_1 \xrightarrow{38.2} 3/2^+_{\text{gs}}$. The uncertainty for this B(E2) value allows a significantly lower effective boson charge thereby allowing the multipole mixing ratios to decrease. Note, that a different boson charge will not change the calculated relative B(E2) values in Table 5. Overall, except for the 429 and 241 keV transitions, reasonably good agreement with the experimental values is achieved.

[2] The calculation of B(M1) values using the IBFM with all five orbitals is omitted, as the operator depends on effective single-particle g-factors for all five orbitals. All together, this would lead to eleven parameters, which would have to be adjusted.

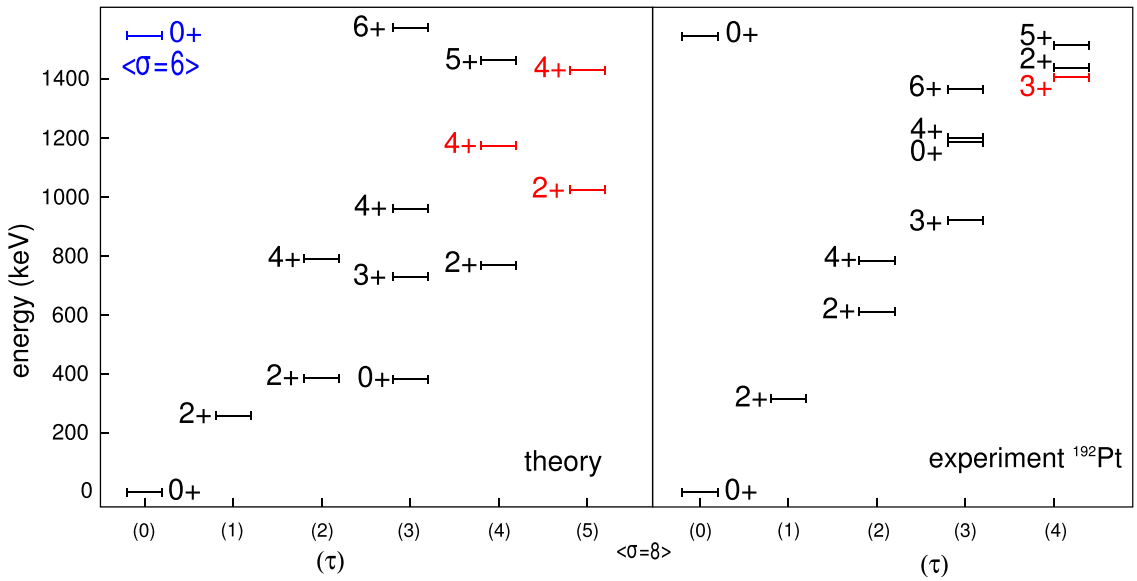

Fig. 5. (Color online.) States predicted by the IBFM with the parameters obtained from the fit to the data of ^{193}Au and compared to the level scheme of ^{192}Pt. Only with states of positive parity were considered. The parameters are $\bar{A} = -0.0432$, $B = 0.0213$, $C = 0.0289$ MeV. All states are from the same σ multiplet, except the state assigned to the third 0^+ and is labeled in blue. States either predicted but not observed in experiment or vice versa are labeled red.

8. The supersymmetric partner ^{192}Pt

We can now use the properties of the IBFM Hamiltonian in the U(6/4) limit to describe the neighboring ^{192}Pt nucleus, that is eight bosons away from shell closures at $N = 126$ and $Z = 82$. According to the supersymmetry between bosons and fermions (see Eq. (13)), the fermion is transformed into a boson, but the system is still described by the same set of parameters. In fact, the Hamiltonian is the one of the O(6) limit [39] with the eigenfunction of Eq. (14). Only parameter D of the $SO^B(6)$ group has to be fitted to the Pt data, since the parameter $\bar{A}$ is composed of $\bar{A} = D + A$. In the previous fit to the nucleus ^{193}Au, parameter D was chosen in such a way that only levels with quantum number $\sigma = 7$ are relevant for the fit. For the assignment of theoretical predicted states to the experimentally observed states, IBM calculations performed in Ref. [39] on ^{196}Pt were used. Consistent with Ref. [39], the third 0^+ state in ^{192}Pt was assigned to the $\sigma = 6$ ($\sigma = N_{\max} - 2$) multiplet, determining the parameter $\bar{A} = -0.0432$ MeV. Fig. 5 shows the comparison of the experimental and theoretical level scheme. Experimental data of ^{192}Pt was taken from Refs. [40–43]. Fig. 5 reveals that the observed states are not reproduced very well; especially the $J^\pi = 0_2^+$ state predicted at 383 keV has not been observed. As the nucleus ^{192}Pt was studied with (p,t) reactions [41,43] and no 0^+ state was observed between 500 and 1000 keV, it is questionable, whether the predicted state exists. Furthermore, no experimental state is assigned to the $\tau = 5$ multiplets, as they do not agree with the expected decay characteristics.

To achieve a better fit, states of both nuclei, ^{192}Pt and ^{193}Au, were used. For the fit, in addition to the states in ^{193}Au (see Section 6), the yrast band up to the 4^+ and the $0_{2,3}^+$, 2_2^+, 4_2^+ states in ^{192}Pt were considered. The comparison of the theoretical level scheme using the new parameters $\bar{A} = -0.0432$ MeV, $B = 0.0403$ MeV, $C = 0.0173$ MeV is presented in Fig. 6. The new parameters have values similar to the parameters in Refs. [36,39]. The 0_2^+ state is now predicted at 725 keV and fits better to the observed second 0^+ state. The remaining difference in energy

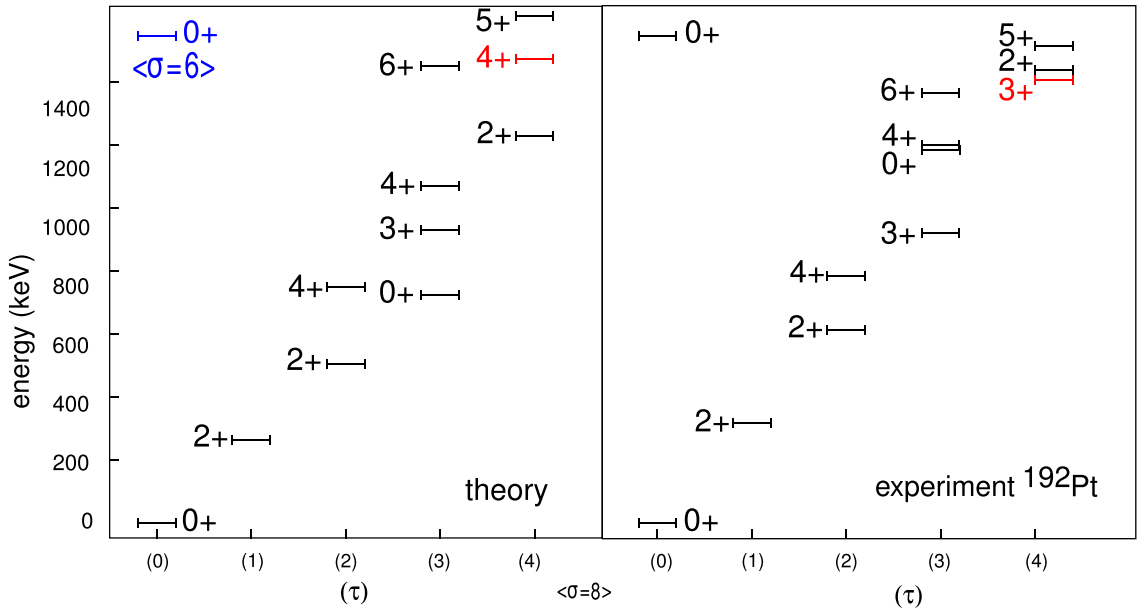

Fig. 6. (Color online.) States predicted by the IBFM with the parameters obtained from the simultaneous fit to the nuclei ^{193}Au and ^{192}Pt, in comparison with the level scheme of ^{192}Pt. Only states with positive parity were considered. The parameters are $\bar{A} = -0.0432$, $B = 0.0403$, $C = 0.0173$ MeV and the parameters A and D are connected by $\bar{A} = D + A$. All states are from the same σ multiplet, except the state assigned to the third 0^+ and is labeled in blue. States either predicted but not observed in experiment or vice versa are labeled red.

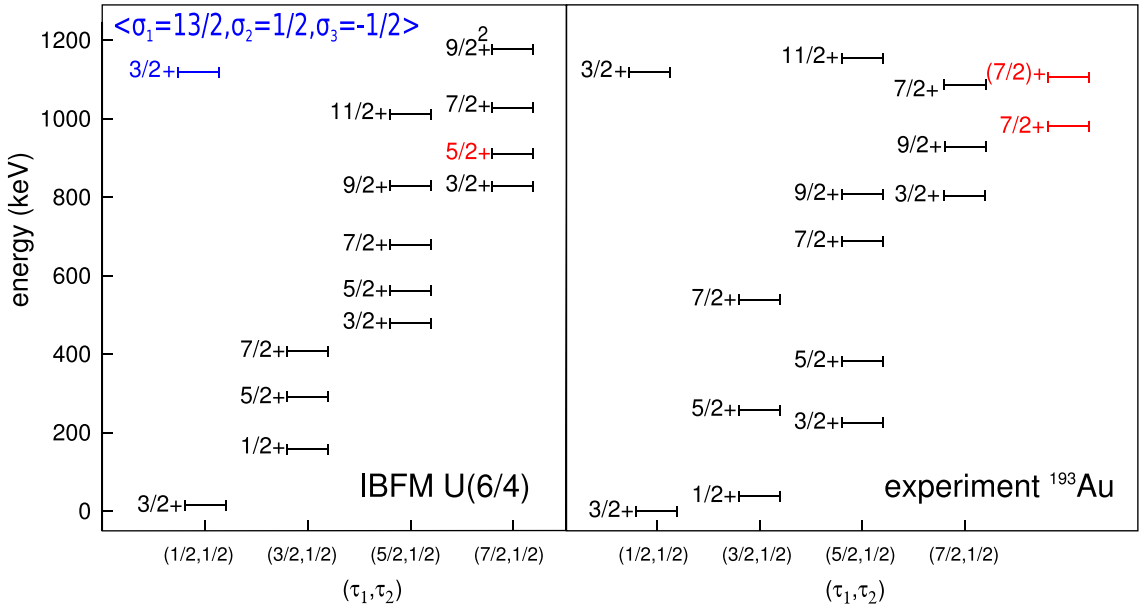

Fig. 7. (Color online.) States predicted by the IBFM with the parameters obtained from the simultaneous fit to the nuclei ^{193}Au and ^{192}Pt, and compared to the level scheme of ^{193}Au, considering states with positive parity only. The parameters are $A = -0.0622$, $B = 0.0403$, $C = 0.0173$ MeV. All states are from the same σ_1, σ_2, σ_3 multiplet, with the exception of the fourth $3/2$, which is labeled in blue. States either predicted but not observed in experiment or vice versa are labeled red.

might be due to neglecting the three-body interaction [44–46]. As the second 0^+ state is generated partly by three d bosons, this might be an major contribution. Overall, the predicted states generated with the new parameters are more consistent with experimental data. However, the theoretical level scheme of ^{193}Au generated by the new parameters (see Fig. 7) is not able to describe

the ordering of observed states in the $\tau_1 = 3/2, 5/2$ multiplet as well as the old parameters, but decay characteristics and transitions strength are still reproduced. Hence, a supersymmetric description of the transition strengths and decay probabilities of the low-lying excited states in ^{192}Pt and ^{193}Au is possible. In contrast, the $3/2^+$ and $7/2^+$ state of the $\tau_1 = 7/2$ multiplet now show a better agreement with experimental data. The difference between the two set of parameters seems to result from varying strengths of the O(5) parameter, as this generates the τ splitting. In ^{193}Au, the first $J^\pi = 1/2^+$ of the $\tau_1 = 3/2$ multiplet is low in energy with respect to the ground state; thus, the τ splitting is small in order to generate the first excited state, whereby one fermion has to couple with one d boson by annihilating one s boson. In contrast to this, the first excited state in ^{192}Pt and especially the second 0^+ state, which is a member of the $\tau = 3$ multiplet, is predicted too low. Thus, a larger τ splitting is needed in ^{192}Pt. In order to incorporate this difference in energy, a three-body interaction or a U(5) term has to be introduced, thereby breaking the O(6) symmetry.

9. Conclusion

A wealth of new data is presented in this work. 49 states were investigated, 15 of them previously unknown. Using $\gamma\gamma$ coincidence spectra, more than 120 γ transitions, assigned to the nucleus ^{193}Au, were investigated regarding their multipolarities and branching ratios. This enabled us to determine the spins of several states.

The comparison of a general IBFM calculation to the new data allows a better understanding of the limit of the Bose–Fermi symmetry. While states, which are member of the $\tau = 1/2, 3/2, 5/2$ multiplet, show good agreement with data, some states predicted by both theories are not observed in experiment. The general IBFM calculation suggests a significant admixture from the $3s_{1/2}$ orbital to the wave functions of these states; thus, it cannot be expected to be reproduced by a simple IBFM calculation in the U(6/4) limit. Still, while the degeneracy of the fourth and fifth $J^\pi = 7/2^+$ state, a member of the $\tau = 9/2$ multiplet, is not valid anymore, the decay characteristics seem to be preserved. The experimentally determined E2 transition strengths of the depopulating transitions of the three lowest excited levels can be reproduced by both calculations. Furthermore, relative E2 transition strengths were compared and show good agreement for transitions between states in the lower energy region. Some transitions depopulating higher excited states are forbidden in the U(6/4) limit, which should be reflected by low absolute transition strengths. In order to test the accuracy of these predictions, lifetimes for higher excited states are needed.

Within the framework of the supersymmetric U(6/4) limit, the level scheme of ^{192}Pt was predicted, using parameters obtained from a fit to the nucleus ^{193}Au. A poor agreement is reached for most of the levels up to an excitation energy of 1600 keV. Therefore, a new set of parameters was obtained using the level schemes of both nuclei. This way, even though the agreement of separate IBFM fits to ^{193}Au and ^{192}Pt is not achieved, we successfully reproduce the experimental level scheme. We conclude, that we are able to establish a dynamical supersymmetry with only three parameters for ^{193}Au and ^{192}Pt.

Acknowledgements

We thank our coworkers and the Tandem accelerator staff at the IKP Köln for their help during the experiment. We thank F. Iachello, M. Elvers and V. Werner for fruitful discussions concerning this work.

Appendix A. $\gamma\gamma$ coincidence spectra and angular correlation analysis

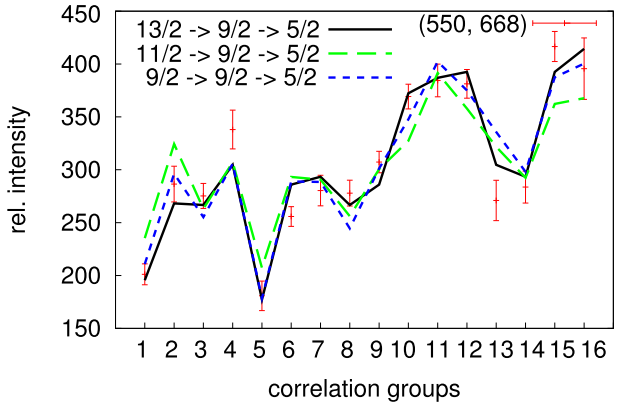

Fig. A.1. (Color online.) Different spin hypotheses are tested for the (550, 668) cascade. The corresponding multipole mixing ratios are $\delta_{9/2,668} = +0.282(167)$, $\delta_{11/2,668} = +0.465(76)$ and $\delta_{13/2,668} = +0.016(88)$. The spin of this state could not be determined unambiguously.

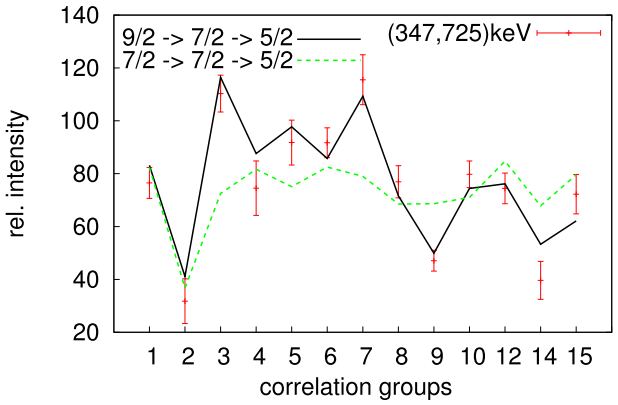

Fig. A.2. (Color online.) The fits for the spin hypotheses $9/2 \xrightarrow{347} 7/2_3 \xrightarrow{725} 5/2_1$ and $7/2 \xrightarrow{347} 7/2_3 \xrightarrow{725} 5/2_1$ are compared. The correlation groups 11, 13, 16 were removed due to low statistics. Clearly, a spin of $9/2$ is favored for the state at 1379 keV. The corresponding multipole mixing ratio is $\delta_{347} = -0.445(238)$.

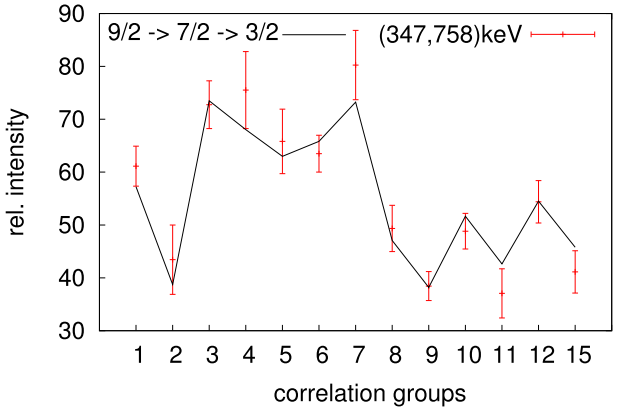

Fig. A.3. (Color online.) The fit for the spin hypothesis $9/2 \xrightarrow{347} 7/2_3 \xrightarrow{758} 3/2_2$ is shown. The correlation groups 13, 14, 16 were removed, due to low statistics. The corresponding multipole mixing ratio is $\delta_{758} = +0.02(21)$.

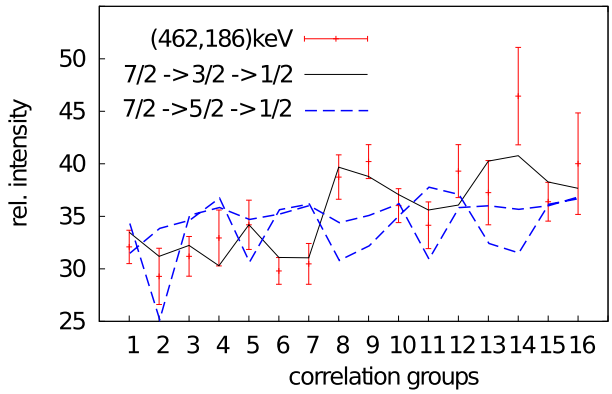

Fig. A.4. (Color online.) From angular correlation analysis of the (692,462) cascade the multipole mixing ratio of the 462 keV transition is determined to either exhibit a pure E2 characteristic, if the spin is $J_2 = 3/2$, or if the spin is $J_2 = 5/2$, the multipole mixing ratio is determined to be $\delta_{462} = +0.21(20)$ or $\delta_{462} = +12.0^{+8}_{-3}$. The fits for the spin hypotheses $7/2_2 \xrightarrow{462} 3/2 \xrightarrow{186} 1/2_1$ and $7/2_2 \xrightarrow{462} 5/2 \xrightarrow{186} 1/2_1$ with the two possible δ_{186} are compared. Clearly, the spin $J_2 = 3/2$ is favored and the corresponding multipole mixing ratio of the depopulating transition is $\delta_{186} = +0.11(15)$.

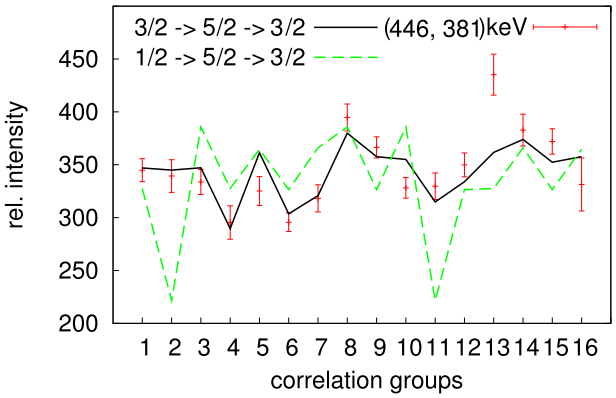

Fig. A.5. (Color online.) The fits for the spin hypotheses $3/2 \xrightarrow{446} 5/2_2 \xrightarrow{381} 3/2_1$ and $1/2 \xrightarrow{446} 5/2_2 \xrightarrow{381} 3/2_1$ are compared. For the 381 keV transition, the already measured multipole mixing ratio $\delta_{462} = -2.93$ from angular correlation analysis of the (547, 381) cascade (see also the discussion in 4 was used. The corresponding multipole mixing ratio for the 446 keV transition is $\delta_{186} = -0.30(7)$.

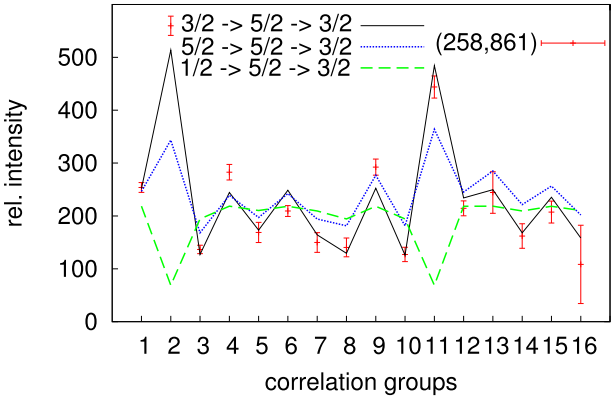

Fig. A.6. (Color online.) The spin hypotheses for $3/2 \xrightarrow{861} 5/2_1 \xrightarrow{258} 3/2_1$, $1/2 \xrightarrow{861} 5/2_1 \xrightarrow{258} 3/2_1$ and $5/2 \xrightarrow{861} 5/2_1 \xrightarrow{258} 3/2_1$ is shown. For the 258 keV transition, the multipole mixing ratio $\delta_{258} = -0.75(11)$ was used. The fits show that the spin 3/2 is clearly favored, but two multipole mixing ratios are possible (For the sake of clarity, only the spin hypothesis with $\delta_{861} = -1.33(40)$ is shown). In Section 4 the state at 1119 keV with the depopulating 861 keV transition is discussed in more detail.

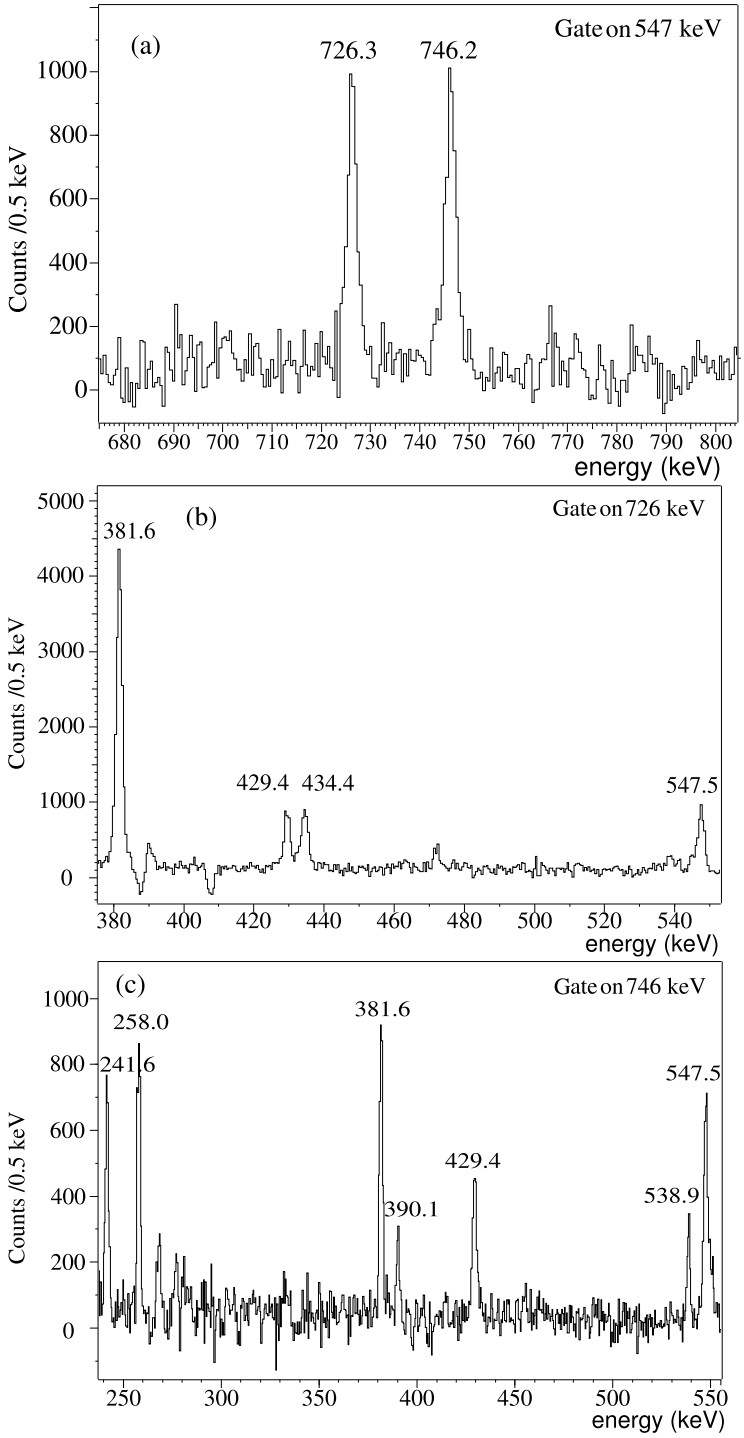

Fig. A.7. The top figure shows (a) $\gamma\gamma$ coincidence spectrum energy gated on the 547.5 keV transition from $J^\pi = 9/2_2^+$ state at 929.1 keV to the $J^\pi = 5/2_2^+$ state at 381.6 keV. Two new transitions with the energy 726.3 keV depopulating the state at 1655.4 keV and the energy 746.2 keV depopulating the state at 1675.3 keV are observed in the spectrum. The middle figure (b) shows a $\gamma\gamma$ coincidence spectrum, energy gated on the newly observed 726.3 keV transition to the $J^\pi = 9/2_2^+$ state at 929.1 keV. Coincident transitions at 381.6, 429.4, 547.5 keV are observed. The 381.6 keV peak is comparatively larger due to the coincidence with another transition at 724.3 keV. The 434.4 keV transition is observed due to the coincidence with a 725.6 transition. The negative peaks in the spectrum yield from background subtraction. A $\gamma\gamma$ coincidence spectrum, energy gated on the new 746.2 keV transition to the $J^\pi = 9/2_2^+$ state at 929.1 keV, is shown in the bottom figure (c). Coincident transitions at 381.6, 429.4, 547.5 keV are observed. The 381.6 keV peak is comparatively larger due to the coincidence with another transition at 724.3 keV. The 434.4 keV transition is observed due to the coincidence with a 725.6 keV transition.

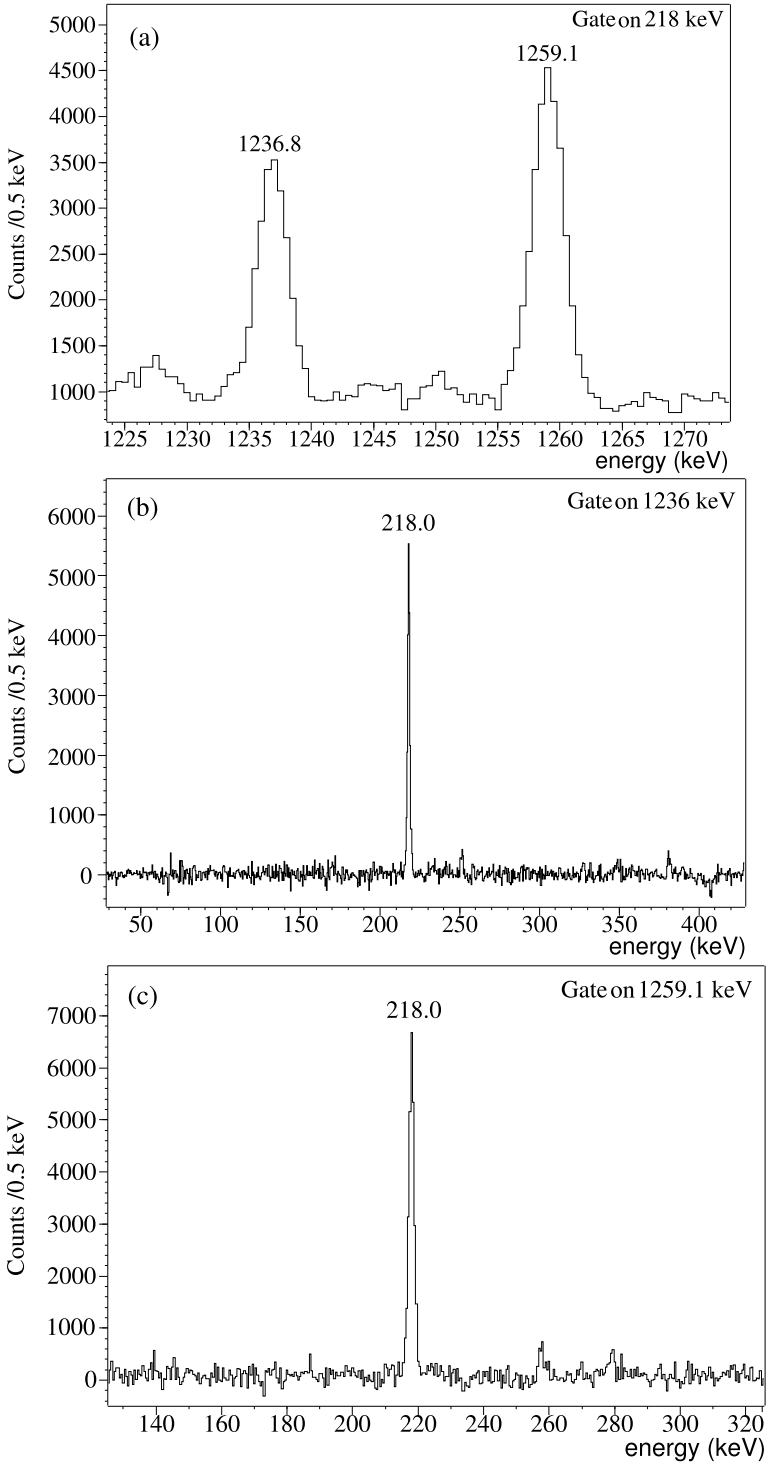

Fig. A.8. The top figure (a) shows a $\gamma\gamma$ coincidence spectrum, energy gated on the 218.0 keV transition from the $J^\pi = 7/2^-_1$ state at 508.1 keV to the isomeric $J^\pi = 11/2^-_1$ state at 290.2 keV. Two new transitions, with the energy 1236.8 keV depopulating the state at 1745.1 keV and the energy 1259.0 keV depopulating the state at 1767.1 keV, are observed in the spectrum. The middle figure (b) shows a $\gamma\gamma$ coincidence spectrum, energy gated on the newly identified 1236.8 keV transition to the $J^\pi = 7/2^-_1$ state at 508.1 keV. A $\gamma\gamma$ coincidence spectrum, energy gated on the new 1259.0 keV transition to the $J^\pi = 7/2^-_1$ state at 508.1 keV, is shown in the bottom figure. The coincident transition at 218.0 keV is observed.

Table A.1
Additional transitions E_γ observed in coincidence with a gated γ transition $E_{\mathrm{gate},\gamma}$. New transitions are labeled with *.

$E_{\mathrm{gate},\gamma}$ [keV]	E_γ [keV]	$E_{\mathrm{gate},\gamma}$ [keV]	E_γ [keV]
407	1097.3(3)	429	1212.0(5)*
	1171.5(3)	499	1115.6(3)*
	1178.7(3)	573	913.1(3)
	1232.4(4)		989.7(3)*
	1241.6(3)		1052.5(3)
	1314.5(3)		1174.1(3)
	1325.9(3)		1352.2(3)
	1339.7(3)	581	809.4(3)*
	1365.4(3)	675	422.2(3)
	1442.2(3)		545.1(3)
	1460.0(3)	721	528.2(4)
	1505.0(4)		
	1557.2(4)		

References

[1] B. Fogelberg, A. Baecklin, V. Berg, S.G. Malmskog, Nucl. Phys. A 153 (1970) 301.
[2] Y. Gono, R.M. Lieder, M. Müller-Veggian, A. Neskas, C. Mayer-Böricke, Nucl. Phys. A 327 (1979) 269.
[3] C.L.M. Vieu, PhD thesis, CSNSM-T-74-01, Orsay, 1974, unpublished.
[4] F. Iachello, Phys. Rev. Lett. 44 (1980) 772.
[5] J.L. Wood, Phys. Rev. C 24 (1981) 1788.
[6] P. Van Isacker, J. Jolie, K. Heyde, A. Frank, Phys. Rev. Lett. 54 (1985) 653.
[7] A. Metz, J. Jolie, G. Graw, R. Hertenberger, J. Gröger, C. Günther, N. Warr, Y. Eisermann, Phys. Rev. Lett. 83 (1999) 1542.
[8] J. Gröger, et al., Phys. Rev. C 62 (2000) 064304.
[9] H.-F. Wirth, et al., Phys. Rev. C 70 (2004) 014610.
[10] C. Bernards, S. Heinze, J. Jolie, C. Fransen, A. Linnemann, D. Radeck, Phys. Rev. C 79 (2009) 054307.
[11] C. Bernards, S. Heinze, J. Jolie, M. Albers, C. Fransen, D. Radeck, Phys. Rev. C 81 (2010) 024312.
[12] F. Iachello, O. Scholten, Phys. Rev. Lett. 43 (1979) 679.
[13] R. Bijker, L.E.A. Dieperink, Nucl. Phys. A 379 (1982) 221.
[14] O. Scholten, PhD thesis, University of Groningen, 1980, https://www.kvi.nl/~scholten/other/OlafsPhD-Thesis.pdf.
[15] A. de Shalit, I. Talmi, Nuclear Shell Theory, Academic Press, New York, USA, 1963.
[16] F. Iachello, P. Van Isacker, The Interacting Boson Fermion Model, Cambridge University Press, Cambridge, England, 1991.
[17] F. Iachello, S. Kuyucak, Ann. Phys. 136 (1981) 19.
[18] A. Frank, J. Jolie, P. Van Isacker, Symmetries in Atomic Nuclei – From Isospin to Supersymmetry, Springer, New York, USA, 2009.
[19] F. Pühlhofer, Nucl. Phys. A 280 (1977) 267.
[20] A. Linnemann, Ph.D. thesis, University of Cologne, 2005, http://kups.ub.uni-koeln.de/1747/.
[21] K.S. Krane, R.M. Steffen, Phys. Rev. C 2 (1970) 724.
[22] K.S. Krane, R.M. Steffen, R.M. Wheeler, At. Data Nucl. Data Tables 11 (1973) 351.
[23] I. Wiedenhöver, code CORLEONE, University of Cologne, 1995, unpublished.
[24] V. Kölschbach, P. Schüler, K. Hardt, D. Rosendaal, C. Günther, K. Euler, R. Tölle, M. Marten-Tölle, P. Zeyen, Nucl. Phys. A 439 (1985) 189–206.
[25] P.O. Tjom, M.R. Maier, D. Benson Jr, F.S. Stephens, R.M. Diamond, Nucl. Phys. A 231 (1974) 397–410.
[26] Y. Oktem, et al., Nucl. Phys. A 231 (1974) 397–410.
[27] V.K. Fischer, Phys. Rev. 99 (1955) 764.
[28] E. Achterberg, G.V. Marti, V.R. Vanin, et al., Nucl. Data Sheets 107 (2006) 1.
[29] J. Bardeen, N.L. Cooper, R.J. Schrieffer, Phys. Rev. C 108 (1957) 1175.
[30] L.S. Kisslinger, R.A. Sorensen, Rev. Mod. Phys. 35 (1963) 853.

[31] F.A. Barfield, R.B. Barrett, A.K. Sage, D.P. Duval, Z. Phys. A 311 (1983) 205.
[32] O. Scholten, 252 Computer Code ODDA, K.V.I. Internal Report, University of Groningen, 1980.
[33] Zhou Chunmei, Nucl. Data Sheets 86 (1998) 645.
[34] T. Thomas, private communication.
[35] S. Heinze, Ph.D. thesis, University of Cologne, 2008, http://kups.ub.uni-koeln.de/2357/.
[36] A. Frank, P. Van Isacker, Algebraic Methods in Molecular and Nuclear Structure Physics, Wiley-Interscience, New York, USA, 1994.
[37] G. Passler, J. Rikovska, E. Arnold, H.-J. Kluge, L. Monz, R. Neugart, H. Ravn, K. Wend, Nucl. Phys. A 580 (1994) 173–212.
[38] K.S. Krane, Phys. Rev. C 8 (1973) 1494.
[39] A. Arima, F. Iachello, The Interacting Boson Model, Cambridge University Press, Cambridge, England, 1987.
[40] C.M. Baglin, Nucl. Data Sheets 84 (1998) 717.
[41] P.T. Deason, C.H. King, T.L. Khoo, J.A. Nolen, F.M. Bernthal, Phys. Rev. C 20 (1979) 927.
[42] E.A. McCutchan, R.F. Casten, V. Werner, R. Winkler, R.B. Cakirli, G. Gürdal, X. Liang, E. Williams, Phys. Rev. C 78 (2008) 014320.
[43] G. Ilie, et al., Phys. Rev. C 82 (2010) 024303.
[44] Liao Ji-zhi, Wang Huang-sheng, Phys. Rev. C 49 (1994) 2465.
[45] K. Heyde, P. Van Isacker, M. Waroquier, J. Moreau, Phys. Rev. C 29 (1984) 1420.
[46] R.F. Casten, P. von Brentano, K. Heyde, J. Jolie, Nucl. Phys. A 439 (1985) 289.
[47] T. Kibedi, T.W. Burrows, M.B. Trzhaskovskaya, P.M. Davidson, C.W. Nestor, Nucl. Instrum. Methods Phys. Res., Sect. A, Accel. Spectrom. Detect. Assoc. Equip. 589 (2008) 202.

Available online at www.sciencedirect.com

ScienceDirect

Nuclear Physics A 925 (2014) 96–111

NUCLEAR PHYSICS A

www.elsevier.com/locate/nuclphysa

Bose–Fermi symmetry in the odd–even gold isotopes

T. Thomas [a,*], J.-M. Régis [a], J. Jolie [a], S. Heinze [a], M. Albers [a,b], C. Bernards [a,c], C. Fransen [a], D. Radeck [a]

[a] *Institute for Nuclear Physics, University of Cologne, Zülpicher Straße 77, D-50937 Köln, Germany*
[b] *Physics Division, Argonne National Laboratory, Argonne, IL 60439, USA*
[c] *WNSL, Yale University, P.O. Box 208120, New Haven, CT 06520-8120, USA*

Received 8 January 2014; received in revised form 5 February 2014; accepted 7 February 2014

Available online 15 February 2014

Abstract

In this work the results of an in-beam experiment on ^{195}Au are presented, yielding new spins, multipole mixing ratios, and new low-lying states essential for the understanding of this nucleus. The positive-parity states from this work together with compiled data from the available literature for $^{185–199}$Au are compared to Interacting Boson Fermion Model calculations employing the Spin(6) Bose–Fermi symmetry. The evolution of the parameters for the τ splitting and the J splitting reveals a smooth behavior. Thereby, a common description based on the Bose–Fermi symmetry is found for $^{189–199}$Au. Furthermore, the calculated $E2$ transition strengths are compared to experimental values with fixed effective boson and fermion charges for all odd–even gold isotopes, emphasizing that the Spin(6) Bose–Fermi symmetry is valid for the gold isotopes.

Keywords: NUCLEAR REACTIONS ^{196}Pt$(p, 2n)$, $E = 14$ MeV; Measured E_γ, I_γ, $\gamma\gamma$-coin, $\gamma(\theta)$ using HORUS spectrometer. ^{195}Au deduced levels, J, π, branching and mixing ratios, B$(E2)$. Comparison with IBFM calculations

1. Introduction

In the last decades, the odd–even gold and even–even platinum isotopes were studied, confirming, that the Interacting Boson Model (IBM) and its extension, the Interacting Boson Fermion

* Corresponding author.

http://dx.doi.org/10.1016/j.nuclphysa.2014.02.002

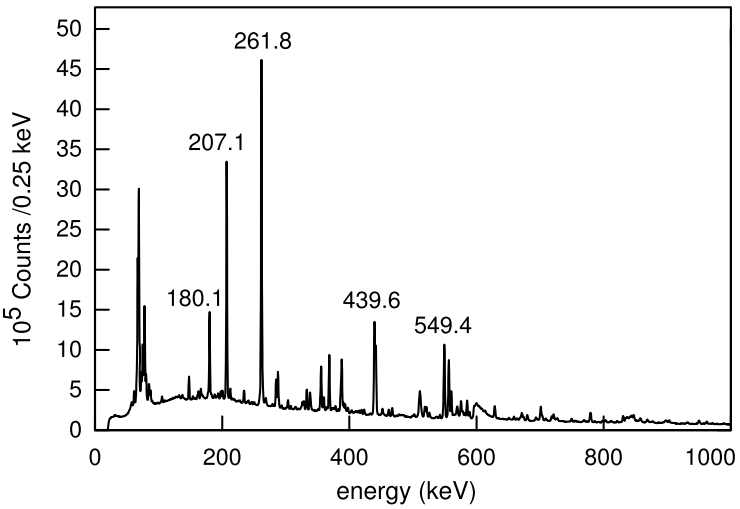

Fig. 1. Total projection of the $\gamma\gamma$ coincidence data. Major peaks from ^{195}Au are labeled with their energies.

Model (IBFM), in the O(6) limit are successful in describing the nuclear properties of excited states [1–8]. In this work we will concentrate on the Spin(6) Bose–Fermi symmetry of the IBFM for the description of odd–even gold isotopes. Hereby a proton fermion in the $\pi 2d_{3/2}$ orbital is coupled to a bosonic core in the O(6) limit. This model is employed to describe excited positive-parity states in the odd–even gold isotopes [2]. In this work we want to investigate whether the Bose–Fermi symmetry is able to give a conclusive description of $^{185-199}$Au. This is particularly interesting, considering, that the evolution of excited states is very smooth. However, essential information such as level spins, level energies of the second $7/2^+$ and first $11/2^+$ states, and multipole mixing ratios are missing for ^{195}Au. Situated in the middle of the isotopic chain, it is important to understand whether the excited states in ^{195}Au follows the smooth evolution. Therefore, an experiment measuring $e^-\gamma$ and $\gamma\gamma$ coincidences was performed after a ^{196}Pt$(p, 2n\gamma)$ and ^{194}Pt$(p, 2n\gamma)$ reaction using the Orange Spectrometer [10]. Some results obtained after the ^{194}Pt$(p, 2n\gamma)$ reaction were published in Ref. [11]. The experiment on ^{195}Au yielded new states at 703, 988 and 1178 keV which lead to inconsistencies with previous observations. To solve these contradictions, an experiment with the ^{196}Pt$(p, 2n\gamma)$ reaction using $\gamma\gamma$ coincidences and correlations was performed to observe transitions depopulating low-lying states with low spin.

In Section 2, we present the new results of the in-beam measurement in ^{195}Au. In Section 3, we investigate the evolution of the parameters within the Bose–Fermi symmetry throughout the odd–even gold isotopes.

2. Experimental results

A proton beam of 14 MeV delivered by the FN tandem accelerator at the Institute of Nuclear Physics, University of Cologne, was impinged on a 1.1 mg/cm^2 thick ^{196}Pt target enriched to 96.1%. Utilizing the ^{196}Pt$(p, 2n\gamma)$ reaction with only small grazing angular momentum transfer of about 3.5 $\hbar$ following estimates of the code *CASCADE* [12], mainly low-lying states with low spin were populated in ^{195}Au. The emitted γ rays were detected with the HORUS Spectrometer [13], which was equipped with ten high-purity germanium detectors. This setup allowed the analysis of $\gamma\gamma$ coincidences. The total projection of the $\gamma\gamma$ coincidence data up to 1000 keV is shown in Fig. 1. The strongest γ transitions are labeled and belong to ^{195}Au. Altogether, during five days of measurement, $1.2 \times 10^9 \gamma\gamma$ coincident events were collected. The data was sorted into 9 correlation group matrices, which account for detector pairs at angles $\Theta_{1,2}$ with

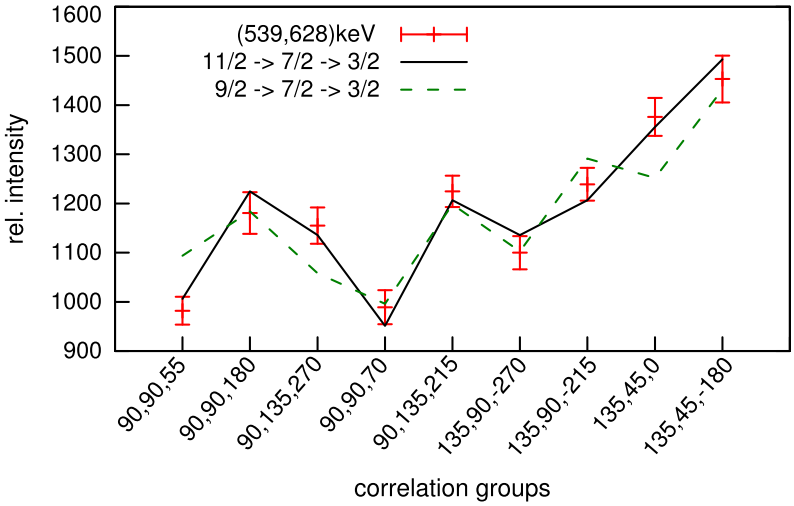

Fig. 2. (Color online.) Comparison of theoretical angular correlations with different spin hypotheses (black solid and green dashed line) with relative intensities obtained from 9 correlation groups with the specific angles Θ_1, Θ_2, ψ for the 549–628 keV $\gamma\gamma$ coincidence. This way the spin $J = 11/2$ of the new state at 1178 keV was determined.

respect to the beam axis and a relative angle ψ between the planes spanned by the detectors and the beam axis. This way, the experimental angular correlation of two coincident γ transitions is determined. By fitting spin hypothesis $J_1 \xrightarrow{E_A,\delta_A} J_2 \xrightarrow{E_B,\delta_B} J_3$, as described in Refs. [14,15], to the data, spins and multipole mixing ratios δ are obtained. The fit is performed with the computer code CORLEONE [16]. In Ref. [17] the same method using the HORUS spectrometer was applied to the neighboring ^{193}Au and the method is described in more detail in Refs. [13,18]. An exemplary pure ($E2$, $E2$) cascade depopulating a state at 1178.03 (5) keV is shown in Fig. 2. In the following, all the new low-lying states with energies up to the 1178 keV and results, which are in contradiction with previous publications, are discussed. Note, the first time the energy value is given together with errors, but for better understanding errors are omitted afterwards. In Table 1, all results obtained in this experiment are listed.

241.58 (7) keV, $3/2^+$. The angular correlation analyses of the $7/2 \xrightarrow{461} 3/2 \xrightarrow{180} 1/2$ and $7/2 \xrightarrow{721} 3/2 \xrightarrow{180} 1/2$ cascades consistently yield two possible $E2/M1$ mixing ratios, $\delta_{180} = +0.06\,(10)$ and $\delta_{180} = -1.86\,(71)$, for the 180.11 (7) keV transition. Since the smaller $E2/M1$ mixing ratio agrees with the $\delta_{180} \approx 0.16$ measured in Refs. [10,19] using conversion electrons, $\delta_{180} = +0.06\,(10)$ is adopted and given in Table 1.

703.48 (6) keV, $7/2^+$. This state was first proposed in Ref. [10] due to inconsistencies in the $e^-\gamma$ and $\gamma\gamma$ coincidence spectra. Our experiment revealed, based on coincidences with the 284.71 (9), 474.45 (10), 509.82 (7) and 613.50 (7) keV transitions feeding this state, that the 441.70 (6) keV transition depopulates the new state at 703 keV and supports the assignment given in Ref. [10]. Apparently, since the 703 keV state was previously unknown, the 441 keV decay together with the coincident 693 keV transition were misplaced and led to assuming a state at 955.08 (15) keV. Note, using the coincidences with the 284, 474, 509 and 613 keV transitions, other transitions at 154.05 (12), 263.75 (11), 461.90 (9) and 703.50 (9) keV are observed depopulating the new 703 keV level with consistent branching ratios, thus, supporting the new assignment.

830.52 (5) keV, $5/2, 7/2^+$. The 830.55 (8) keV transition to the ground state together with the coincident transitions populating this state with 132.38 (13), 288.84 (10), 382.6 (14), 555.45 (12), and 802.67 (13) keV allows the identification of this new state. Unfortunately this state

Table 1
Results of this work on ^{195}Au compared to the literature values from Nuclear Data Sheets (NDS) [23]. States discussed in Section 2 are labeled with $^{\#}$. Newly observed states are labeled with * and newly observed transitions with †. Furthermore, γ intensities I_γ of transitions that are listed in NDS but are not observed due to the sensitivity limit of the detector system or background are labeled with $-$. If the spin or energy of a state is adopted from NDS it is labeled with **. If a spin assignment of a state due to angular correlation analysis is not unique, those spins are labeled with ‡‡. If an angular correlation analysis is not feasible but selection rules suggest the multipole characteristic of the γ transition, the multipolarity is given in parentheses.

E_{level} (keV)	J^π_{initial}	E_γ (keV)	I_γ [23]	$I_{\gamma,\text{exp}}$	δ [23]	δ_{exp}	E_{final} (keV)	J^π_{final}
0.0	$3/2^+$							
61.46 (5)	$1/2^{+**}$	61.46 (5)	100	100	0.45 (1)		0	$3/2^+$
241.58 (7)$^{\#}$	$3/2^+$	180.11 (7)	100 (5)	100	≈0.16	+0.06 (10)	61.46 (5)	$1/2^+$
		241.60 (12)	3.6 (6)	3.8 (10)	≈2.2		0	$3/2^+$
261.78 (5)	$5/2^+$	200.37 (12)	2.6 (3)	2.1 (5)	$E2$	+0.01 (6)	61.46 (5)	$1/2^+$
		261.77 (5)	100 (5)	100	0.51 (1)	−0.55 (14)	0	$3/2^+$
318.58 (4)**	$11/2^{-**}$	318.60 (10)**	100 (11)	–	$M4$		0	$3/2^+$
		56.80 (3)**	72 (3)	–	$E3$		261.77 (5)	$5/2^+$
439.58 (5)	$5/2^+$	198.00 (11)†		6.2 (6)		−0.29 (26)	241.58 (7)	$3/2^+$
		378.15 (14)†		6.0 (7)		($E2$)	61.46 (5)	$1/2^+$
		439.58 (6)	100	100	$M1$	−0.04 (4)	0	$3/2^+$
525.69 (7)	$7/2^-$	207.11 (6)	100	100	$E2$	+0.01 (10)	318.58 (4)	$11/2^-$
549.46 (5)	$7/2^+$	287.67 (6)	21 (4)	21.7 (14)		+0.04 (2)	261.78 (5)	$5/2^+$
		307.87 (13)†		1.6 (4)		$(+3.94^{+18.12}_{-1.88})$	241.58 (7)	$3/2^+$
		549.47 (6)	100 (10)	100	($E2$)	+0.05 (10)	0	$3/2^+$
703.48 (6)*	$7/2^+$	154.05 (12)†		3.3 (4)		−0.13 (21)	549.47 (6)	$7/2^+$
		263.75 (11)†		7.7 (6)		+0.15 (6)	439.58 (5)	$5/2^+$
		441.70 (6)†		100		−0.20 (2)	261.78 (5)	$5/2^+$
		461.90 (9)†		10.4 (7)		+0.00 (12)	241.58 (7)	$3/2^+$
		703.50 (9)†		14.9 (11)		−0.17 (18)	0	$3/2^+$
706.52 (7)	$15/2^-$	387.94 (6)	100	100	$E2$	−0.05 (6)	318.58 (4)**	$11/2^-$
818.18 (7)	$9/2^+$	268.71 (12)†		5.4 (5)		−0.34 (12)	549.46 (5)	$7/2^+$
		556.41 (6)	100	100	($E2$)	+0.01 (2)	261.78 (5)	$5/2^+$
830.52 (5)$^{*\#}$	$5, 7/2^{+*\ddagger\ddagger}$	390.87 (12)†		38.0 (38)			439.58 (5)	$5/2^+$
		588.94 (6)†		45.0 (50)			241.58 (7)	$3/2^+$
		830.55 (8)†		100			0	$3/2^+$
841.31 (9)	$3/2^+$	401.74**	0.07 (2)	–			439.58 (5)	$5/2^+$
		599.75 (8)	26.2 (9)	20 (8)	0.55 (2)	+0.54 (23)	241.58 (7)	$3/2^+$
		779.79 (21)	100	100			61.46 (5)	$1/2^+$
		841.27**	4.0 (9)	–	$M1$, $E2$		0	$3/2^+$
878.90 (7)	$13/2^{-**}$	172.35 (15)	0.76 (11)	1.0 (3)	$M1$	($M1$)	706.52 (7)	$15/2^-$
		560.32 (6)	100	100	$M1$	+0.23 (4)	318.58 (4)	$11/2^-$
894.14 (6)	$9/2^-$	368.43 (6)	100 (4)	100	$M1$	+0.18 (6)	525.69 (7)	$7/2^-$
		575.58 (7)	65 (7)	57.0 (49)	0.65 (30)	−0.60 (40)	318.58 (4)	$11/2^-$

(*continued on next page*)

Table 1 (*continued*)

E_{level} (keV)	J^{π}_{initial}	E_{γ} (keV)	I_{γ} [23]	$I_{\gamma,\text{exp}}$	δ [23]	δ_{exp}	E_{final} (keV)	J^{π}_{final}
962.80 (5)*#	$7/2^{+}$	132.38 (13)†		2.5 (8)			830.52 (5)	$5, 7/2^{+}$
		413.26 (7)†		10.3 (13)		(M1)	549.46 (5)	$7/2^{+}$
		701.04 (6)†		100		+2.00 (10)	261.78 (5)	$5/2^{+}$
		721.23 (6)†		56.2 (49)		−0.06 (7)	241.58 (7)	$3/2^{+}$
988.34 (12)*#	$9/2^{+}$	284.71 (9)†		39.1 (29)		−0.15 (8)	703.48 (6)	$7/2^{+}$
		548.86 (7)†		100		+0.01 (5)	439.58 (5)	$5/2^{+}$
1068.19 (5)	$9/2^{-}$	105.47 (12)		16.2 (12)			962.80 (5)	$7/2^{+}$
		250.00 (10)		9.7 (10)			818.18 (7)	$9/2^{+}$
		364.62 (9)		11.6 (14)			703.48 (6)	$7/2^{+}$
		518.66 (6)	100 (21)	100		0.01 (4)	549.46 (5)	$7/2^{+}$
		542.51 (7)	55 (13)	42.8 (32)		0.25 (10)	525.69 (7)	$7/2^{-}$
		749.65 (7)	100 (16)	67.5 (49)	$M1$	−0.09 (8)	318.58 (4)	$11/2^{-}$
1083.05 (8)	$3/2^{+}$	821.27 (6)	100 (9)		$M1\,(+E2)$	0.19 (3)	261.78 (5)	$5/2^{+}$
		1021.8 (2)**	64 (7)	–	$(E2)$		61.46 (5)	$1/2^{+}$
		1082.90 (2)**	24 (3)	–	$M1$		0	$3/2^{+}$
1110.97 (9)$^{-}$		585.18 (5)	100 (4)		$E2$		525.69 (7)	$7/2^{-}$
		671.13 (25)**	1.2 (14)	–			439.58 (5)	$5/2^{+}$
		868.9 (3)**	0.17 (7)	–			241.58 (7)	$3/2^{+}$
		1049.27 (25)**	10 (3)	–			61.46 (5)	$1/2^{+}$
1119.34 (4)*#	$7, 9/2^{+}$‡‡	288.84 (10)†		52.8 (48)			830.52 (5)	$5, 7/2^{+}$
		415.85 (7)†		31.4 (43)			703.48 (6)	$7/2^{+}$
		569.87 (7)†		99.0 (81)			549.46 (5)	$7/2^{+}$
		679.77 (6)†		100			439.58 (5)	$5/2^{+}$
1178.03 (5)*#	$11/2^{+}$#	359.85 (6)†		48.9 (41)		−0.09 (3)	818.18 (7)	$9/2^{+}$
		474.45 (10)†		10.7 (30)			703.48 (6)	$7/2^{+}$
		628.61 (6)†		100		+0.05 (6)	549.46 (5)	$7/2^{+}$
1213.24 (8)*	$5/2^{+}$	382.6 (14)†		15.3 (20)			830.52 (5)	$5, 7/2^{+}$
		509.82 (7)†		100		−0.038 (14)	703.48 (6)	$7/2^{+}$
		663.79 (10)†		38.4 (25)		$+3.92^{+5.05}_{-1.48}$	549.46 (5)	$7/2^{+}$
		951.54 (9)†		41.2 (25)		+0.02 (8)	261.78 (5)	$5/2^{+}$
		971.70 (8)†		36.5 (22)		+0.50 (26)	241.58 (7)	$3/2^{+}$
1251.12 (5)	$3, 5/2$‡‡	811.46 (8)	68 (23)	100			439.58 (5)	$5/2^{+}$
		989.36 (7)	40 (15)	77.8 (47)			261.78 (5)	$5/2^{+}$
		1009.58 (8)	100 (20)	62.7 (41)			241.58 (7)	$3/2^{+}$
		1189.5 (2)**	76 (15)	–			61.46 (5)	$1/2^{+}$
		1251.14 (13)**	53 (10)	–			0	$3/2^{+}$
1280.57 (5)	$11/2^{-}$	386.41 (7)	100 (10)	100	$M1$	+0.20 (5)	894.14 (6)	$9/2^{-}$
		401.69 (16)	5.4 (13)	6.1 (7)	–		878.90 (7)	$13/2^{-}$
		754.89 (7)	20 (2)	19.9 (18)	$E2$	+0.03 (15)	525.69 (7)	$7/2^{-}$
		962.00 (7)	77 (7)	77.4 (63)	$M1$		318.58 (4)	$11/2^{-}$
1304.74 (8)*	$(3, 5, 7/2^{-})$	193.81 (8)†		13.2 (12)			1110.97 (9)	$3/2^{-}$
		779.03 (7)†		100			525.69 (7)	$7/2^{-}$
1317.01 (5)*	$9/2^{+}$	328.67 (10)†		16.6 (59)			988.34 (12)	$9/2^{+}$
		354.23 (7)†		100		−0.59 (12)	962.80 (5)	$7/2^{+}$

Table 1 (*continued*)

E_{level} (keV)	J^{π}_{initial}	E_{γ} (keV)	I_{γ} [23]	$I_{\gamma,\text{exp}}$	δ [23]	δ_{exp}	E_{final} (keV)	J^{π}_{final}
		498.79 (7)†		32.8 (60)		$-2.04^{+0.71}_{-1.61}$	818.18 (7)	$9/2^{+}$
		613.50 (7)†		73.0 (77)		$+4.11^{+1.94}_{-1.03}$	703.48 (6)	$7/2^{+}$
		767.62 (13)†		38.9 (68)			549.46 (5)	$7/2^{+}$
1346.22 (6)	$11/2^{-}$	452.06 (6)	72 (5)	75.2 (43)	$M1$	+0.16 (6)	894.14 (6)	$9/2^{-}$
		467.34 (6)	100 (6)	100	$M1$	+0.04 (5)	878.90 (7)	$13/2^{-}$
		1027.45 (11)**	40 (5)	–	$M1$		318.58 (4)	$11/2^{-}$
1365.52 (9)	$17/2^{-}$	659.00 (6)	100	100		+0.29 (3)	706.52 (7)	$15/2^{-}$
1386.01 (5)*	$9/2^{+}$	397.75 (7)†		100		+0.43 (18)	988.34 (12)	$9/2^{+}$
		423.19 (7)†		87.5 (53)		+0.17 (5)	962.80 (5)	$7/2^{+}$
		555.45 (12)†		39.2 (49)			830.52 (5)	$5, 7/2^{+}$
		682.63 (13)†		15.9 (12)			703.48 (6)	$7/2^{+}$
		836.56 (9)†		89.9 (52)		+0.58(17)	549.46 (5)	$7/2^{+}$
1396.90 (5)$^{\#}$	$11/2^{+}$	578.67 (6)	100 (17)	79.5 (17)	($M1$)	−0.19 (4)	818.18 (7)	$9/2^{+}$
		693.40 (6)		100	($E2$)	−0.02 (7)	703.48 (6)	$7/2^{+}$
		847.57 (10)	69 (17)	33.6 (12)			549.46 (5)	$7/2^{+}$
1404.65 (7)	$15/2^{-}$	525.68 (7)	100 (6)	100	$M1$	+0.22 (4)	878.90 (7)	$13/2^{-}$
		698.19 (7)	13.1 (13)	12.4 (12)	$M1$	+0.09 (46)	706.52 (7)	$15/2^{-}$
		1086.2 (20)**	9.7 (14)	–			318.58 (4)	$11/2^{-}$
1406.09 (8)	$11/2^{-}$	337.90 (6)	100	100		−1.02(15)	1068.19 (5)	$9/2^{-}$
1424.73 (9)	$19/2^{-}$	718.21 (5)	100	100	$E2$	−0.01 (5)	706.52 (7)	$15/2^{-}$
1475.56 (6)*		581.42 (6)†		100			894.14 (6)	$9/2^{-}$
		949.86 (6)†		81.3 (84)			525.69 (7)	$7/2^{-}$
1487.25 (9)	$9, 11/2^{-}$**	419.06 (7)	100	100	≈2.4		1068.19 (5)	$9/2^{-}$
1489.45 (10)	$13/2^{+}$	671.27 (7)	100	100		−0.01 (4)	818.18 (7)	$9/2^{+}$
1527.10 (8)*	$7/2^{+}$	708.92 (7)		100		+0.24 (9)	818.18 (7)	$9/2^{+}$
		977.63 (11)		26.3 (29)		$-0.19^{+0.51}_{-0.61}$	549.46 (5)	$7/2^{+}$
1559.74 (6)	$13/2^{-}$**	279.11 (10)	22 (6)	61.6 (62)	$M1$		1280.57 (5)	$11/2^{-}$
		665.42 (12)**	8.7 (8)	–			894.14 (6)	$9/2^{-}$
		680.88 (9)	35 (4)	69.3 (68)	$M1$		878.90 (7)	$13/2^{-}$
		853.23 (9)	42 (5)	100	$M1$		706.52 (7)	$15/2^{-}$
		1241.17 (10)**	100 (1)	–	$M1$		318.58 (4)	$11/2^{-}$
1567.89 (15)*		263.24 (8)		45.6 (28)			1304.74 (8)	$(3, 5, 7/2^{-})$
		673.94 (7)		100			894.14 (6)	$9/2^{-}$
		1041.9 (7)		53.6 (32)			525.69 (7)	$7/2^{-}$
1605.55 (27)	$(11, 13)/2^{-}$	324.50 (7)	16 (6)	32.9 (19)			1280.57 (5)	$11/2^{-}$
		711.01 (13)†		10.0 (12)			894.14 (6)	$9/2^{-}$
		727.37 (7)	100 (10)	61.6 (33)	$M1$		878.90 (7)	$13/2^{-}$
		899.01 (1)	82 (15)	100	($E2$)		706.52 (7)	$15/2^{-}$
		1286.4 (4)**	13 (3)	–			318.58 (4)	$11/2^{-}$
1633.01 (10)*		513.69 (9)†		100			1119.34 (4)	$7, 9/2^{+}$
		802.67 (13)†		24.9 (27)			830.52 (5)	$5, 7/2^{+}$
		814.62 (11)†		49.5 (34)			818.18 (7)	$9/2^{+}$

(*continued on next page*)

Table 1 (*continued*)

E_{level} (keV)	J^{π}_{initial}	E_{γ} (keV)	I_{γ} [23]	$I_{\gamma,\text{exp}}$	δ [23]	δ_{exp}	E_{final} (keV)	J^{π}_{final}
1656.42 (5)*	$9, 11/2^{+\ddagger\ddagger}$	270.35 (8)†		28.7 (45)			1386.01 (5)	$9/2^{+}$
		478.38 (9)†		74.0 (47)			1178.03 (5)	$11/2^{+}$
		668.25 (5)†		100			988.34 (12)	$9/2^{+}$
		838.23 (9)†		57.2 (44)			818.18 (7)	$9/2^{+}$
1691.84 (9)*	$(9, 11/2^{-})$	411.11 (8)†		24.9 (23)			1280.57 (5)	$11/2^{-}$
		797.86 (12)†		11.3 (11)			894.14 (6)	$9/2^{-}$
		812.78 (12)†		12.4 (11)			878.90 (7)	$13/2^{-}$
		1166.3 (6)†		100			525.69 (7)	$7/2^{-}$
1711.8 (4)*		315.05 (6)†		62.3 (52)			1396.90 (5)	$11/2^{+}$
		723.72 (4)†		100			988.34 (12)	$9/2^{+}$
1779.3 (5)*		372.94 (8)†		100			1406.09 (7)	$11/2^{-}$

is not populated strongly enough in order to distinguish between the possible spins $5/2$, $7/2$ in the angular correlation analysis.

946.83 (16) keV. This state with the depopulating transition of 628.30 (20) keV reported by Refs. [20,21] cannot be confirmed by our data. Instead the 628 keV transition is assigned to a new state at 1178 keV (cf. discussion about the state at 1178 keV).

955.08 (15) keV, $(9/2^{+})$. This state with the depopulating transition of 693.17 (25) keV reported by Refs. [20–22] cannot be confirmed by our data. Instead the analysis of $\gamma\gamma$ coincidences reveals that the 693 keV transition is feeding a state at 703.48 (6) keV reported in Ref. [10], thus, this transition is assigned to a state at 1396 keV (cf. discussion about the state at 1396 keV). Due to the large error, the observation of a state at 960 (10) keV after a (p, t) reaction [22] could also corresponds to a new state at 962.80 (5) keV observed in our experiment.

962.80 (5) keV, $7/2^{+}$. This state could be identified with the 105.47 (12), 354.23 (7) and 423.19 keV transitions feeding this state. The feeding transitions reveal consistent branching ratios for the transitions depopulating the 962 keV state.

988.34 (5) keV, $9/2^{+}$. This state was already proposed in Ref. [10] and the coincidence spectra of the 328.67 (10), 397.75 (7) and 668.25 (5) keV transitions confirm this new state.

1119.34 (4) keV, $7/2, 9/2^{+}$. The $\gamma\gamma$ coincidences show, that a 513.69 (9) keV transition feeds a state at 1119 keV and that this state is depopulated by 288.84 (10), 415.85 (7), 569.87 (7) and 679.77 (6) keV transitions.

1178.03 (5) keV, $11/2^{+}$. A 478.38 (9) keV transition feeding the 1178 keV state and in coincidence with the depopulating transitions at 359.58 (6), 474.45 (10) and 693.17 (25) keV confirms the existence of this new state. Fig. 2 shows a $\gamma\gamma$ angular correlation analysis for the spin hypotheses $11/2 \xrightarrow{614} 7/2 \xrightarrow{549} 3/2_{gs}$ (black solid line) and $9/2 \xrightarrow{614} 7/2 \xrightarrow{549} 3/2_{gs}$ (green dashed line). The spin hypothesis $11/2 \xrightarrow{614} 7/2 \xrightarrow{549} 3/2_{gs}$ fits the data best. The angular correlation analysis of the (359,556 keV) cascade also favors a spin assignment of $11/2$ to the 1178 keV state. Thus, the spin for the newly observed state at 1178 keV was determined to be $11/2$. The multipole mixing ratio of the transition to the $9/2^{+}$ state favors the assignment of positive parity to the 1178 keV state.

1396.90 (5) keV, $11/2^{+}$. A transition at 441.50 (20) keV was assigned to this state in Ref. [20]. This transition is now assigned to the new state at 703 keV (see the discussion about the

703 keV state). The new assignment of transitions is supported by a new 315.05 (6) keV transition feeding this state and by measurements using $e^-\gamma$ coincidences in Ref. [10].

3. IBFM calculation in the framework of the Spin(6) Bose–Fermi symmetry

In various publications [7,9,24–26], the nuclear properties of ^{195}Au were described using the Interacting Boson Fermion Model as well as the Interacting Boson Fermion Model-2, establishing that both the positive-parity and negative-parity states can be understood in the framework of these models. In the current work, we focus on the structure of the positive-parity states in ^{195}Au and in the neighboring odd–even gold isotopes. For this, we use the Spin(6) Bose–Fermi symmetry and couple a proton in the $\pi 2d_{3/2}$ orbital to a bosonic core described by the IBM O(6) limit [4,27]. The corresponding group chain of this Hamiltonian can be written as:

$$\begin{array}{ccccccccc} \mathrm{U}^B(6) & \otimes & \mathrm{U}^F(4) & \supset & \mathrm{SO}^B(6) & \otimes & \mathrm{SU}^F(4) \supset \mathrm{Spin}^{BF}(6) & \supset \mathrm{Spin}^{BF}(5) & \supset \mathrm{Spin}^{BF}(3) \\ [N_B] & & \left[1^{N_F}\right] & & \langle\sigma\rangle & & \langle\alpha_1,\alpha_2,\alpha_3\rangle\ \langle\sigma_1,\sigma_2,\sigma_3\rangle & (\tau_1,\tau_2) & J \end{array} \tag{1}$$

with $N_F = 1$ in the case of the odd-A nucleus. In the gold isotopes N_B corresponds to the number of boson holes with respect to the neutron shell closure at $N = 126$ and the proton shell closure at $Z = 82$. Other quantum numbers ($\langle\sigma\rangle$, $\langle\alpha_1,\alpha_2,\alpha_3\rangle$ $\langle\sigma_1,\sigma_2,\sigma_3\rangle$, (τ_1,τ_2), J) of the nested algebras are determined by reduction rules (see Ref. [2]). The Hamiltonian written in form of a linear combination of Casimir operators corresponding to the group chain, neglecting constant terms that only contribute to the binding energy, is:

$$\begin{aligned} H = {} & D\cdot C_2\big[\mathrm{SO}^B(6)\big] + A\cdot C_2\big[\mathrm{Spin}^{BF}(6)\big] \\ & + B\cdot C_2\big[\mathrm{Spin}^{BF}(5)\big] + C\cdot C_2\big[\mathrm{Spin}^{BF}(3)\big]. \end{aligned} \tag{2}$$

Where $C_2[X]$ is the second order Casimir operator of the given algebra X. The corresponding energy eigenfunction of the Hamiltonian can be derived from the eigenfunction of the Casimir operators of the subgroups and yields [27]:

$$\begin{aligned} E = {} & D\sigma(\sigma+4) + A\big(\sigma_1(\sigma_1+4) + \sigma_2(\sigma_2+2) + \sigma_3^2\big) \\ & + B\big(\tau_1(\tau_1+3) + \tau_2(\tau_2+1)\big) + C\big(J(J+1)\big). \end{aligned} \tag{3}$$

Calculations using the Bose–Fermi symmetry were already successfully employed for the following gold isotopes: ^{191}Au [28], ^{193}Au [17,29], ^{195}Au [5–7], ^{197}Au [2,3,30–32] and ^{199}Au [33]. In these references the Bose–Fermi symmetry was applied to individual nuclei or specific odd–even and odd–odd neighboring gold isotopes. Here we present a systematic investigation for a larger number of odd–even gold isotopes within the framework of the Spin(6) Bose–Fermi symmetry according to Eqs. (1)–(3).

Recently, an Interacting Boson Fermion Model calculation using all proton orbitals ($\pi 1g_{7/2}$, $\pi 2d_{5/2}$, $\pi 1h_{9/2}$, $\pi 2d_{3/2}$, $\pi 3s_{1/2}$) between the $Z = 50$ and $Z = 82$ shell closures for ^{193}Au [17] was performed, showing that the main contribution to the wave functions of the low-lying positive-parity states with $(\tau_1,\tau_2) = (1/2,1/2) - (5/2,1/2)$ originates from the $\pi 2d_{3/2}$ orbital. To simplify matters only τ_1 is mentioned in the following sections, as τ_2 is always equal to $1/2$. However, according to the full IBFM calculation, the $\pi 3s_{1/2}$ contribution to the wave function increases considerably for the third $5/2^+$ states, thus this state cannot be described as a member of the $\tau_1 = 7/2$ multiplet. Another difficulty is the determination of positive-parity states associated to other multiplets than the $\langle\sigma\rangle = \langle N_B\rangle$ and $\langle\sigma_1,\sigma_2,\sigma_3\rangle = \langle N_B + 1/2, 1/2, 1/2\rangle$

multiplet. Furthermore, only a few low-spin states far off pseudo-yeast especially for the more exotic gold isotopes are known. Thus, in this work we investigate only states associated with the $\tau_1 = 1/2, 3/2, 5/2$ multiplets and with spins up to $11/2^+$ in each of the odd–even gold isotopes. Hence, only the parameters B and C in the eigenfunction (3) are relevant for a fit of the excitation energies.

Note, the level scheme of the Spin(6) Bose–Fermi symmetry looks similar to the Spin(5) Bose–Fermi symmetry, where a nucleon in a $j = 3/2$ orbital is coupled to a bosonic core in the U(5) limit [2], especially when solely the τ_1, τ_2 and J quantum numbers are considered. But two crucial differences allows the distinction between these two Bose–Fermi symmetries in the gold isotopes. Firstly, in the Spin(5) Bose–Fermi symmetry the second $(\tau_1, \tau_2) = (1/2, 1/2)$ and $J = 3/2$ state is associated with the same $n_d = 1$ multiplet (the other states are $J = 1/2, 5/2, 7/2$). Together with the $J = 3/2$ states associated with the $n_d = 0$ and $n_d = 2$ multiplets, more $3/2$ states are predicted than observed in the gold isotopes between 0–800 keV. In the Spin(6) Bose–Fermi symmetry this problem is avoided, since the second $(\tau_1, \tau_2) = (1/2, 1/2)$, $J = 3/2$ state belongs to the next $\langle \sigma_1, \sigma_2, \sigma_3 \rangle = \langle N_B - 1/2, 1/2, 1/2 \rangle$ multiplet and thus can be shifted to higher energies without affecting other low-lying states. Secondly, in the Spin(5) Bose–Fermi symmetry the B($E2$) strength for transitions connecting the lowest $J = 1/2 - 7/2$ states to the ground state depend purely on the effective boson charge α_2 and the number of bosons N_B. In the Spin(6) Bose–Fermi symmetry, the fermion charge f_2 and the τ_1 quantum number influence the B($E2$) strength (see Eq. (4)). Furthermore, for transition between higher excited states in the Spin(5) Bose–Fermi symmetry, β_2, another effective boson charge, is crucial for the B($E2$) value. Due to algebraic considerations the effective boson charge β_2 is omitted in the Spin(5) Bose–Fermi symmetry. Hence, albeit only the highest $\langle \sigma_1 \rangle$ multiplet of the Spin(6) Bose–Fermi symmetry is observed, a differentiation to the Spin(5) Bose–Fermi symmetry is possible.

The knowledge of the levels in the gold isotopes is primarily based on the compilation of data in the Nuclear Data Sheets (NDS) [23,34–40]. For ^{193}Au, additional information was taken from Ref. [17] and for ^{195}Au the results from this work were adopted. ^{183}Au and ^{201}Au are not considered due to the scarce knowledge of states which can be associated to the $\tau_1 = 5/2$ multiplet.

In Fig. 3(a), levels associated with the $\tau_1 = 1/2, 3/2, 5/2$ multiplets in $^{185-199}$Au are shown. If the spin of a state is not unambiguously known, that state is given in parenthesis. States in ^{195}Au are labeled in blue in case the state has been firstly observed in this experiment and labeled in red, if the spin is determined for the first time. Note, the results obtained from this experiment are important for the interpretation of the evolution of levels. The new second $7/2^+$ and first $11/2^+$ fits in with the overall smooth evolution of level energies. This indicates, that the difference in single-particle energies between the $\pi 2d_{3/2}$ and $\pi 3s_{1/2}$ orbitals and the population of the $d_{3/2}$ and $s_{1/2}$ orbitals are constant for different odd–even gold isotopes. Calculations based on the Nilsson Model show consistent results, predicting a constant difference between the single-particle energies for the $\pi 2d_{3/2}$ and $\pi 3s_{1/2}$ orbitals despite increasing β-deformation [41]. With regard to the evolution of the states shown in Fig. 3(a), just three changes of the ordering of levels are observed, the most significant one is the switch of the ground state from $1/2^+$ to $3/2^+$ from ^{189}Au to ^{191}Au.

In order to investigate the Bose–Fermi symmetry, a least-square fit was preformed for each odd–even gold isotope separately and to all those levels given in Fig. 3(a). For the fit, the computer code *ArbModel* [42] was used and the quantum numbers were derived from Eq. (3).

The parameters of the fits are listed in Table 2 and the theoretical levels are shown in Fig. 3(b). Note, the parameters are similar to the parameters derived from calculations in other Refs. [3,17].

Table 2
The parameters derived from a least-square fit using Eq. (3) to the energy of the states of the gold nuclei. The corresponding root mean square error (RMS) is given in MeV.

Gold isotope	C (MeV)	B (MeV)	RMS (MeV)
185	0.0210	0.0109	0.102
187	0.0268	0.0148	0.065
189	0.0296	0.0141	0.057
191	0.0291	0.0180	0.049
193	0.0289	0.0213	0.050
195	0.0284	0.0240	0.051
197	0.0284	0.0274	0.049
199	0.0298	0.0302	0.025

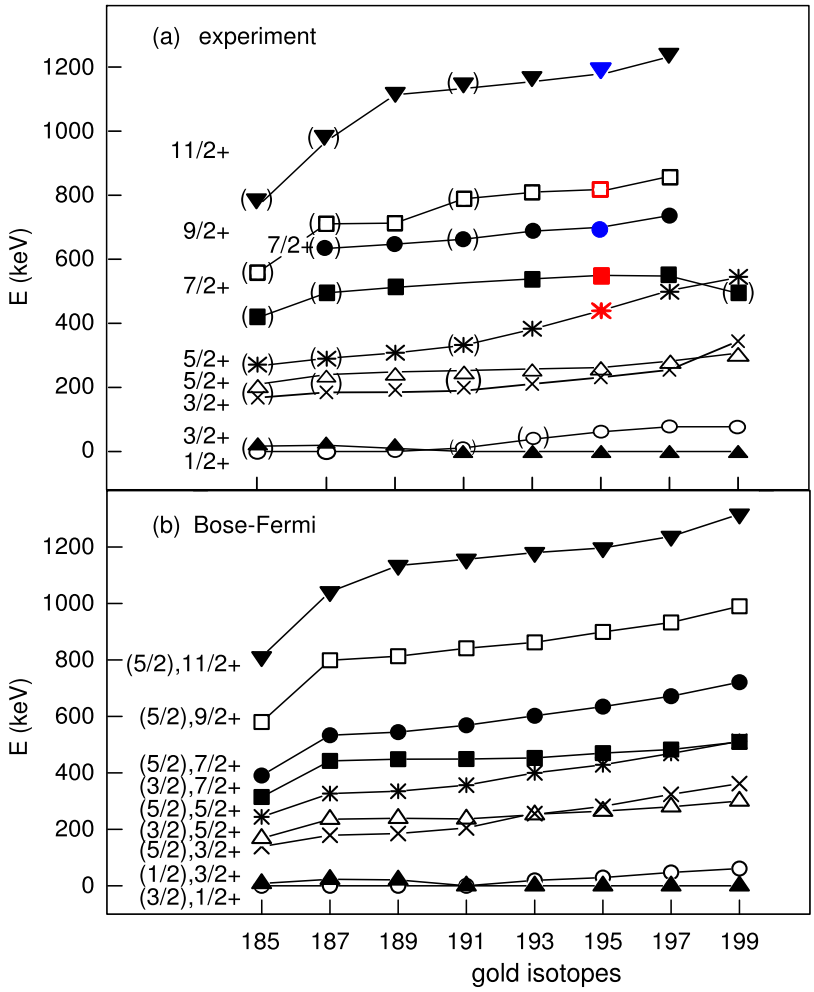

Fig. 3. (Color online.) The evolution of low-lying states in the odd–even $^{185-199}$Au isotopes is shown top figure (a). If the spin is not unambiguously known, the states are labeled with parentheses. States in ^{195}Au are colored in red, in case the spin could be exactly determined and blue, in case that state is observed of the first time. $*$ denotes, that in ^{185}Au the ground state is $5/2^-$, thus, the excitation energies of positive-parity states are normalized with respect to the energy of the first excited $1/2^+$ state. The bottom figure (b) shows the evolution of the states derived from an IBFM calculation employing the Bose–Fermi symmetry. The (τ_1) and J quantum numbers are given next to the states.

On the left of the figure the quantum number (τ_1) and the spin J of each state is given. As discussed above, all states shown in the figure have the same $\langle\sigma\rangle = \langle N_B\rangle$ and $\langle\sigma_1, \sigma_2, \sigma_3\rangle$ quantum numbers. Comparison between Fig. 3(a) and 3(b) reveals that the observed levels are in a good

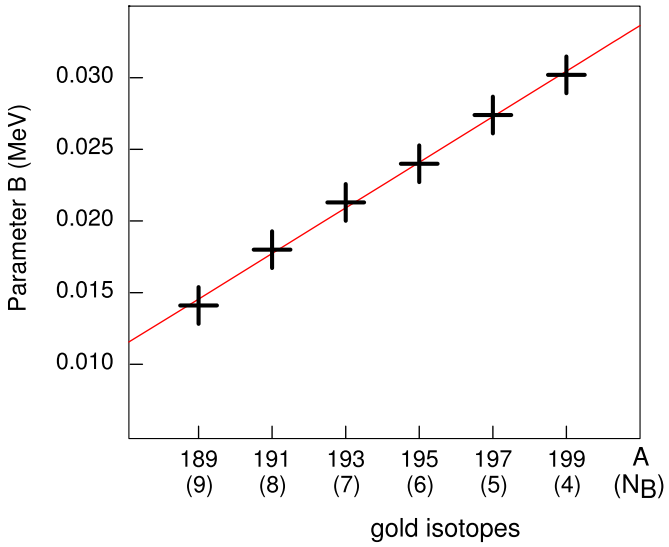

Fig. 4. (Color online.) A linear function $f(N_B) = a_\tau - b_\tau \times N_B$ is fitted to the strength of the τ splitting (parameter B) in $^{189–199}$Au with the boson holes $N_B = 4$–9. The derived parameters are $a_\tau = 0.0432$ MeV and $b_\tau = 0.0032$ MeV.

agreement with the calculated states, also indicated by root mean square error (RMS) given in Table 2. In fact the change of ordering of levels observed experimentally can be reproduced in the calculations. Especially the switch of the ground state from spin $J^\pi = 1/2^+$ in ^{187}Au to $J^\pi = 3/2^+$ in ^{191}Au is described by the model. Overall, the evolution of levels along the gold isotopes is rather smooth. However, in ^{185}Au the energies of especially the $9/2^+$ and $11/2^+$ states are drastically reduced, which can be attributed to the influence of the bosonic core. In ^{186}Hg, the bosonic core for ^{185}Au, shape coexistence of $0p$–$2h$ configuration and a configuration induced by two-particle excitations across the $Z = 82$ shell gap plays a major role [43,44]. For ^{187}Au the influence of shape coexistence diminishes considering that the intruder configuration in ^{188}Hg is shifted up sharply to higher energies. Of greater significance to the low-lying positive-parity states could be the proximity of ^{187}Au to ^{186}Pt. Similar to the situation in the mercury isotopes, in the neutron-deficient even–even $^{178–188}$Pt coexisting strongly deformed prolate and weakly deformed oblate configurations are observed [45–47]. In fact, the ground state in $^{178–186}$Pt nuclei are strongly deformed, while in ^{188}Pt the first state associated with a prolate configuration is observed at 900 keV and the ground state exhibits oblate shape. Since the influence of the strongly deformed configuration to the low-lying states in ^{188}Pt should be greatly reduced, it seems appropriate to use the Bose–Fermi symmetry to describe ^{189}Au.

The parameters B and C derived for τ and J splitting (see Table 2), respectively, are shown in Figs. 4 and 5. The x-axis denotes the number of boson holes needed to describe the nucleus. For the parameters obtained for $^{189–199}$Au, a graduate change is apparent and linear functions $f(N_B) = a_{\tau,J} - b_{\tau,J} \times N_B$ were fitted to these values. ^{185}Au and ^{187}Au are omitted from the fits as the model space encompassing the Bose–Fermi symmetry cannot describe shape coexistence. The solid lines represents the linear functions and show excellent agreement with the strength of the τ and J splitting, respectively. While the slope of the linear fit to parameter C is approximately constant ($b_J = -0.0001$ MeV and $a_J = 0.0283$ MeV), parameter B decreases with increasing number of bosons N_B ($b_\tau = 0.0032$ MeV and $a_\tau = 0.0432$ MeV). In fact, the change of τ splitting, induced by the Spin$^{BF}(5)$ algebra, in the IBFM reflects the collectivity. Phenomenologically, this can be understood using the bosonic core of the odd–even gold isotopes. It is well known, that generally in even–even nuclei the energy of the first 2^+ decreases linearly as collectivity increases along an isotopic chain and as the nuclei approach mid-shell.

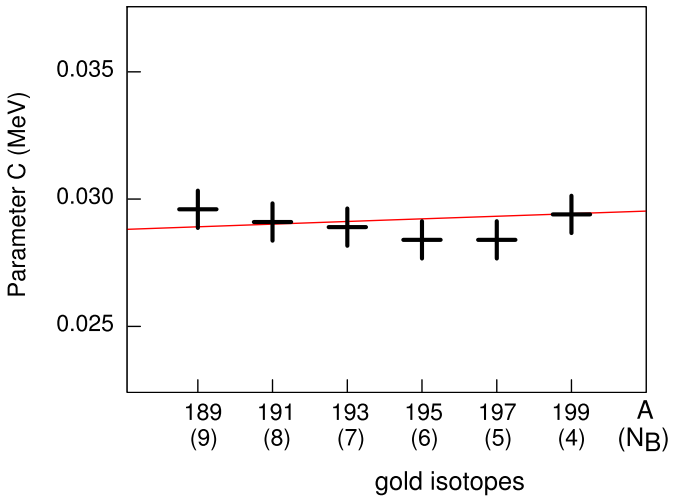

Fig. 5. (Color online.) A linear function $f(N_B) = a_J - b_J \times N_B$ is fitted to the strength of the J splitting (parameter C) in $^{189-199}$Au with the boson holes $N_B = 4$–9. The derived parameters are $a_J = 0.0283$ MeV and $b_J = -0.0001$ MeV.

Table 3
The quadrupole moments of the ground state $3/2^+$ in $^{191-199}$Au are adopted from Ref. [48]. Using Eq. (5), the effective boson charge are calculated.

Gold isotope	$Q_{3/2^+}$ (eb)	α_2 (eb)
191	+0.72 (2)	0.1085 (27)
193	+0.66 (2)	0.1106 (29)
195	+0.61 (2)	0.1130 (30)
197	+0.547 (16)	0.1154 (31)
	0.597 (10)	0.1259 (21)
199	+0.37 (1)	0.0901 (24)
	+0.510 (16)	0.1241 (39)
	0.55 (3)	0.1339 (73)
	0.64 (6)	0.1558 (146)

Assuming the IBM in the O(6) limit is valid for the bosonic core, the first excited 2^+ state has seniority $\tau = 1$ and the ground state is assigned $\tau = 0$. On the basis of a constant J splitting, the compression of excitation energy can only be expressed by a reduction of the τ splitting. Besides level energies, it is interesting to investigate whether other observables confirm the smooth evolution of collectivity along the odd–even gold isotopes. Particularly quadrupole moments are associated with collectivity, with high values describing strong deformation due to collective motion of the valence nucleons. In the Spin(6) Bose–Fermi symmetry, the quadrupole transition operator and the quadrupole moment are defined as [2]:

$$T^{E2}_{\mu} = \alpha_2 \left[s^{\dagger} \times \tilde{d} + d^{\dagger} \times \tilde{s} \right]^{(2)}_{\mu} + f_2 \left[a^{\dagger}_{3/2} \times \tilde{a}_{3/2} \right]^{(2)}_{\mu}, \tag{4}$$

$$Q_J = \sqrt{\frac{16\pi}{5}} \sqrt{\frac{J(2J-1)}{(2J+1)(J+1)(2J+3)}} \langle J || \mathrm{T(E2)} || J \rangle. \tag{5}$$

Here, α_2 is the effective boson charge and f_2 the effective fermion charge. We can use the simplification $\alpha_2 = f_2$ [1], as only the ground state quadrupole moments are known.

Table 3 lists the quadrupole moments of ground states adopted from Ref. [48]. In the case of ^{197,199}Au multiple quadrupole moments are known for the ground state and given in Table 3.

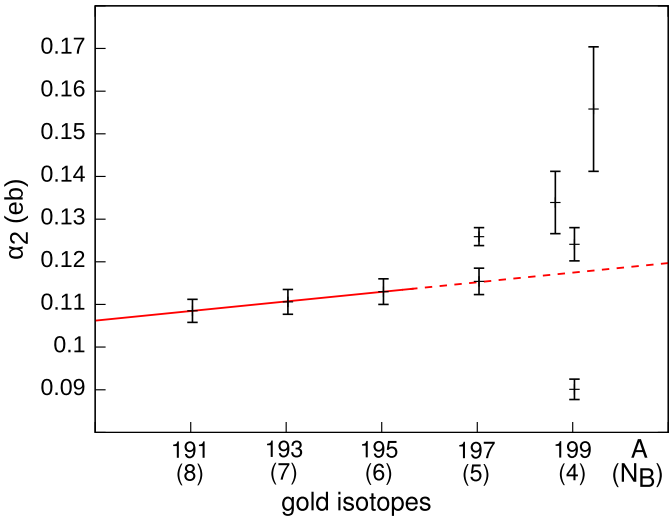

Fig. 6. (Color online.) A linear function $f(N_B) = a + b \times N_B$ is fitted to the effective boson charge α_2 in $^{191–195}$Au with the number of boson holes $N_B = 6$–8, indicated with a solid red line. The derived parameters are $a = 0.1265$ eb and $b = -0.0023$ eb. The dashed red line represents the projection of the linear fit to the heavier gold isotopes, which are not used for the fit. Note, for clarity the different quadrupole moments of ^{199}Au ($N_B = 4$) are slightly shifted in x direction.

In $^{185–189}$Au no such quadrupole moment exists since the ground state is $1/2^+$. The quadrupole moments are used to determine the effective boson charge and are listed in Table 3.

In Fig. 6 the different effective boson charges are plotted against the number of boson holes. For the lighter gold isotopes again a smooth evolution in visible, thus the linear function $f(N_B) = a + b \times N_B$ is fitted to the effective charges of $^{191–195}$Au and yields $a = 0.1265$ eb and $b = -0.0023$ eb. Again, the slope b is very flat, so a constant effective charge can be assumed for the odd–even gold isotopes. However, the effective boson charge derived from the quadrupole moments seriously underestimates the B($E2$) values. In order to obtain an effective boson charge which agrees with the measured $E2$ strength the simplification $\alpha_2 = f_2$ is not applied to Eq. (4). Thus, the effective boson and fermion charge are obtained using the transitions $1/2^+_1 \xrightarrow{61.5} 3/2^+_{g.s.}$ and $5/2^+_1 \xrightarrow{200.4} 1/2^+_1$ in ^{195}Au, yielding $\alpha_2 = 0.133$ and $f_2 = 0.313$. α_2 is very close to the parameter in Ref. [17]. These parameters are assumed to be constant for the odd–even nuclei and the B($E2$) values calculated whenever experimental values are available. The comparison between measured and theoretical $E2$ strength is given in Table 4 and yields overall a good agreement. The quadrupole moments are overestimated using the larger effective boson and fermion charge by approximately 0.2 eb for the ground states except for ^{199}Au, where $Q_{3/2^+,199\mathrm{Au}} = 0.64$ (6) eb is reproduced.

Another important test for the validity of the model are B($M1$) values, especially since in odd nuclei considerable $M1$ strength is observed. In Refs. [2,30,49] the $M1$ transition operator and its relation with gyromagnetic ratios, magnetic moments, and B($M1$) values are discussed in detail for ^{197}Au. Since in other odd–even gold isotopes available data is too scarce to perform a reasonable investigation of $M1$ strength, we refer to these works.

4. Conclusion

The experiment performed at the Cologne tandem accelerator provided vital information (the determination of spins, transitions, and especially, the observation of new states) to investigate the Spin (6) Bose–Fermi symmetry in the odd–even gold isotopes. For $^{185–199}$Au the calculated and

Table 4
Comparison of calculated $E2$ strength with measured B($E2$) values from Refs. [38,23,39,40,17] and this work.

	E_{initial} (keV)	J^{π}_{initial}	E_{final} (keV)	J^{π}_{final}	E_{γ} (keV)	B($E2$)$_{\text{theory}}$ (e^2b^2)	B($E2$)$_{\text{NDS}}$ (e^2b^2)
^{193}Au	38.2	$1/2^+$	0.0	$3/2^+$	38.2	0.343	0.304 (80)
	224.8	$3/2^+$	38.2	$1/2^+$	189.6	0.160	$\geqslant$0.0
		$3/2^+$	0.0	$3/2^+$	224.8	–	$\geqslant$0.053
	258.0	$5/2^+$	38.2	$1/2^+$	219.8	0.067	0.101 (20)
		$5/2^+$	0.0	$3/2^+$	258.0	0.343	0.272 (5)
^{195}Au	61.4	$1/2^+$	0.0	$3/2^+$	61.4	0.275	0.275 (27)
	241.6	$3/2^+$	61.4	$1/2^+$	180.1	0.125	$\geqslant$0.022
	241.6	$3/2^+$	0.0	$3/2^+$	241.6	–	$\geqslant$0.007
	261.8	$5/2^+$	61.4	$1/2^+$	200.4	0.058	0.058 (13)
		$5/2^+$	0.0	$3/2^+$	261.8	0.275	0.121 (27)
^{197}Au	77.4	$1/2^+$	0.0	$3/2^+$	77.4	0.213	0.238 (20)
	268.8	$3/2^+$	77.4	$1/2^+$	191.4	0.094	0.123 (20)
		$3/2^+$	0.0	$3/2^+$	268.9	–	$\geqslant$0.126
	279.0	$5/2^+$	77.4	$1/2^+$	201.6	0.050	0.098 (12)
		$5/2^+$	0.0	$3/2^+$	279.0	0.213	0.177 (41)
	502.5	$5/2^+$	77.4	$1/2^+$	425.0	0.108	0.052 (23)
		$5/2^+$	0.0	$3/2^+$	502.6	–	0.047 (41)
	547.5	$7/2^+$	279.0	$5/2^+$	268.5	0.073	0.012 (5)
		$7/2^+$	268.8	$3/2^+$	278.7	0.015	0.046 (14)
		$7/2^+$	0.0	$3/2^+$	547.5	0.213	0.224 (20)
	736.7	$7/2^+$	279.0	$5/2^+$	457.7	0.137	0.143 (41)
		$7/2^+$	268.8	$3/2^+$	468.1	0.020	0.041 (27)
	855.5	$9/2^+$	547.5	$7/2^+$	308.0	0.057	0.068 (48)
		$9/2^+$	279.0	$5/2^+$	576.5	0.210	0.279 (34)
^{199}Au	77.2	$1/2^+$	0.0	$3/2^+$	77.2	0.158	0.166 (90)
	317.1	$5/2^+$	77.2	$1/2^+$	239.9	0.043	$\geqslant$0.037
		$5/2^+$	0.0	$3/2^+$	317.1	0.158	$\geqslant$0.049
	323.7	$3/2^+$	77.2	$1/2^+$	246.5	0.066	$\leqslant$0.283
	493.8	$7/2^+$	323.6	$3/2^+$	170.6	0.011	$\geqslant$0.041
		$7/2^+$	0.0	$3/2^+$	493.8	0.158	$\geqslant$0.052
	543.0	$5/2^+$	323.7	$3/2^+$	219.4	0.010	$\geqslant$0.016
		$5/2^+$	317.1	$5/2^+$	225.9	0.029	$\geqslant$0.004
		$5/2^+$	77.2	$1/2^+$	468.8	0.113	$\geqslant$0.004

experimental level schemes for the $\tau_1 = 1/2, 3/2, 5/2$ multiplets were compared, revealing, that not only the agreement is very good, but also the switch of the ground state from $1/2^+$ to $3/2^+$ in ^{191}Au is predicted correctly. The parameters derived from a least-squares fit reflect the smooth evolution of levels in $^{189–199}$Au. Since the J splitting is almost constant, solely the τ splitting indicates the increasing collectivity towards mid-shell. Indeed, it turns out that the evolution of parameters B and C throughout $^{189–199}$Au can be predicted and the energy of states belonging to the $\tau_1 = 1/2, 3/2, 5/2$ multiplet can be expressed by the simple equation (all numerical values in MeV):

$$E(N_B) = E_0 + (0.0435 - N_B \times 0.0032)\big(\tau_1(\tau_1+3) + \tau_2(\tau_2+1)\big) + (0.0283 + N_B \times 0.0001)\big(J(J+1)\big). \quad (6)$$

We can conclude from this equation, that the compression of level energies with the increasing number of boson holes can mainly be attributed to collectivity. In fact, the linear dependency of collectivity for the excited states is expected if other interactions are stable. The analysis of the experimental levels for ^{185,187}Au and the proximity to shape coexistence in the even–even mercury isotopes [43] and platinum isotopes [47] suggest, that the Spin(6) Bose–Fermi symmetry is not applicable to these nuclei.

The quadrupole moments available for the odd–even gold isotopes support the observation of a very smooth change of nuclear properties in $^{189–199}$Au. This is stressed by the good agreement between calculated and observed B($E2$) values. The calculated B($E2$) values are based on effective boson charge and effective fermion charge derived solely from B($E2$) transitions in ^{195}Au and seem to be valid for the other odd–even gold isotopes. However, using the effective boson charge and fermion charge, a simultaneous description of both, quadrupole moments and B($E2$) values, is not possible. The quadrupole moments are overestimated by approximately 0.2 eb, although the evolution of the quadrupole moments to smaller values towards shell closure is reproduced.

Overall, the Spin(6) Bose–Fermi symmetry quite successfully describes the properties of odd–even gold isotopes, particularly considering the simplicity of the model employed by restricting the fermion to the $\pi 2d_{3/2}$ orbital.

Acknowledgements

We thank our coworkers and the Tandem accelerator staff at the IKP Köln for their help during the experiment. We thank R.V. Jolos for fruitful discussions concerning this work. Part of this work was supported by DFG under grant JO391/2-1 and JO391/3-2.

References

[1] A. Arima, F. Iachello, The Interacting Boson Model, Cambridge University Press, Cambridge, England, 1987.
[2] F. Iachello, P. Van Isacker, The Interacting Boson Fermion Model, Cambridge University Press, Cambridge, England, 1991.
[3] A. Frank, P. Van Isacker, Algebraic Methods in Molecular & Nuclear Structure Physics, Wiley–Interscience, New York, USA, 1994.
[4] A. Frank, J. Jolie, P. Van Isacker, Symmetries in Atomic Nuclei – From Isospin to Supersymmetry, Springer, New York, USA, 2009.
[5] A. Metz, J. Jolie, G. Graw, R. Hertenberger, J. Gröger, C. Günter, N. Warr, Y. Eisermann, Phys. Rev. Lett. 83 (1999) 1542.
[6] J. Gröger, et al., Phys. Rev. C 62 (2000) 064304.
[7] H.-F. Wirth, et al., Phys. Rev. C 70 (2004) 014610.
[8] P. Van Isacker, J. Jolie, K. Heyde, A. Frank, Phys. Rev. Lett. 54 (1985) 653.
[9] P. Navrátil, J. Dobes, Phys. Rev. C 37 (1988) 2126.
[10] J.-M. Régis, Diploma thesis, University of Cologne, 2007, unpublished.
[11] J.-M. Régis, T. Materna, G. Pascovici, S. Christen, A. Dewald, C. Fransen, J. Jolie, P. Petkov, K.O. Zell, Rev. Sci. Instrum. 81 (2010) 113505.
[12] F. Pühlhofer, Nucl. Phys. A 280 (1977) 267.
[13] A. Linnemann, Ph.D. thesis, University of Cologne, 2005, http://kups.ub.uni-koeln.de/1747/.
[14] K.S. Krane, R.M. Steffen, Phys. Rev. C 2 (1970) 724.
[15] K.S. Krane, R.M. Steffen, R.M. Wheeler, At. Data Nucl. Data Tables 11 (1973) 351.
[16] I. Wiedenhöver, Code CORLEONE, University of Cologne, 1995, unpublished.
[17] T. Thomas, C. Bernards, J.-M. Régis, M. Albers, C. Fransen, J. Jolie, S. Heinze, D. Radeck, N. Warr, K.-O. Zell, Nucl. Phys. A 922 (2014) 200.
[18] C. Bernards, S. Heinze, J. Jolie, C. Fransen, A. Linnemann, D. Radeck, Phys. Rev. C 81 (2009) 024312.

[19] J. Frana, A. Spalek, M. Fiser, A. Kokes, Nucl. Phys. A 165 (1971) 625.
[20] K. Farzine, V.H. Buttlar, Z. Phys. C 270 (1974) 155.
[21] C. Vieu, A. Peghaire, J.S. Dionisio, Rev. Phys. Appl. 8 (1973) 231.
[22] L.H. Goldmann, B.L. Cohen, R.A. Moyer, R.C. Diehl, Phys. Rev. C 2 (1970) 561.
[23] Zhou Chunmei, Nucl. Data Sheets 86 (1998) 645.
[24] R. Bijker, A.E.L. Dieperink, Nucl. Phys. A 379 (1982) 221.
[25] J.M. Arias, C.E. Alonso, M. Lozano, Phys. Rev. C 33 (1986) 1482.
[26] P.B. Semmes, A.F. Barfield, B.R. Barrett, J.L. Wood, Phys. Rev. C 35 (1987) 844.
[27] F. Iachello, S. Kuyucak, Ann. Phys. 136 (1981) 19.
[28] C.D. Papanicolopulos, J. L, Wood, J.D. Cole, J.H. Hamilton, K.S. Krane, R.L. Mlekodaj, A.V. Ramayya, M. Huyse, L. Vanneste, E.F. Zganjar, ORNL 6004 (1983) 180.
[29] J.L. Wood, Phys. Rev. C 24 (1981) 4.
[30] A.E. Stuchbery, L.D. Wood, H.H. Bolotin, C.E. Doran, I. Morrison, A.P. Byrne, G.J. Lampard, Nucl. Phys. A 486 (1988) 374.
[31] J. Vervier, Phys. Lett. B 100 (1981) 383.
[32] J. Vervier, R. Holzmann, R.V.F. Janssens, M. Loiselet, M.A. Van Hove, Phys. Lett. B 105 (1981) 343.
[33] U. Mayerhofer, T. von Egidy, J. Jolie, H.G. Borner, G. Colvin, S. Judge, B. Krusche, S.J. Robinson, K. Schreckenbach, S. Brant, V. Paar, Z. Phys. A 341 (1991) 1.
[34] M.S. Basunia, Nucl. Data Sheets 106 (2005) 619.
[35] M.S. Basunia, Nucl. Data Sheets 110 (2009) 999.
[36] S.-c. Wu, H. Niu, Nucl. Data Sheets 100 (2003) 1.
[37] V.R. Vanin, et al., Nucl. Data Sheets 108 (2007) 2393.
[38] E. Achterberg, G.V. Marti, V.R. Vanin, et al., Nucl. Data Sheets 107 (2006) 1.
[39] Huang Xiaolong, Zhou Chunmei, Nucl. Data Sheets 104 (2005) 283.
[40] Balraj Singh, Nucl. Data Sheets 108 (2007) 79.
[41] S.G. Nilsson, Dan. Mat. Fys. Medd. 29 (16) (1955).
[42] S. Heinze, Ph.D. thesis, University of Cologne, 2008, http://kups.ub.uni-koeln.de/2357/.
[43] M. Scheck, et al., Phys. Rev. C 83 (2011) 037303.
[44] K. Heyde, J.L. Wood, Rev. Mod. Phys. 83 (2011) 1467.
[45] A.E. Stuchbery, S.S. Anderssen, A.P. Byrne, P.M. Davidson, G.D. Dracoulis, G.J. Lane, Phys. Rev. Lett. 79 (1996) 13.
[46] M.K. Harder, K.T. Tang, P. Van Isacker, Phys. Lett. B 405 (1997) 25.
[47] I.O. Morales, A. Frank, C.E. Vargas, P. Van Isacker, Phys. Rev. 78 (2008) 024303.
[48] N.J. Stone, At. Data Nucl. Data Tables 90 (2005) 75.
[49] H.H. Bolotin, D.L. Kennedy, B.J. Linard, A.E. Stuchbery, S.H. Sien, I. Katayama, H. Sakai, Nucl. Phys. A 321 (1979) 231.

Chapter 4

The molybdenum isotopes

PHYSICAL REVIEW C **88**, 044305 (2013)

Evidence for shape coexistence in ^{98}Mo

T. Thomas,[1,2,*] K. Nomura,[1,3] V. Werner,[2] T. Ahn,[2] N. Cooper,[2] H. Duckwitz,[1] M. Hinton,[2,4] G. Ilie,[2] J. Jolie,[1] P. Petkov,[1,5] and D. Radeck[1]

[1]*Institut für Kernphysik, Universität zu Köln, Zülpicher Straße 77, D-50937 Köln, Germany*

[2]*Wright Nuclear Structure Laboratory, Yale University, New Haven, Connecticut 06520, USA*

[3]*Grand Accélérateur National d'Ions Lourds, CEA/DSM-CNRS/IN2P3, Boulevard Henri Becquerel, F-14076 Caen Cedex 05, France*

[4]*Department of Physics, University of Surrey, Guildford GU2 7XH, United Kingdom*

[5]*Bulgarian Academy of Science, Institute for Nuclear Research and Nuclear Energy, Tsarigradsko Chausse 72, 1784 Sofia, Bulgaria*

(Received 6 June 2013; revised manuscript received 5 September 2013; published 7 October 2013)

A $\gamma\gamma$ angular-correlation experiment has been performed to investigate the low-energy states of the nucleus ^{98}Mo. The new data, including spin assignments, multipole mixing ratios, and lifetimes reveal evidence for shape coexistence and mixing in ^{98}Mo, arising from a proton intruder configuration. This result is reproduced by a theoretical calculation within the proton-neutron interacting boson model with configuration mixing, based on microscopic energy density functional theory. The microscopic calculation indicates the importance of the proton particle-hole excitation across the $Z = 40$ subshell closure and the subsequent mixing between spherical vibrational and the γ-soft equilibrium shapes in ^{98}Mo.

DOI: 10.1103/PhysRevC.88.044305 PACS number(s): 21.60.Jz, 21.60.Fw, 23.20.En, 25.55.−e

I. INTRODUCTION

For decades, clarifying the nature of shape coexistence has been one of the major objectives in nuclear structure physics [1,2]. The phenomenon has been observed in various regions of the nuclear chart, from light [3] to heavy [4] systems. In ^{186}Pb, for example, three low-lying 0^+ states bunch together in energy within the range of 700 keV [4]. The emergence of the extremely low-lying 0^+ states is, in terms of the spherical shell model, attributed to two- or four-proton excitations across the $Z = 82$ shell closure. The residual interaction between protons and neutrons leads to the lowering of the excited 0^+ states and the different corresponding shell-model configurations are linked to relevant geometrical deformations in a mean-field picture [5].

The $A \sim 100$ mass region also presents a unique laboratory for the evolution of nuclear shape and shape coexistence [6,7]. The interplay between single-particle and collective degrees of freedom leads to shape phase transitions along isotopic and isotonic chains [8]. The most dramatic examples for shape coexistence and shape transition occur in the Zr isotopic chain, as recently revealed for ^{94}Zr [9]. Especially in the $N = 50$–56 Zr isotopes the 0_1^+ state and the very low-lying 0_2^+ state are considered strongly mixed $0p$-$0h$ and $2p$-$2h$ proton configurations, where protons are promoted from the pf shell to the $g_{9/2}$ orbital, as also found in shell-model calculations [6,10]. The structure of the low-lying 0_2^+ state in $N \geqslant 58$ Zr isotopes is somewhat more complicated due to neutron contributions. In Mo isotopes, starting from $N = 50$, the nuclear shape gradually evolves from a sphere and, driven by the enhanced proton-neutron residual interaction, large deformation sets in at $N \approx 60$ [11]. Situated in between, $^{98}_{42}$Mo$_{56}$ is pivotal for understanding shape transitions in this mass region. In particular, the concept of shape coexistence can apply to this nucleus, where proton cross-shell excitations from the $Z = 28$–40 pf shell to the $\pi g_{9/2}$ orbit may play an important role [12]. In fact, experimentally, the first-excited state of ^{98}Mo has been shown to be an coexisting isomeric 0^+ state of different shape [13,14]. The mixing between the proton $2p$-$0h$ and $4p$-$2h$ configurations forms the first excited 0^+ state and the ground state as revealed by the investigation of γ transitions depopulating 1^+ states with equal strengths to both 0^+ states [12], akin to the findings for ^{92}Zr [6].

To address the important issue of the nature of low-lying structure in ^{98}Mo, we performed a $\gamma\gamma$ angular-correlation experiment. In this paper, the results of this experiment are reported as well as the identification of shape coexistence and the role of a proton intruder configuration in ^{98}Mo. The experimental results are supported by predictions of the interacting boson model [15] with configuration mixing, where the Hamiltonian is determined microscopically. The microscopic calculation indicates the importance of the proton intruder configuration and the substantial mixing between spherical-vibrational and γ-unstable shapes in ^{98}Mo.

II. EXPERIMENTAL PROCEDURE

In order to extend the ^{98}Mo level scheme, we used the reaction ^{96}Zr(α, $2n$)^{98}Mo. A 16 MeV α beam was delivered by the extended stretched transuranium (ESTU) tandem accelerator at the Wright Nuclear Structure Laboratory, Yale University, impinging on a 1.25 mg/cm^2 thick ^{96}Zr target enriched to 57.36%. The γ transitions were detected by 10 Compton-suppressed high-purity Ge (HPGe) Clover detectors of the YRAST Ball array [16]. During five days of measurement, 1.2×10^9 events were collected using a $\gamma\gamma$ coincidence trigger.

Figure 1 shows the total projection of the $\gamma\gamma$ coincidence data. Due to impurities in the ^{96}Zr target transitions from $^{93–99}$Mo isotopes were observed. The most prominent peaks are labeled with their associated nuclear origin. The data

*tim.thomas@ikp.uni-koeln.de

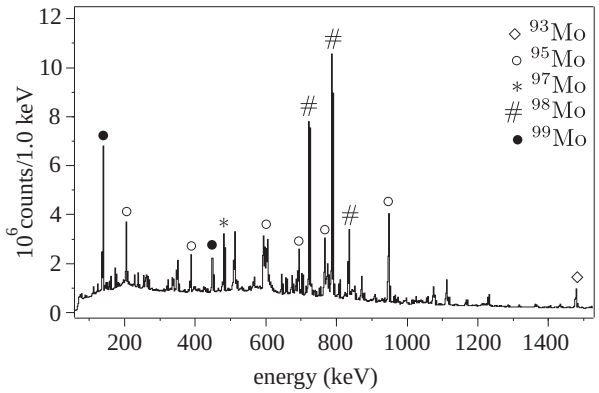

FIG. 1. Total projection of the $\gamma\gamma$ coincidence data. Major peaks from ^{98}Mo and the main side reactions are marked.

were sorted into 11 correlation group matrices, which account for detector pairs at angles Θ_1 and Θ_2 with respect to the beam axis and a relative angle ψ between the plains spanned by the detectors and the beam axis, in order to perform a $\gamma\gamma$ angular-correlation analysis. Relative intensities in the correlation groups were then fit to angular-correlation functions to extract spins and multipole mixing ratios, as described in Refs. [17,18], by using the computer code CORLEONE [19,20]. The code takes into account the attenuation factors of the detectors [21,22]. An example of a $\gamma\gamma$ angular-correlations analysis is shown in Fig. 2 for the $2_4^+ \xrightarrow{1419} 2_1^+ \xrightarrow{787} 0_{gs}^+$ cascade, yielding the hitherto unknown multipole mixing ratio $\delta_{1419} = 0.33 \pm 0.11$. In the literature [23], conflicting multipole mixing ratios are given for γ transitions depopulating low-lying states in ^{98}Mo. The superior sensitivity of the present setup allowed us to resolve discrepancies. For more detailed information about $\gamma\gamma$ angular-correlations analysis with the YRAST Ball array see Refs. [22,24]. In the same way, the multipole mixing ratio of the $2_2^+ \xrightarrow{644} 2_1^+$ transition was measured to be $+1.67\,(25)$, which is in agreement with the larger solution from an $(n, n'\gamma)$ experiment [25] and refutes the most recent value from Coulomb excitation [14].

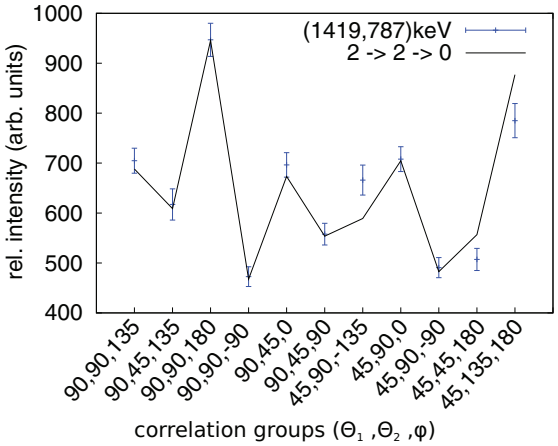

FIG. 2. (Color online) Comparison of a fitted theoretical angular correlation (solid line) with relative intensities obtained from 11 correlation groups for the 1419–787 keV $\gamma\gamma$ coincidence.

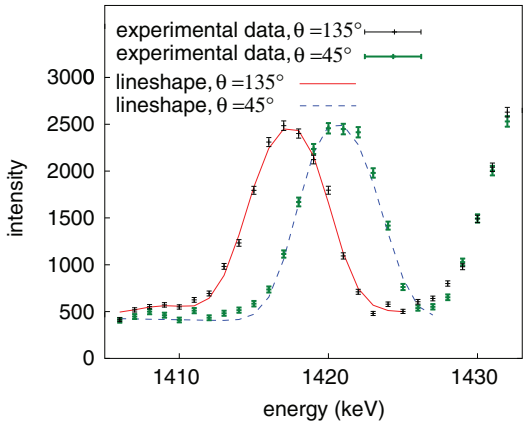

FIG. 3. (Color online) Determination of the effective lifetime of the 1419 keV transition depopulating the 2_4^+ state using a gate set on the 787 keV transition. Coincidence spectra with a gate set on the 787 keV transition for two different angles are shown. The red solid line represents the simulated lineshape at forward angle and the blue dashed line the backward angle. The effective average lifetime is $\tau = 0.30\,(7)$ ps.

Lifetimes of excited states were determined using the Doppler-shift attenuation method (DSAM) [26]. The data was sorted into three matrices according to the three angles $\theta = 45°$, $90°$, $135°$ of the detectors relative to the beam axis. For the lineshape analysis, the stopping process of an excited nucleus is simulated using nuclear [27] and electronic stopping powers [28]. In Fig. 3, a lineshape analysis for the 1419 keV transition depopulating the 2_4^+ state is shown. The weighted mean value over the angles for the effective lifetime is calculated to be $\tau = 0.30\,(7)$ ps. The analysis procedure is outlined in more detail in Ref. [29].

III. THEORETICAL PROCEDURE

To interpret the nature of the low-lying structure and the relevant shape dynamics in ^{98}Mo, we performed a self-consistent mean-field calculation using the Skyrme energy density functional (EDF) (see Ref. [30] for review). Figure 4(a) shows the total energy surface of ^{98}Mo in terms of the axial quadrupole deformation β and triaxiality γ [31] obtained through the constrained Hartree-Fock-BCS (HF-BCS) method with the Skyrme functional SLy6 [32] using the code EV8 [33]. Figure 4(a) displays two minima in the mean-field energy surface, with the deeper one being close to a spherical shape ($\beta \approx 0$) and the other at $\beta \approx 0.21$ and $\gamma \approx 20°$ with some degree of softness. On the other hand, no coexisting minima are visible in the microscopic energy surfaces of the adjacent nuclei ^{96}Mo [Fig. 4(c)] and ^{100}Mo [Fig. 4(d)]. ^{98}Mo appears to be transitional between near-spherical (^{96}Mo) and deformed (^{100}Mo) shapes.

To study quantitatively the spectroscopic observables associated with the intrinsic shape of interest, it is necessary to go beyond the mean-field approximation. In this work we resort to the proton-neutron interacting boson model (IBM-2) [15,34] to generate spectra and transition rates that are comparable to data. By mapping the microscopic energy surface onto the

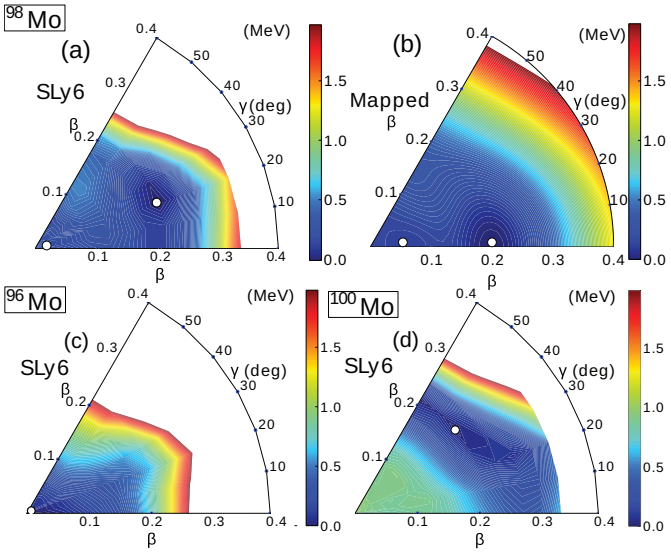

FIG. 4. (Color online) Contour plots of the microscopic (a) and the mapped (b) energy surfaces in (β, γ) plane of ^{98}Mo, and of the microscopic energy surfaces of the adjacent nuclei ^{96}Mo (c) and ^{100}Mo (d). The color code ranges from 0 (mean-field minimum) to 2 MeV, and the minima are identified by the solid white circles. The Skyrme SLy6 functional is used.

equivalent IBM-2 Hamiltonian in the boson condensate [35], the Hamiltonian parameters are determined microscopically, thereby not invoking any adjustment to data (cf. Refs. [36,37] for details). The mapped Hamiltonian is to be diagonalized numerically in the boson m-scheme basis to provide level energies and transition rates with good quantum numbers in the laboratory frame. We note that the above-mentioned procedure is similar to that used in Ref. [38], where it was used to make a prediction on the structure of ^{96}Kr, whereas in the present work we put this procedure to a more crucial test.

In order to describe the two mean-field minima, the model space of the IBM-2 needs to be extended by including the intruder configuration and by mixing the Hamiltonians associated with the two configurations [39]. From the observed systematics of the two-neutron separation energies (see, e.g., Ref. [40] for a review), the $N = 56$ neutron subshell gap is only notable for $Z \leqslant 40$, and the gap becomes rapidly quenched for higher Z ($\geqslant$42). This indicates that proton intruder states are more significant for heavier Mo isotopes than neutron shell effects. Furthermore, the calculated single-particle energies as functions of the β deformation indicate the lowering of the proton $g_{9/2}$ orbitals and the occupation of the last protons in the orbitals at $\beta \approx 0.2$ associated with the γ-soft minimum in Fig. 4(a). These considerations lead us to take the IBM-2 model space including the two-proton excitation across the $Z = 40$ shell. The ^{90}Zr nucleus is then taken to be the inert core, and the number of proton bosons is 1 and 3 for the normal and the intruder configurations, respectively, while the neutron boson number is fixed at 3. Note that normal (intruder) configuration denotes hereafter the proton $2p$-$0h$ ($4p$-$2h$) configuration. The full Hamiltonian of the system is then given as [38]

$$H = P_{\rm nor} H_{\rm nor} P_{\rm nor} + P_{\rm intr}(H_{\rm intr} + \Delta) P_{\rm intr} + H_{\rm mix}, \quad (1)$$

TABLE I. The intrinsic deformation parameter β_2 for the lowest-three excited 2^+ states. The theoretical values extracted from the intrinsic quadrupole moments obtained by the IBM-2 ($K = 0$ is assumed) $\beta_2^{\rm IBM}$, and the equivalent values $\beta_2^{\rm MF}$ associated with the mean-field minima, and the experimental values $\beta_2^{\rm expt}$ from inelastic scattering of deuterons [43,44] and Coulomb excitation [45] are shown.

$E_{\rm level}$ (keV)	J^π	$\beta_2^{\rm MF}$	$\beta_2^{\rm IBM}$	$\lvert\beta_2^{(d,d')}\rvert$	$\lvert\beta_2^{\rm CoulEx}\rvert$[a]
787.26	2_1^+	(+0.21)	+0.132	0.167 (4)[b]	0.174 (5)
1432.29	2_2^+	(≈0.0)	+0.060	0.046[c]	0.037 (2)
1758.32	2_3^+		−0.121	0.029[c]	0.11 (5)

[a]Taken from Ref. [45].
[b]Taken from Ref. [44].
[c]Taken from Ref. [43].

where $H_{\rm nor}$ ($H_{\rm intr}$) and $P_{\rm nor}$ ($P_{\rm intr}$) represent the Hamiltonian of and the projection operator onto the normal (intruder) configuration space, respectively. Δ and $H_{\rm mix} = \omega(s_\pi^\dagger s_\pi^\dagger + d_\pi^\dagger d_\pi^\dagger) + {\rm H.c.}$ stand for the energy offset needed for the proton cross-shell excitation and interaction that mixes two configurations, respectively. The resulting mapped IBM-2 energy surface is shown in Fig. 4(b). One can see in Fig. 4(b) two equivalent minima near $\beta \approx 0$ and $\beta \approx 0.2$, with the latter being γ soft similarly to the microscopic energy surface.[1]

IV. RESULTS AND DISCUSSION

The calculation predicts a spectroscopic quadrupole moment for the 2_1^+ state of $Q(2_1^+) = -0.245e$b, corresponding to a weak prolate deformation. This is consistent with a previous experimental value of $Q(2_1^+) = -0.25\,(9)e$b [42], but differs from the more recent one, $Q(2_1^+) = -0.05\,(2)e$b [14]. We note that the latter result stems from a global fit to data taking known multipole mixing ratios and lifetimes into account. Some of these input data have been changed and complemented by our present measurement. In Table I, we give the intrinsic β-deformation parameters for the lowest three 2^+ states, taken from inelastic scattering [43,44] and Coulomb excitation [45] data. These data are compared to the value obtained from the minima in the mean-field energy surface [Fig. 4(a)], and the deformation extracted from the intrinsic quadrupole moment in the IBM-2, assuming $K = 0$. The best agreement is found with Coulomb excitation values from Ref. [45].

Next we analyze the structure of the low-energy level scheme of ^{98}Mo. Figure 5 compares the data from the present experiment (left-hand side) and the calculated spectra after (center) and before the mixing, i.e., unperturbed configurations (right-hand side). Note that some experimental states, which are close in energy and have the same spin, have been identified

[1]A minimum at $\gamma = 20°$, however, is not obtained with the used Hamiltonian containing up to only two-body boson terms. It has been shown [41] that a three-body boson term should be included in the IBM Hamiltonian to give rise to the triaxial minimum and to better describe the detailed structure of the quasi-γ band. This is, however, not particularly of relevance for the present paper.

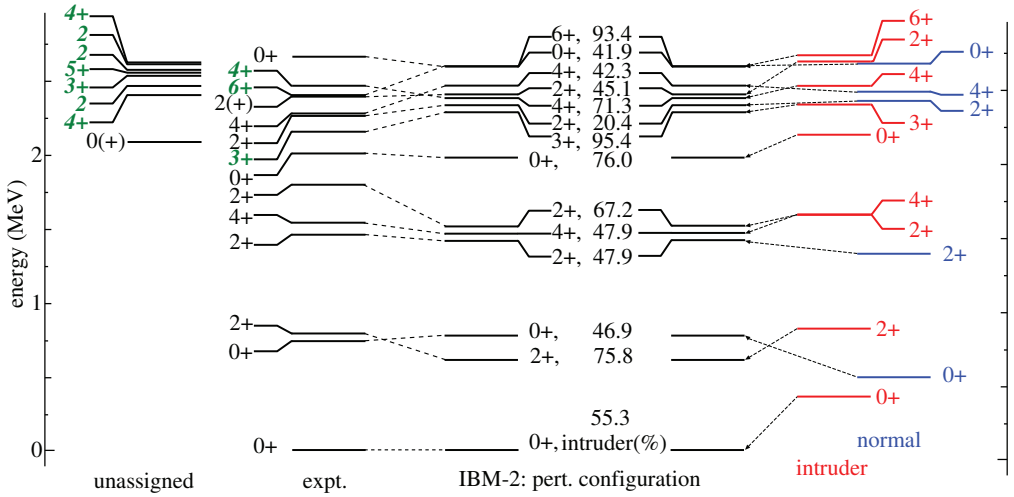

FIG. 5. (Color online) Low-energy level scheme of ^{98}Mo. The experimental (left) and the calculated spectra with mixing ("IBM-2: pert. configuration," center) and without mixing (right). New spin assignments are denoted in italic letters. The number indicated next to spin value (center) represents the fraction of the intruder configuration in the wave function of each state.

from the comparison to predicted B(E2) values (cf. Tables II and III). Even though the energy levels are calculated without any fit to data; that is, the Hamiltonian parameters are derived solely from the microscopic EDF and the mapping procedure, the overall agreement between data and calculation in Fig. 5 is remarkably good. While the experimental 0_2^+ excitation energy is well reproduced by the theory, the calculated 2_1^+ level energy seems rather low compared with the experimental value. The reason is the strong level repulsion between the unperturbed low-spin states of the two configurations due to a rather large mixing strength. In the experiment an excess of states is observed above the 0_4^+ state, which could not be assigned to predicted states. These might originate from a more complicated structure eventually associated with higher-order effects such as the four-proton cross-shell excitation and/or the excitation of neutrons, which are outside of the model space of the present calculation.

Looking into the origin of each state in a more quantitative manner, first we notice on the right-hand side of Fig. 5 that the unperturbed 0_1^+ and 0_2^+ states of the normal and the intruder configurations are very close in energy. After the mixing, the 0^+ ground states in each configuration repel each other by $\approx$350 keV in energy (as illustrated by arrows). Here, the matrix element $\langle H_{\rm mix}\rangle$, which mixes unperturbed 0_1^+ states of the normal and the intruder configurations, is calculated to be 385 keV. This value is consistent with the result from a schematic two-level mixing calculation of 326 keV [12]. In the resulting 0_1^+ and 0_2^+ states, normal and intruder configurations

TABLE II. Theoretical E2 transition strengths (in W.u.) compared to experimental values from Refs. [14,23] and from this work. States in bold are predicted to be of intruder nature in theory. For transitions with mixed multipolarity the multipole mixing ratio δ measured in the present experiment is given.

$E_{\rm level}$ (keV)	J_I^π	E_γ (keV)	J_F^π	B(E2)$_{\rm theor}$	B(E2)$_{\rm expt}$	$\delta_{\rm expt}$
787.26[a]	$\mathbf{2_1^+}$	787.26	$\mathbf{0_1^+}$	27	$21.4\,^{+11}_{-10}$	
		52.6	0_2^+	256	280 (40)[b]	
1432.29[a]	2_2^+	644.70	$\mathbf{2_1^+}$	22	47.8^{+132}_{-100}	+1.67 (25)
		697.10	0_2^+	8	2.5^{+8}_{-6}	
		1432.29	$\mathbf{0_1^+}$	0.03	1.0^{+2}_{-1}	
1509.74[a]	4_1^+	722.48	$\mathbf{2_1^+}$	49	$49.1^{+5.5}_{-4.5}$	
1758.32[a]	$\mathbf{2_3^+}$	326.05	2_2^+	13	4.7^{+189}_{-23}	−0.17 (22)
		971.03	$\mathbf{2_1^+}$	6	3.2^{+134}_{-16}	−0.97 (14)
		1023.61	0_2^+	7	7.8^{+286}_{-34}	
2206.74	2_4^+	1419.48	$\mathbf{2_1^+}$	1.3	1.7 (2)	−0.33 (11)
2333.03	$2_5^{(+)}$	900.85	2_2^+	1	1.6^{+8}_{-4}	$-0.15^{+0.19}_{-0.20}$
2343.26[c]	$\mathbf{6_1^+}$	833.52	4_1^+	56	10.1 (4)	

[a] τ Adopted from Ref. [45].
[b] B(E2) adopted from Ref. [23].
[c] τ Adopted from Ref. [14].

TABLE III. Same as Table II, but normalized with respect to the largest B(E2) value among the depopulating decays from a given initial state.

$E_{\rm level}$ (keV)	J_I^π	E_γ (keV)	J_F^π	B(E2)$^{\rm rel}_{\rm theor}$	B(E2)$^{\rm rel}_{\rm expt}$	$\delta_{\rm expt}$
1962.81	$\mathbf{0_3^+}$	530.61	2_2^+	1	1	
		1175.57	$\mathbf{2_1^+}$	0.10	0.05 (1)	
2104.66	$\mathbf{3_1^+}$	594.65	4_1^+	0.66	<0.40[a]	
		672.50	2_2^+	1	1	$+6.66^{+3.41}_{-1.71}$
		1317.37	$\mathbf{2_1^+}$	0.13	0.04 (3)	$+2.91^{+0.64}_{-0.46}$
2223.74	$\mathbf{4_2^+}$	713.80	4_1^+	1	1	+1.13 (17)
		791.58	2_2^+	1.60	0.88 (11)	
		1436.68	$\mathbf{2_1^+}$	0.03	0.04 (1)	
2419.48	$\mathbf{4_4^+}$	661.16	$\mathbf{2_3^+}$	1	1	
		909.52	4_1^+	0.54	0.33 (3)	−0.64 (10)
		1632.46	$\mathbf{2_1^+}$	0.06	0.02 (1)	

[a] Branching ratio adopted from Ref. [23], no multipole mixing ratio available, assumed to be a pure E2 transition.

are almost equally mixed with fraction of 55.3% and 46.9%, respectively.

One should also notice that the unperturbed normal and the intruder level schemes exhibit, to a certain extent, vibrational and γ-soft characteristics, respectively. Within the unperturbed intruder configuration, the $R_{4/2} = E(4_1^+)/E(2_1^+)$ ratio of 2.67, as well as the closely lying 4_1^+, 2_2^+ states, in which a two-phonon 0^+ state is absent, is typical for a γ-soft structure. The unperturbed normal configuration, in contrast, displays closely lying 4_1^+, 2_2^+, and 0_2^+ states, more typical for a spherical vibrator. Also the $R_{4/2} = 2.32$ of the unperturbed normal configuration deviates strongly from deformed values toward the spherical harmonic oscillator ($R_{4/2} = 2.0$). This interpretation correlates with the microscopic energy surface in Fig. 4(a) and is consistent with previous empirical IBM-2 fitting calculations [46].

Finally, in Tables II and III we compare experimental and theoretical B(E2) values. Lifetimes are either adopted from Ref. [14] or measured in the present experiment. If not stated differently, all multipole mixing ratios and branching ratios are from the present work. The conversion coefficient α was obtained from calculations using the code BRICC [47]. Very good agreement between experiment and theory is obtained, confirming the strong mixing between both configurations. In particular, the strong $B(\mathrm{E2}; 2_1^+ \to 0_2^+)$ and $B(\mathrm{E2}; 2_2^+ \to 2_1^+)$ transitions, relative to the $2_1^+ \to 0_1^+$ transition (see Table II), present a stringent test of configuration mixing. The measured $B(\mathrm{E2}; 6_1^+ \to 4_1^+)$ is much smaller than predicted, perhaps due to fragmentation.

In Table III we compare relative B(E2) values, normalized with respect to the largest B(E2) value among the depopulating decays from a given initial state, for the states without lifetime information. Note that the three $4^+_{2,3,4,\mathrm{expt}}$ states are observed within 200 keV. From comparison of relative B(E2) values the $4^+_{2,\mathrm{expt}}$ state can be assigned to the predicted $4^+_{3,\mathrm{theor}}$ state generated mainly by the intruder configuration, while the $4^+_{4,\mathrm{expt}}$ state can be assigned to a strongly mixed $4^+_{2,\mathrm{theor}}$ state. Table III shows the same extent of consistency as obtained in Table II.

V. CONCLUSION

We have revealed robust experimental evidence for shape coexistence and configuration mixing in the low-lying structure of ^{98}Mo. Key data on multipole mixing ratios and lifetimes have been obtained, allowing for a detailed comparison with a new theoretical calculation within the IBM based on the microscopic EDF. The EDF calculation predicted two (near-spherical and γ-soft) mean-field minima in the energy surface [Fig. 4(a)], which necessitates the extension of the IBM to include a intruder configuration associated with the proton excitation across the $Z = 40$ subshell closure. The two intrinsic shapes are mixed strongly into low-spin states (cf. Fig. 5). The excitation spectra and E2 properties are calculated in a fully microscopic way and are in excellent agreement with the wealth of new spectroscopic data and consistent with a previous phenomenological IBM fit [46]. The theoretical method used in this work is robust and capable of appropriately modeling the coexistence of different shapes. Hence, it allows for a universal description of nuclear shapes and will be applied to other heavy exotic nuclei in the future.

ACKNOWLEDGMENTS

We thank the Tandem accelerator staff at the Wright Nuclear Structure Laboratory, Yale University for their help during the experiment. This work is supported by US DOE under Grant No. DE-FG02-91ER-40609. K.N. acknowledges the support through the JSPS postdoctoral program for research abroad. P.P. is indebted to the Bulgarian Science Fund for the financial support under contract DFNI-E 01/2.

[1] J. L. Wood, K. Heyde, W. Nazarewicz, M. Huyse, and P. van Duppen, Phys. Rep. **215**, 101 (1992).
[2] K. Heyde and J. L. Wood, Rev. Mod. Phys. **83**, 1467 (2011).
[3] G. E. Brown and A. M. Green, Nucl. Phys. **85**, 87 (1966).
[4] A. N. Andreyev *et al.*, Nature (London) **405**, 430 (2000).
[5] W. Nazarewicz, Phys. Lett. B **305**, 195 (1993).
[6] V. Werner *et al.*, Phys. Lett. B **550**, 140 (2002).
[7] G. S. Simpson *et al.*, Phys. Rev. C **74**, 064308 (2006).
[8] P. Cejnar, J. Jolie, and R. F. Casten, Rev. Mod. Phys. **82**, 2155 (2010).
[9] A. Chakraborty *et al.*, Phys. Rev. Lett. **110**, 022504 (2013).
[10] K. Sieja, F. Nowacki, K. Langanke, and G. Martinez-Pinedo, Phys. Rev. C **79**, 064310 (2009).
[11] P. Federman and S. Pittel, Phys. Rev. C **20**, 820 (1979).
[12] G. Rusev *et al.*, Phys. Rev. Lett. **95**, 062501 (2005).
[13] D. Burch, P. Russo, H. Swanson, and G. E. Adelberger, Phys. Lett. B **40**, 357 (1972).
[14] M. Zielinska *et al.*, Nucl. Phys. A **712**, 3 (2002).
[15] F. Iachello and A. Arima, *The Interacting Boson Model* (Cambridge University Press, Cambridge, 1987).
[16] C. W. Beausang *et al.*, Nucl. Instrum. Methods Phys. Res., Sect. A **452**, 431 (2000).
[17] K. S. Krane and R. M. Steffen, Phys. Rev. C **2**, 724 (1970).
[18] K. S. Krane, R. M. Steffen, and R. M. Wheeler, At. Data Nucl. Data Tables **11**, 351 (1973).
[19] I. Wiedenhöver, code CORLEONE, University of Cologne, 1995 (unpublished).
[20] I. Wiedenhöver *et al.*, Phys Rev. C **58**, 721 (1998).
[21] M. E. Rose, Phys Rev. **91**, 610 (1953).
[22] R. J. Casperson, Ph.D. thesis, Yale University, 2009 (unpublished).
[23] B. Sing, Nucl. Data Sheets **98**, 335 (2003).
[24] E. Williams *et al.*, Phys. Rev. C **80**, 054309 (2009).
[25] R. A. Meyer, J. Lin, G. Molnar, B. Fazekas, A. Veres, and M. Sambataro, Phys. Rev. C **29**, 1839 (1984).
[26] W. M. Currie and C. H. Johnson, Nucl. Instrum. Methods **63**, 221 (1968).
[27] L. C. Northcliffe and R. F. Schilling, At. Data Nucl. Data Tables **7**, 233 (1970).
[28] J. F. Ziegler, *Helium Stopping Powers and Ranges in Elemental Matter* (Pergamon Press, New York, 1978).
[29] P. Petkov *et al.*, Nucl. Phys. A **640**, 293 (1998).
[30] M. Bender, P.-H. Heenen, and P.-G. Reinhard, Rev. Mod. Phys. **75**, 121 (2003).

[31] A. Bohr and B. R. Mottelson, *Nuclear Structure* (Benjamin, New York, 1975), Vol. II.
[32] E. Chabanat, P. Bonche, P. Haensel, J. Meyer, and R. Shaeffer, Nucl. Phys. A **627**, 710 (1997).
[33] P. Bonche, H. Flocard, and P.-H. Heenen, Comput. Phys. Commun. **171**, 49 (2005).
[34] T. Otsuka, A. Arima, and F. Iachello, Nucl. Phys. A **309**, 1 (1979).
[35] J. N. Ginocchio and M. W. Kirson, Nucl. Phys. A **350**, 31 (1980).
[36] K. Nomura, N. Shimizu, and T. Otsuka, Phys. Rev. Lett. **101**, 142501 (2008).
[37] K. Nomura, R. Rodríguez-Guzmán, L. M. Robledo, and N. Shimizu, Phys. Rev. C **86**, 034322 (2012).
[38] M. Albers *et al*., Nucl. Phys. A **899**, 1 (2013).
[39] P. D. Duval and B. R. Barrett, Phys. Lett. B **100**, 223 (1981).
[40] A. Kankainen *et al*., J. Phys. G **39**, 093101 (2012).
[41] K. Nomura, N. Shimizu, D. Vretenar, T. Niksić, and T. Otsuka, Phys. Rev. Lett. **108**, 132501 (2012).
[42] P. Paradis, R. Lecomte, S. Landsberger, and S. Monaro, Phys. Rev. C **20**, 1201 (1979).
[43] R. J. Peterson, R. A. Emigh, and R. E. Anderson, Nucl. Phys. A **290**, 155 (1977).
[44] G. M. Ukita, T. Borello-Lewin, L. B. Horodynski-Matsushigue, J. L. M. Duarte, and L. C. Gomes, Phys. Rev. C **64**, 014316 (2001).
[45] J. Barrette, M. Barrette, A. Boutard, R. Haroutunian, G. Lamoureux, and S. Monaro, Phys. Rev. C **6**, 1339 (1972).
[46] M. Sambataro and G. Molnár, Nucl. Phys. A **376**, 201 (1982).
[47] T. Kibédi, T. W. Burrows, M. B. Trzhaskovskaya, P. M. Davidson, and C. W. Nestor, Nucl. Instrum. Methods Phys. Res., Sect. A **589**, 202 (2008).

4.2 Nuclear structure of ^{96,98}Mo: shape coexistence, robustness of boson seniority and mixed symmetry states

4.2.1 Experimental results

To excite low-lying states in ^{96}Mo, an in-beam experiment was performed at the FN-Tandem accelerator of the Institute of Nuclear Physics, University of Cologne. A ^{3}He beam was accelerated to 18 MeV and impinged on a 8 mg/cm^2 ≈96% enriched ^{96}Zr target. The emitted γ rays were detected with the OSIRIS [50] cube coincidence spectrometer, equipped with nine HPGe-detectors in this experiment. Six of them were equipped with Compton suppression shields. During one week of measurement around 1.5 billion coincident $\gamma\gamma$ events were collected. Figure 4.1 shows a total projection of the

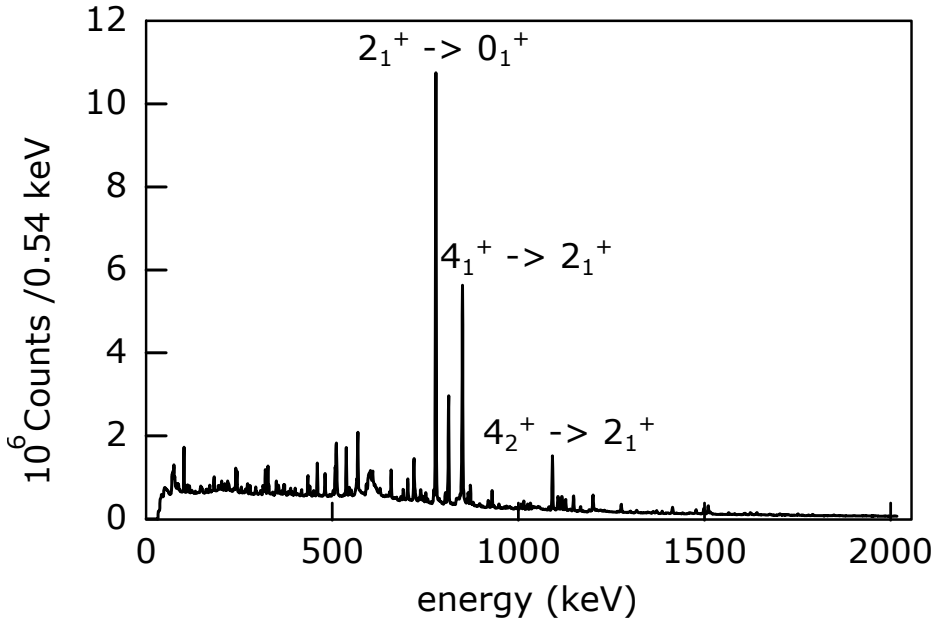

Figure 4.1: Total projection of the $\gamma\gamma$ coincidence data (up to 2000 keV) of the ^{96}Mo experiment. The strongest γ lines are observed at around 800 keV and belong to Yrast band transitions of ^{96}Mo.

$\gamma\gamma$ coincidence data. States with spins J≥8 are weakly populated, and off-Yrast states are observed in this experiment.

To extend the level scheme and verify multipole mixing ratios reported in previous experiments in the neighboring even-even molybdenum isotopes,

another in-beam experiment was performed at the ESTU-Tandem accelerator at Wright Nuclear Structure Lab at Yale University to investigate ^{98}Mo. Using an α beam accelerated to an energy of 16 MeV, γ-transitions emitted after the (α,2n) reaction were detected by 10 Compton-suppressed Clover detectors mounted in the YRAST Ball array [51]. A more detailed discussion of this experiment and partial results are published in Ref. [52]. In this publication, the complete results of ^{98}Mo will be discussed.

An important objective of these experiments was to measure multipole mixing ratios of decay transitions. Especially suited for this purpose are $\gamma\gamma$ correlations in in-beam experiments. For a $J_1 \xrightarrow{E_A,\delta_A} J_2 \xrightarrow{E_B,\delta_B} J_3$ cascade, as described in Refs. [45, 46], different hypotheses for multipole mixing ratios δ can be tested as well as different spins J. In order to perform a $\gamma\gamma$ angular correlation analysis, the data is sorted in correlation group matrices, which account for detector pairs at specific angles $\Theta_{1,2}$ with respect to the beam axis and a relative angle ψ between the planes spanned by the corresponding detectors and the beam axis. For the OSIRIS setup nine different correlation groups are utilized, while the YRAST Ball setup had eleven correlation groups. Since neither of the used targets were pure, the different reaction channels could be used to crosscheck the results of the angular correlation analyses between both experiments.

Figures 4.2 and 4.3 show the angular correlations for the 778-719 keV $\gamma\gamma$ cascade in ^{96}Mo in the OSIRIS and the YRAST Ball setup, respectively, comparing two possible $E2/M1$ mixing ratios measured also in a (n,n$'\gamma$) experiment [53]. ^{96}Mo in the YRAST Ball experiment stems from a side reaction, hence, statistics are lower. Note, the smaller δ_{719} value results from a least-square fit while $\delta_{719} = +1.1$ (1) yields a second minimum in Ref. [53]. The $\delta = +0.40$ (3) assignment is favored in both angular correlations and is given in table 4.1. The fit of the spin hypotheses to data was performed with the computer code CORLEONE [47, 48] For all cases where the angular correlation analysis allows the determination of the multipole mixing ratios, that value is given in tables 4.1 and 4.2. For more details about angular correlation analyses using the OSIRIS or YRAST Ball setups, see Refs. [50] and Ref [52, 54], respectively. Furthermore, in some figures featuring angular correlations, multipole mixing ratios are given with errors derived from a least square fit, otherwise the multipole mixing ratio is fixed to the given value obtained from Nuclear Data Sheets (NDS) [55, 56].

The YRAST Ball experiment allowed for the determination of lifetimes of excited states using the Doppler-Shift Attenuation Method (DSAM) [57]. The line shape is determined by the stopping power of the target material, the α beam energy at 16 MeV, the recoil energy, the mean lifetime τ of the state and

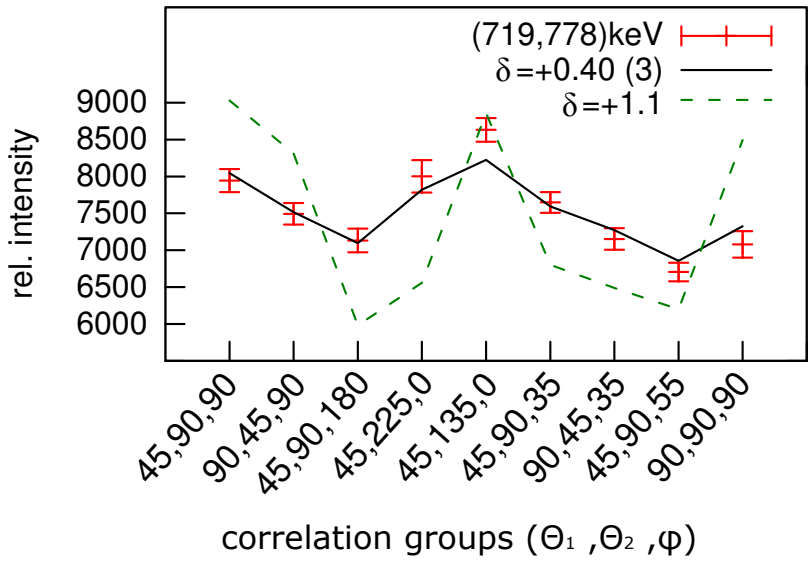

Figure 4.2: Comparison of two spin hypotheses $2 \xrightarrow{719,\delta_{719}} 2 \xrightarrow{778,\delta_{778}=0} 0$ with different $E2/M1$ mixing ratios δ_{719} (black solid and green dashed line) with relative intensities obtained from nine $\gamma\gamma$ angular correlation groups at the OSIRIS setup. The $E2/M1$ mixing ration $\delta = +0.40$ (3) obtained from a least-square fit is favored over $\delta = +1.1$ (1), one of two minima reported in Ref. [53]. The smaller $E2/M1$ mixing ratio $+0.34^{+0.90}_{-0.70}$ reported in Ref. [53] agrees with the present values from both experiments (see also Fig. 4.3).

the angle of the detected γ ray with respect to the beam axis. Figure 4.4 shows the application of line shape analysis. The determined mean lifetime τ =0.25 (5) ps of the state at 2700.86 (36) keV is an effective lifetime, since delayed side feeding cannot be excluded in general in such DSAM experiments. In Ref. [52] another example of the DSAM technique is given and discussed in more detail.

In the following section the complete results obtained from the $\gamma\gamma$ analyzes of both in-beam experiments, ^{96}Mo and ^{98}Mo, are given. First, some states conflicting with previous data in ^{96}Mo and ^{98}Mo are discussed, followed by tables 4.1 and 4.2 with all experimental results.

^{96}Mo:

1497.96 (9) keV, 2^+**.** In addition to the $2_2^+ \xrightarrow{1497} 0_1^+$ and $2_2^+ \xrightarrow{719} 2_1^+$ transitions, a $2_2^+ \xrightarrow{349} 0_2^+$ would be expected at 349.9 keV. Due to multiple transitions with energy close to 350 keV, it is not possible to confirm such a transition, thus a upper limit is given.

1625.92 (9) keV, 2^+**.** For the 847.68 (12) keV transition conflicting $E2/M1$ mix-

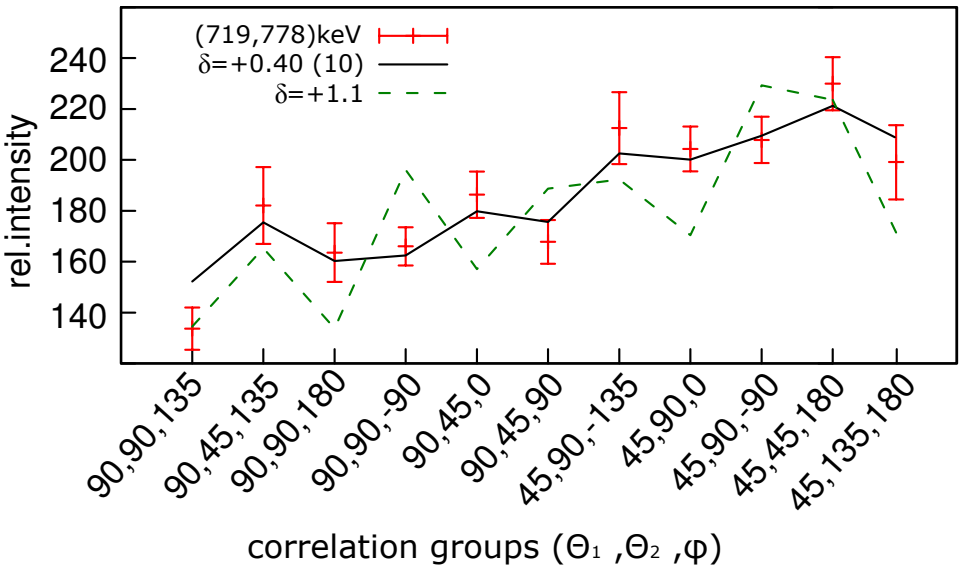

Figure 4.3: Comparison of theoretical angular correlations of the $2 \xrightarrow{719,\delta_{719}} 2 \xrightarrow{778,\delta_{778}=0} 0$ spin hypothesis with relative intensities obtained from eleven correlation groups at the YRAST Ball setup for the 778-719 keV $\gamma\gamma$ coincidence. The $E2/M1$ mixing ratio $\delta = +0.40$ (10) (black solid) obtained from a least square fit is favored over $\delta = +1.1$ (1) (green dashed line) reported in Ref. [53]. For more information see Fig. 4.2.

ing ratios, $\delta(2_2^+ \xrightarrow{847} 2_1^+)$=$-1.05^{+9}_{-10}, -0.6$ (5), -6.9^{+12}_{-21}, were determined, where the first value was measured in a (n,γ) [58] experiment and the latter two originate from Ref. [53]. Evaluation of the angular correlation of the 847-778 $\gamma\gamma$ cascade reveals a rather strong M1 admixture with $\delta_{847} = -0.12$ (5) (see Figure A.1), which agrees with the smaller $E2/M1$ mixing ratio given in Ref. [53]. In order to determine the $E2/M1$ mixing ratio, the two peaks at 847.68 (12) keV and 849.99 (9) ($4_1^+ \rightarrow 2_1^+$) keV have to be discriminated, which is challenging for NaI(Tl) detectors employed in Ref. [58] but possible in this experiment due to the superior resolution of the HPGe detectors. To verify that the nearby 850 keV tranition did not influence our result, the total volume of the doublet at 847 keV and 849 keV was integrated and compared with superposed spin hypotheses $2 \xrightarrow{847,\delta_{847}} 2 \xrightarrow{778,\delta_{778}=0} 0$ and $2 \xrightarrow{849,\delta_{849}=0} 2 \xrightarrow{778,\delta_{778}=0} 0$ (see Figure A.2). Note, since the ratio of the volumes of the 847 keV and the 849 keV peaks is not known in detail, the superposed spin hypotheses were normalized to relative intensities in the correlation groups at the angles (45,90,90) and (45,90,55). The normalization reflects that the major

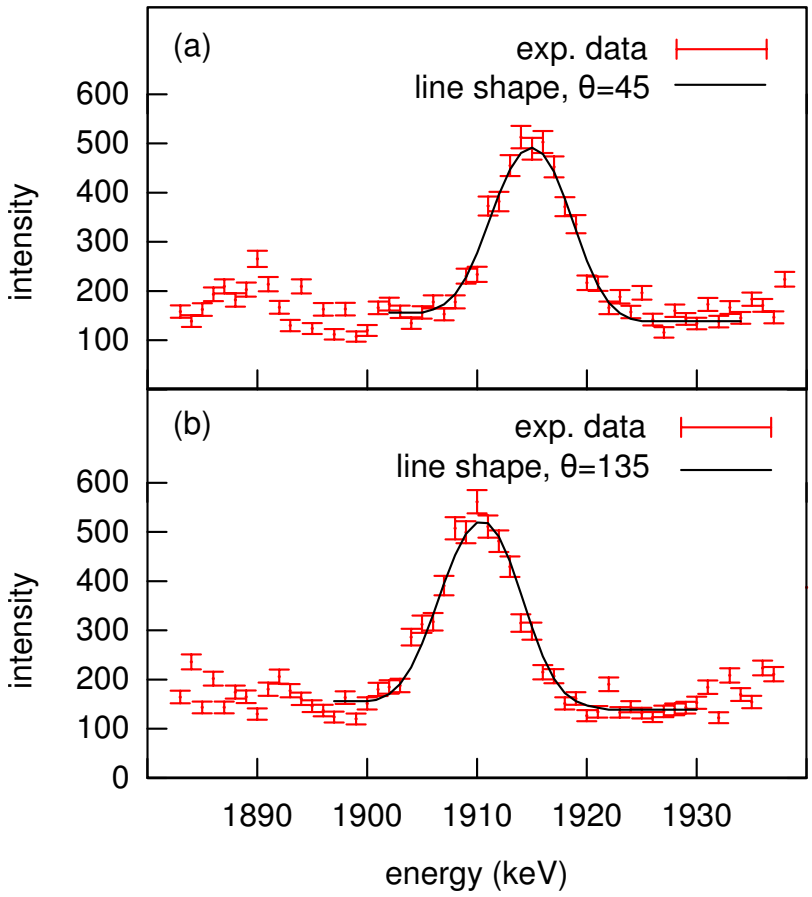

Figure 4.4: Determination of the effective lifetime by analyzing the line shape of the 1913 keV transition in ^{98}Mo depopulating a (2^+) state at 2700 keV using a gate set on the 787 keV transition. Coincidence spectra with a gate set on the 787 keV transition for two different angles are shown. The black solid line represents the simulated line shape at forward (a) and backward (b) angle. The determined effective mean lifetime is $\tau = 0.25$ (5) ps.

component of the superposed angular correlations stems from the 778-849 keV cascade. Nevertheless, only correlation groups with the angles (45,90,180) and (45,225,0) are sensitive to δ_{847} and yield a better fit for $\delta_{847} = -0.12$ than $\delta_{847} = -1.05$. Both figures, A.1 and A.2, together show, that $\delta_{847} = -0.12$ (5) assignment is favored.

1978.43 (10) keV, 3^+**.** The angular correlation analysis of the depopulating transition at 480.55 (9) keV shows that the $E2/M1$ mixing ratio $\delta_{480} = -17.8^{+10.3}_{-64.6}$ is favored (see Figure A.3) to the assignment of $\delta_{480} = -0.12$ (4) reported in Ref. [53]. A rather pure E2 characteristic for the 480 keV transition is also supported by the angular correlation of the 1498-480

keV cascade. On the other hand, for the other depopulating transition at 1200.39 (7) keV a stronger $E2/M1$ mixing with $\delta_{1200} = +0.34(4)$ was determined (see Figure A.4) than in Ref. [53].

2219.46 (9) keV, 4^+. The branching ratios from this work for the transitions depopulating this state mostly agree with values reported in Ref. [53]. However the relative γ intensity of the 241.36 (20) keV transition seems to be overestimated in Ref. [58], which might originate from a doublet with a 241.33 keV transition depopulating a state at 1869.64 (6) keV and cannot be distinguished in the singles spectrum used in Ref. [58]. The coincidence technique employed in this work allows to determine the branching ratio and avoids any contribution of the contaminating 241.33 keV transition.

2594.39 (12) keV, 3^+. The analysis of the branching ratios of the depopulating transitions yields different results than given in [53]. One reason might be that the coincidence technique together with the superior absolute efficiency of the OSIRIS setup allows a better discrimination of the 966 keV and 968 keV peaks compared to the one detector used in Ref. [53].

2818.67 (35) keV, 4^+. The angular correlation analysis of the 1190-849 keV $\gamma\gamma$ cascade suggests a spin for the state with either $J_{2818} = 4, 5, 6$, but the spin assignment $J_{2818} = 5, 6$ can be ruled out due to the depopulating 1320.9 (5) keV transition to the $J^\pi = 2^+$ state reported in Ref. [53], assuming only dipole and quadrupole transitions.

Table 4.1: Results of this work on ^{96}Mo. States discussed in section 4.2.1 are labeled with a sharp sign ($^\#$). Newly observed states are labeled with a asterisk (*) and newly observed transitions with dagger (†). Furthermore, γ intensities I_γ of transitions that are listed in NDS [55] but are not observed due to the sensitivity limit of the detector system or background are labeled with a dash ($-$). If a value is adopted from NDS it is labeled with a double asterisk (**). If a spin assignment of a state due to angular correlation analysis is not unique, those spins are labeled with a double-dagger (‡‡). If an angular correlation analysis is not feasible but selection rules suggest the multipole characteristic of the γ transition, the multipolarity is given in parentheses.

E_{level} (keV)	$J^\pi_{initial}$	τ(ps)	E_γ(keV)	$I_{\gamma,exp}$	δ_{exp}	E_{final}(keV)	J^π_{final}
0.0	0^+	stable					
778.23 (6)	2^+	5.29 (9)**	778.23 (6)	100	E2	0.0	0^+
1147.96 (10)	0^+	88 (12)**	369.73 (8)	100	E2	778.23 (6)	2^+
1497.88 (9)$^\#$	2^+	1.13 (10)**	(349.9)	<2.3	E2	1147.96 (10)	0^+
			719.55 (7)	100	+0.40 (4)	778.23 (6)	2^+
			1497.97 (9)	39.9 (8)	E2	0.0	0^+
1625.92 (9)$^\#$	2^+	>1.30**	128.0 (4)**	<0.9		1497.88 (9)	2^+
			477.61 (25)*	1.7 (4)	E2	1147.96 (10)	0^+
			847.68 (12)	100	-0.12 (5)	778.23 (6)	2^+
			1626.00 (22)	6.4 (17)	E2	0.0	0^+
1628.22 (8)	4^+	1.73 (29)**	849.99 (6)	100	-0.01 (2)	778.23 (6)	2^+
1869.64 (6)	4^+	$9.23^{+40,**}_{-22}$	241.33 (7)	9.0 (5)	$+0.5^{+1.2}_{-0.6}$	1628.22 (8)	4^+

E_{level} (keV)	$J^{\pi}_{initial}$	τ(ps)	E_{γ}(keV)	$I_{\gamma,exp}$	δ_{exp}	E_{final}(keV)	J^{π}_{final}
			(243.6)	< 0.6		1625.92 (9)	2^+
			371.71 (7)	6.3 (6)	-0.05 (6)	1497.88 (9)	2^+
			1091.50 (6)	100	-0.03 (3)	778.23 (6)	2^+
1978.43 (10)$^{\#}$	3^+	>3.30**	108.94 (11)	-		1869.64 (6)	4^+
			349.96 (8)	4.9 (2)	+0.22 (10)	1628.22 (8)	4^+
			352.54 (10)	4.4 (2)	$+3.7^{+15.0}_{-1.8}$	1625.92 (9)	2^+
			480.55 (9)	30.8 (4)	$-17.8^{+10.3}_{-64.6}$	1497.88 (9)	2^+
			1200.39 (7)	100	+0.34 (4)	778.23 (6)	2^+
2095.86 (11)	2^+	0.140 (16)**	(597)	<4.7		1497.88 (9)	2^+
			947.41 (32)	1.8 (5)		1147.96 (10)	0^+
			1317.63 (9)	100	-0.01 (9)	778.23 (6)	2^+
			2095.59 (10)	-		0.0	0^+
2219.46 (9)$^{\#}$	4^+	>0.55**	241.36 (20)	14.7 (8)		1978.43 (10)	3^+
			349.65 (16)	88.5 (37)	+0.09 (13)	1869.64 (6)	4^+
			591.21 (9)	96.7 (39)	+0.84 (23)	1628.22 (8)	4^+
			593.42 (18)	46.0 (35)	-0.05 (10)	1625.92 (9)	2^+
			721.57 (12)	100	+0.04 (5)	1497.88 (9)	2^+
			1441.10 (16)	43.5 (22)	+0.03 (5)	778.23 (6)	2^+
2234.70 (8)	3^-	>0.40**	365.01 (17)	10.0 (7)	-0.10 (20)	1869.64 (6)	4^+
			608.70 (8)	100	-0.09 (12)	1625.92 (9)	2^+
			736.92 (8)	94.0 (38)	+0.03 (5)	1497.88 (9)	2^+
			1456.25 (9)**	-		778.23 (6)	2^+
2426.51 (29)	$2^{+,**}$	$0.27^{+6,**}_{-4}$	447.62 (10)**	-		1978.43 (10)	3^+
			800.27 (10)**	<45.2		1625.92 (9)	2^+
			928.25 (10)**	-		1497.88 (9)	2^+
			1648.00 (28)	100		778.23 (6)	2^+
			2426.28 (10)	-		0.0	0^+
2438.47 (6)	5^+	>0.20**	219.05 (9)	6.4 (9)		2219.46 (9)	4^+
			459.91 (7)	44.4 (29)	+0.05 (13)	1978.43 (10)	3^+
			568.82 (6)	100	-0.15 or -3.6	1869.64 (6)	4^+
			810.18 (36)	16.3 (34)		1628.22 (8)	4^+
2440.80 (10)	6^+	>0.30**	812.58 (6)	100	-0.02 (3)	1628.22 (8)	4^+
2481.28 (10)	$2,3,4^{\ddagger\ddagger}$	>1.46**	611.30 (20)	17.1 (37)		1869.64 (6)	4^+
			853.09 (8)	100		1628.22 (8)	4^+
			983.1 (2)**	-		1497.88 (9)	2^+
			1703.24 (39)	33.9 (79)		778.23 (6)	2^+
2501.69 (23)	$1,2^{\dagger}$	0.139 (19)**	875.61 (10)**	-		1625.92 (9)	2^+
			1003.69 (10)**	-		1497.88 (9)	2^+
			1353.73 (21)	100		1147.96 (10)	0^+
			1723.29 (10)**	-		778.23 (6)	2^+
			2501.84 (10)**	-		0.0	0^+
2540.78 (32)	$(3)^{+,**}$	0.100 (14)**	914.53 (9)**	-		1625.92 (9)	2^+
			1042.62 (9)**	-		1497.88 (9)	2^+
			1762.55 (32)	100		778.23 (6)	2^+
2594.39$^{\#}$ (12)	$3^{+,**}$	$1.15^{+620,**}_{-58}$	374.9 (2)**	-		2219.46 (9)	4^+
			615.66 (23)	73.7 (127)		1978.43 (10)	3^+
			966.38 (31)	36.5 (69)		1628.22 (8)	4^+
			968.37 (19)	100		1625.92 (9)	2^+
			1096.31 (26)	62.7 (122)		1497.88 (9)	2^+
			1816.21 (33)	26.4 (55)		778.23 (6)	2^+
2625.32 (20)	4^+	0.72^{+115**}_{-29}	405.9 (3)	-		2219.46 (9)	4^+
			1847.09 (19)	100		778.23 (6)	2^+
2734.68 (12)	5^+	>0.36**	293.9 (4)**	-		2440.80 (10)	6^+
			864.93 (10)	63.9 (12)	+0.05 (6)	1869.64 (6)	4^+
			1106.59 (7)	100	-0.02 (3)	1628.22 (8)	4^+
			1109.1 (5)**	-		1625.92 (9)	2^+
2736.27 (21)	$3^{+,**}$	$0.175^{+26,**}_{-25}$	1238.50 (27)	75.3 (10.3)		1497.88 (9)	2^+

E_{level} (keV)	$J^{\pi}_{initial}$	τ(ps)	E_{γ}(keV)	$I_{\gamma,exp}$	δ_{exp}	E_{final}(keV)	J^{π}_{final}
			1957.89 (32)	100	+0.14 (25)	778.23 (6)	2^+
2755.31 (33)	$6^{+,**}$	$>0.280^{**}$	314.17 (9)	20.1 (8)	+0.19 (14)	2440.80 (10)	6^+
			316.52 (19)	14.0 (7)		2438.47 (6)	5^+
			535.78 (8)**	-		2438.47 (6)	5^+
			885.4 (2)**	-		1869.64 (6)	4^+
			1127.09 (7)	100	-0.03 (5)	1628.22 (8)	4^+
2806.42 (24)	(1)**	$0.164^{+30,**}_{-26}$	1180.42 (10)**	-		1625.92 (9)	2^+
			1308.39 (10)**	-		1497.88 (9)	2^+
			1658.46 (22)	100		1147.96 (10)	0^+
2818.67 (35)	4^+	$0.085^{+23,**}_{-17}$	1190.45 (34)	100	-0.08 (15)	1628.22 (8)	4^+
			1320.9 (5)**	-		1497.88 (9)	2^+
2875.35 (12)	$6, 7^+$		120.34 (18)	2.9 (6)		2755.31 (33)	$6^{+,**}$
			434.55 (7)	100	+0.12 (7) or +1.8 (2)	2440.80 (10)	6^+
2975.70 (14)	5^+		434.6 (2)**	-		2540.78 (32)	$(3)^{+,**}$
			740.78 (12)	46.0 (57)		2234.70 (8)	3^-
			755.6 (2)**	-		2219.46 (9)	4^+
			997.15 (22)	53.1 (72)	(E2)	1978.43 (10)	3^+
			1347.54 (15)	100	$+1.5^{+4.1}_{-0.9}$	1628.22 (8)	4^+
2978.51 (11)	8^+		223.31 (9)	2.1 (4)		2755.31 (33)	$6^{+,**}$
			537.70 (7)	100		2440.80 (10)	6^+
3014.43 (20)	$5^{(+),*}$		279.53 (9)*	77.7 (35)		2734.68 (12)	5^+
			1386.39 (11)*	100	+0.02 (7)	1628.22 (8)	4^+
3030.83 (12)*			592.43 (10)*	100		2438.47 (6)	5^+
3143.32 (34)*			388.01 (10)*	100		2755.31 (33)	$6^{+,**}$
3370.29 (12)	8^+		391.59 (13)	6.1 (2)	-0.04 (38)	2978.51 (11)	8^+
			929.49 (7)	100	-0.01 (3)	2440.80 (10)	6^+
3445.96 (12)	6^+		1007.49 (10)	100	+0.35 (8)	2438.47 (6)	5^+
3473.14 (10)	7^+		738.39 (7)	78.6 (19)	+0.04 (5)	2734.68 (12)	5^+
			1032.42 (12)	100	-0.02 (4)	2440.80 (10)	6^+
3597.08 (16)			862.40 (10)*	100		2734.68 (12)	5^+
3710.73 (16)*			732.22 (11)	100		2978.51 (11)	8^+
3787.26 (13)	10^+		808.75 (7)	100		2978.51 (11)	8^+
3804.55 (39)*			434.26 (37)*	100		3370.29 (12)	8^+
3916.20 (15)	$7^+, 9^{\ddagger\ddagger}$		545.91 (9)	100		3370.29 (12)	8^+
4533.33 (17)	$9^+, 11^{\ddagger\ddagger}$		746.07 (11)	100		3787.26 (13)	10^+
4795.38 (26)	11^{**}		879.18 (21)	100		3916.20 (15)	$7^+, 9^{\ddagger\ddagger}$

Table 4.2: Results of this work on ^{98}Mo. States discussed in section 4.2.1 are labeled with a sharp sign ($^{\#}$). Newly observed states are labeled with a asterisk (*) and newly observed transitions with dagger (†). Furthermore, γ intensities I_{γ} of transitions that are listed in NDS [56] but are not observed due to the sensitivity limit of the detector system or background are labeled with a dash ($-$). If a value is adopted from NDS it is labeled with a double asterisk (**). If a spin assignment of a state due to angular correlation analysis is not unique, those spins are labeled with a double-dagger (‡‡). If an angular correlation analysis is not feasible but selection rules suggest the multipole characteristic of the γ transition, the multipolarity is given in parentheses.

E_{level} (keV)	$J^{\pi}_{initial}$	τ(ps)	E_{γ}(keV)	$I_{\gamma,exp}$	δ_{exp}	E_{final}(keV)	J^{π}_{final}
^{98}Mo							
734.75 (4)	0^+	31.45 (130)**					
787.26 (15)	2^+	5.08 (9)**	(52.6)	–		734.75 (4)	0^+
			787.26 (15)	100	+0.0	0.0	0^+
1432.18 (12)$^{\#}$	2^+	2.21 (23)**	644.70 (15)	100	+1.67 (25)	787.26 (15)	2^+
			697.10 (46)	5.8 (7)	(E2)	734.75 (4)	0^+
			1432.29 (20)	81.5 (16)	+0.0	0.0	0^+
1509.74 (21)	4^+	3.65 (7)**	(78.0)	–		1509.74 (21)	4^+

E_{level} (keV)	$J^{\pi}_{initial}$	τ(ps)	E_{γ}(keV)	$I_{\gamma,exp}$	δ_{exp}	E_{final}(keV)	J^{π}_{final}
			722.48 (15)	100	+0.02 (3)	787.26 (15)	2^+
1758.32 (12)	2^+	2.05 (8)**	248.5	–		1432.18 (12)	2^+
			326.05 (25)	7.0 (3)	-0.17 (22)	1432.18 (12)	2^+
			971.03 (16)	65.9 (10)	-0.97 (14)	787.26 (15)	2^+
			1023.61 (16)	100	+0.0	734.75 (4)	0^+
			1758.64 (14)	–		0.0	0^+
1962.81 (20)	0^+		530.61 (30)	39.1 (29)	(E2)	1432.18 (12)	2^+
			1175.57 (20)	100	+0.0	787.26 (15)	2^+
2017.36 (16)	3^-	93.8 (101)**	258.96 (26)	22.0 (19)	+0.01 (6)	1758.32 (12)	2^+
			507.8 (2)	–		1509.74 (21)	4^+
			1230.04 (15)	100	-0.04 (7)	787.26 (15)	2^+
			2018.01 (53)	16.2 (17)	(E3)	0.0	0^+
2037.26 (14)	$0^{(+)}$		1250.00 (19)	100	+0.0	787.26 (15)	2^+
2104.66 (15)	3^+		594.65 (12)	–		1509.74 (21)	4^+
			672.50 (17)	78.9 (28)	$+6.7^{+3.4}_{-1.7}$	1432.18 (12)	2^+
			1317.37 (17)	100	$+2.9^{+0.6}_{-0.5}$	787.26 (15)	2^+
2206.74 (26)	2^+	0.30 (2)	448.2 (2)	–		1758.32 (12)	2^+
			1419.48 (22)	100	-0.33 (11)	787.26 (15)	2^+
2223.74 (14)	4^+		206.3 (5)	–		2017.36 (16)	3^-
			465.5 (2)	–		1758.32 (12)	2^+
			713.80 (16)	100	+1.13 (17)	1509.74 (21)	4^+
			791.58 (17)	82.9 (36)	+0.07 (8)	1432.18 (12)	2^+
			1436.68 (25)	23.4 (19)	-0.03 (7)	787.26 (15)	2^+
2333.03 (24)#	$2^{(+)}$	0.50 (17)	900.85 (21)	100	$-0.15^{+0.19}_{-0.20}$	1432.18 (12)	2^+
2333.32 (17)#	4^+		109.48 (44)	10.9 (44)		2223.74 (14)	4^+
			575.06 (10)	–		1758.32 (12)	2^+
			823.33 (16)	77.4 (47)	-0.388 (7)	1509.74 (21)	4^+
			1546.30 (22)	100	-0.04 (4)	787.26 (15)	2^+
2343.26 (26)	6^+	7.50 (29)**	833.52 (15)	100	-0.01 (7)	1509.74 (21)	4^+
2418.52 (29)#	$2^{(+)}$		986.34 (27)	100	+0.01 (7)	1432.18 (12)	2^+
			1631.26 (50)	96.5 (59)		787.26 (15)	2^+
2419.48 (18)#	4^+		195.66 (10)	–		2223.74 (14)	4^+
			314.9 (2)	–		2104.66 (15)	3^+
			402.33 (39)	10.0 (14)	(E1)	2017.36 (16)	3^-
			661.16 (40)	17.8 (13)	+0.09 (10)	1758.32 (12)	2^+
			909.52 (17)	100	-0.64 (10)	1509.74 (21)	4^+
			987.48 (10)	–		1432.81 (12)	2^+
			1632.46 (33)	40.5 (16)	(E2)	787.26 (15)	2^+
2485.47 (21)	3^+		151.9 (2)	–		2333.32 (17)	4^+
			380.05 (43)	21.8 (17)		2104.66 (15)	3^+
			467.0 (9)	–		2104.66 (15)	3^+
			726.83	< 4.6		1758.32 (12)	2^+
			975.25 (32)	35.9 (17)	$-0.89^{+0.62}_{-1.60}$	1509.74 (21)	4^+
			1053.04 (26)	55.2 (27)	$-0.97^{+0.27}_{-0.36}$	1432.18 (12)	2^+
			1698.49 (26)	100	-0.52 (13)	787.26 (15)	2^+
2506.10 (16)#	5^+		86.51 (32)	8.2 (44)		2419.48 (18)	4^+
			162.53 (15)	–		2343.26 (26)	6^+
			172.89 (16)	73.6 (32)	+0.05 (11)	2333.32 (17)	4^+
			282.52 (10)	–		2223.72 (14)	4^+
			299.6 (2)	–		2206.74 (26)	2^+
			996.33 (16)	100	-0.96 (10)	1509.74 (21)	4^+
2525.50 (29)	2^{**}	0.47 (6)	1093.32 (26)	100	+0.01 (17)	1432.18 (12)	2^+
2562.41 (23)	2		544.52 (39)	7.4 (9)		2017.36 (16)	3^-
			803.6 (5)	–		1758.32 (12)	2^+
			1775.37 (23)	100	+0.05 (7)	787.26 (15)	2^+
2572.83 (17)	3		239.2 (2)	–		2333.32 (17)	4^+
			555.07 (35)	47.0 (66)		2017.36 (16)	3^-
			814.46 (26)	49.6 (27)	+0.10 (10)	1758.32 (12)	2^+
			1140.83 (47)	29.1 (34)		1432.18 (12)	2^+

E_{level} (keV)	$J^{\pi}_{initial}$	τ(ps)	E_{γ}(keV)	$I_{\gamma,exp}$	δ_{exp}	E_{final}(keV)	J^{π}_{final}
			1785.90 (24)	100	+0.01 (6)	787.26 (15)	2^+
2574.35 (16)	4^+		350.81 (18)	100	-0.13 (24)	2223.74 (14)	4^+
			557.08 (39)	19.9 (56)	(E1)	2017.36 (16)	3^-
			1064.27 (18)	90.9 (40)	$-2.69^{+0.75}_{-1.47}$	1509.74 (21)	4^+
2612.21 (46)	$0^{(+)}$		1824.95 (44)	100	+0.0	787.26 (15)	2^+
2619.99 (28)	3^+		1187.50 (43)	9.7 (7)	$+0.95^{+0.98}_{-0.50}$	1432.18 (12)	2^+
			1832.93 (33)	100	-0.54 (13)	787.26 (15)	2^+
			1886.3 (7)	–		734.75 (4)	0^+
2620.56 (17)	5^-		603.25 (17)	63.3 (12)	-0.08 (11)	2017.36 (16)	3^-
			1110 .75 (16)	100	-0.05 (10)	1509.74 (21)	4^+
2678.49 (20)	6^+		172.47 (26)	3.6 (5)		2506.10 (16)	5^+
			335.15 (16)	52.8 (8)	-0.01 (10)	2343.26 (26)	6^+
			345.258 (20)	–		2333.32 (17)	4^+
			445.04 (10)	–		2223.74 (14)	4^+
			1168.81 (16)	100	+0.01 (4)	1509.74 (21)	4^+
2700.86 (36)$^{\#}$	$(2^+)^{**}$	0.25 (5)	493.4 (6)	–		2206.74 (26)	2^+
			1913.60 (33)	100	-0.14 (14)	787.26 (15)	2^+
2733.27 (36)$^{\#}$	$(2^+)^{**}$		1946.01 (33)	100	-0.09 (15)	787.26 (15)	2^+
2768.46 (35)	4^+		1981.20 (32)	100	+0.01 (11)	787.26 (15)	2^+
2795.37 (18)	4^-		778.01 (20)†	37.7 (31)	-0.37 (15)	2017.36 (16)	3^-
			1285.63 (16)	100	-0.02 (3)	1509.74 (21)	4^+
2812.72 (42)$^{\#}$	1^+,2^+,$3^{+,\ddagger\ddagger}$		2025.46 (39)†	100	$-4.4^{+2.2}_{-56.7}$	787.26 (15)	2^+
2836.33 (16)	6^+		157.87 (16)	100		2678.49 (20)	6^+
			330.18 (23)	23.3 (56)	-0.24 (6)	2506.10 (16)	5^+
			493.09 (20)	23.0 (56)	-0.29 (15)	2343.26 (26)	6^+
			1326.7	–		1509.74 (21)	4^+
2853.71 (31)	8^+,7+,6^+,$5^{+,\ddagger\ddagger}$		510.45 (16)	100		2343.26 (26)	6^+
2871.00 (43)	2^+,3		2083.74 (40)†	100	+0.06(10) or $-3.7^{+1.5}_{-5.8}$	787.26 (15)	2^+
2896.58 (21)	5^+		791.83 (28)†	100	(E2)	2104.66 (15)	3^+
			1386.84 (19)†	96.0 (35)	$+3.2^{+0.8}_{-0.5}$	1509.74 (21)	4^+
2905.07 (74)	$(4^+)^{**}$	0.22 (2)	2117.81 (72))†	100		787.26 (15)	2^+
2916.29 (47)	(2^+)	0.11^{+9}_{-6}	2129.03 (45)	100	$-0.71^{+0.37}_{-0.57}$	787.26 (15)	2^+
2962.58 (45)	(2^+,3,4^+)		944.39 (44)	18.5 (47)		2017.36 (16)	3^-
			1452.69 (42)	100		1509.74 (21)	4^+
			2176.41 (47)†	82.5 (141)		787.26 (15)	2^+
2976.70 (32)	$(4^{+,\ddagger\ddagger})$		557.1 (4)	–		1419.48 (18)	4^+
			753.19 (14)	–		2223.74 (14)	4^+
		0.64 (33)	1466.96 (24)	100	+0.05 (17)	1509.74 (21)	4^+
			2189.4 (5)			787.26 (15)	2^+
3019.73 (18)	5^-		399.43 (18)	100	+0.06 (15)	2620.56 (17)	5^-
			676.66(26)	33.5 (24)	-0.01 (10)	2343.26 (26)	6^+
			1002.85 (31)	24.4 (10)	+0.03 (5)	2017.36 (16)	3^-
			1510.4	–		1509.74 (21)	4^+
3021.39 (40)	$(5^{-,**})$		688.23 (10)	–		2333.03 (24)	2^+
			797.88 (10)	–		2223.74 (14)	4^+
			815.5 (3)	–		2206.74 (26)	2^+
			917.05 (13)	–		2104.66 (15)	3^+
			1004.31 (10)	–		2017.36 (16)	3^-
			1263.36 (11)	–		1758.32 (12)	2^+
			1511.65 (34)	100		1509.74 (21)	4^+
			1589.62 (10)	–		1432.18 (12)	2^+
			2234.31 (10)	–		787.26 (15)	2^+
3025.93 (33)	5^+		1516.19 (25)†	100	+0.27 (6)	1509.74 (21)	4^+
3050.21 (35)	$(4^+,3^+)^{\ddagger\ddagger}$		544.5 (4)	–		2506.10 (16)	5^+
			631.4 (2)	–		2419.48 (18)	4^+
			717.5 (3)	–		2333.03 (24)	$2^{(+)}$
		0.18 (3)	1540.47 (52)	100	-0.20 (27)	1509.74 (21)	4^+

E_{level} (keV)	$J^{\pi}_{initial}$	τ(ps)	E_{γ}(keV)	$I_{\gamma,exp}$	δ_{exp}	E_{final}(keV)	J^{π}_{final}
			1618.75 (11)	–		1432.18 (12)	2^+
			2263.0 (2)	–		787.26 (15)	2^+
3067.34 (24)	4^-,5		446.78 (17)	100		2620.56 (17)	5^-
3095.74 (19)	7^-		475.23 (17)	100	+0.01 (3)	2620.56 (17)	5^-
			752.41 (16)	81.2 (16)	-0.01 (4)	2343.26 (26)	6^+
3108.99 (21)	$(2^+,4)^{\ddagger\ddagger}$		1091.52 (20)	100	+0.05 (7)	2017.36 (16)	3^-
			1599.50 (33)	24.2 (37)		1509.74 (21)	4^+
3210.45 (34)	$(4+)^{**}$		1193.09 (30)	100		2017.36 (16)	3^-
3228.71 (29)	$(5^+,6^+)^{\ddagger\ddagger}$	0.22 (3)	885.48 (21)	100	+0.67 (12) or +0.07 (16)	2343.26 (26)	6^+
			1718.80 (55)	<23.8		1509.74 (21)	4^+
3271.24 (31)	$(8^+,7^+,6^+)^{\ddagger\ddagger}$		927.95 (17)	100		2343.26 (26)	6^+
3323.12 (21)	$7^{(-)}$		227.37 (18)†	100	-0.08 (10)	3095.74 (19)	7^-
			979.87 (23)†	99.9 (66)	(E1)	2343.26 (26)	6^+
3556.67 (46)		0.24 (7)	1213.41 (38)†			2343.26 (26)	6^+

^{98}Mo:

1432.18 (10) keV, 2^+. For the depopulating 644 keV transition conflicting multipole mixing ratios are reported. A (n,n'γ) experiment [59] measured two competing values, +1.70 (16) and +0.13 (4) (less likely according to the publication). The Coulomb excitation experiment by M.Zielinska et al. [60], however, resulted in a multipole mixing ratio delta of +0.27 (2), and a (n,γ) experiment [61] determined a value of 0.58 (5). The different multipole mixing ratios are tested in the angular correlation analysis shown in figure A.5. A multipole mixing ratio of $\delta_{644} = 1.67$ (25) is favored and is in good agreement with one of the multipole mixing ratios from the previous (n,n'γ) experiments. Note, that in a neutron capture experiment the angular correlation function for a sequence of γ cascades depends only on the angle between the γ rays. In a Coulomb excitation experiment, firstly, the second 2^+ state is much less excited than the first 2^+ state (see figure 1 in M. Zielinska et al. [60]), and secondly, known $E2/M1$ mixing ratios have been used as input (to the GOSIA code), in order to obtain matrix elements in a global fit. The present in-beam experiment avoids all of the above-mentioned problems. The (α, 2n) reaction sufficiently populates non-Yrast 2^+ states of ^{98}Mo. The multi-detector setup and the given beam quantization axis allow to use 11 correlation groups for the angular correlation analysis. Furthermore, a $\delta_{644} = 1.67$ (25) is supported by the angular correlation analysis using the OSIRIS setup ($\delta_{Osiris,644} = 3.2^{+4.6}_{-1.4}$).

2333.03 (24) and 2333.32 (17) keV, $2^{(+)}$ and 4^+. Using $\gamma\gamma$ coincidences of the 172.89 (16) transition which feeds the state at 2333.32 keV, a γ line at 900.85 keV cannot be detected. This agrees with data from a β decay experiment [59], where a depopulating transition at 900.85 keV was not ob-

served with the relative γ intensity reported in Ref. [56]. The 900.85 keV transition also exhibit a Doppler shift in detectors positioned in forward and backward direction which is not observed for the other transitions given in NDS, thus establishing that in the level scheme at 2333 keV in fact two states can be placed as proposed in proton and deuteron inelastic scattering experiments [62]. Summarizing, the 2333.03 and 2333.32 state can be confirmed by independent gates.

2418.52 (29) keV, 2. The two states at 2418.52 (29) keV and 2419.48 (18) keV are difficult to disentangle. But the coincidence spectrum of the observed 86.51 (32) keV transition depopulating the 2506.10 (16) keV state (see discussion of this state) allows to solely observe γ decays from the state at 2419.48 keV, since a transition with an E3 multipole characteristic is unlikely to be observed. From the coincidence spectrum of the 86 keV we can assume that a hypothetical contributions of a 987.48 keV transition depopulating the state at 2419.48 keV to the 986.34 keV transition depopulating the state at 2418.52 keV is negligible.

2419.48 (18) keV, 4^+. In previous (p, t) and β decay experiments [59,63] a spin of 3^- was assigned to the 2419 keV state while in a (pol t,p) reaction [64] the spin 2 was determined for this state. Figure A.6 shows the comparison of the three possible spin hypothesis with data and a spin of 4^+ is favored. The new spin assignment is confirmed by the angular correlation analysis of the $\gamma\gamma$ cascade 661-1023. Note, the (pol t, p) experiment might have observed the state at 2418 keV instead, (see discussion to the 2418 keV state) which revealed a spin of 2.

2485.47 (21) keV, 3^+. The relative intensity of the 726.83 (11) keV transition observed in Ref. [59] cannot be confirmed, as no γ line is observed in $\gamma\gamma$ coincidence spectrum with the 1023 keV transition. At this energy the sensitivity is such that peaks with a relative γ intensity greater than 4.6% with respect to the other depopulating 1698.49 keV transition would be observed.

2506.10 (16) keV, 5^+. The angular correlation analysis of the 722-996 keV $\gamma\gamma$ cascade (see Figure A.7) favors the spin assignment 5^+ for the 2506 keV state and the multipole mixing ratio is δ_{996} =-0.96 (10).

2700.86 (36) keV, (2^+). The angular correlation analysis favors a spin assignment of 2^+ for this state, a spin assignment of 1^+ or 3^+ cannot be fully rejected. The δ_{1913} value given in Table 4.2 is for a presumed spin 2^+ adopted from literature [56]. The $E2/M1$ mixing ratio for other spin hypotheses are $\delta_{1^+\rightarrow 2_1^+} = -0.45$ (10) and $\delta_{3^+\rightarrow 2_1^+} = +0.34$ (9).

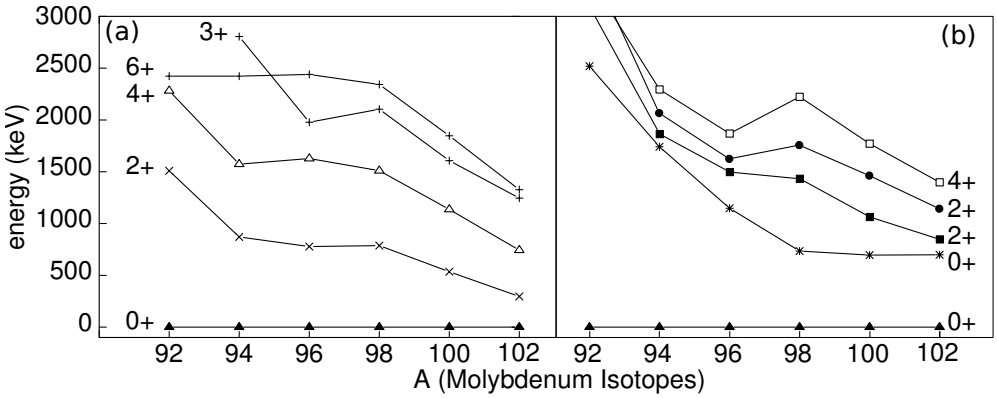

Figure 4.5: Low-lying states observed in experiments [55, 56] are plotted for different molybdenum isotopes. To provide a better overview, the figure is split for states belonging to the Yrast band (a) and off-Yrast states (b).

2733.27 (36) keV, (2^+). The angular correlation analysis yield a possible spin assignment of 2^+, 3^+ for this state. The δ_{1946} value given in Table 4.2 is for a presumed spin 2^+ adopted from the compiled data [56]. If the spin of the 2733 keV state is 3^+, the associated multipole mixing ratio is δ_{1946} =0.27 (10) for the 1946.01 (33) keV transition to the 2^+_1.

2812.72 (42) keV, 1^+,2^+,3^+. The angular correlation analysis does reveal a favored spin assignment for this state. However, if the spin assignment of 2 reported in an inelastic scattering experiment Ref. [62] is correct, the multipole mixing would be δ_{2025} =-4.$4^{2.2}_{-56.7}$.

3095.74 (19) keV, 7^-. The depopulating 752 keV transitions is observed with a smaller branching ratio than reported in Ref [59]. However, in that publication another γ decay with the same energy is observed to depopulate the state at 2976 keV (which was not observed in our data). If the given γ intensities were swapped for both transitions, the newly calculated branching ratio from the β decay experiment would fit to our data. Note, from a previous (α, 2n) experiment [65] the relative intensity was also reported to be much stronger with respect to the depopulating 475.23 keV transition.

4.3 Shape coexistence in ^{96}Mo

4.3.1 Shape coexistence within the IBM-1

Already Sambataro *et al* [66] suggested that configuration mixing is necessary in order to describe excited states in ^{96}Mo. Several observables strongly point towards shape coexistence. The evolution of low-lying states is given in Fig. 4.5. It is striking, that while the excitation energy of the second 0^+ state drops steeply from ^{94}Mo to ^{98}Mo, the states belonging to the Yrast band remain approximately constant. On the other hand, the states shown in Fig. 4.5(b) decrease in energy for ^{96}Mo and show a local maximum for ^{98}Mo. These features together with other observables such as γ transitions depopulating 1^+ states with equal strengths to both 0^+ states [67] in ^{98}Mo are well described by shape coexistence [52, 66] associated with the two minima in Fig. 4.7. To test whether explicit inclusion of shape coexistence can improve the description of ^{96}Mo, IBM-1 calculations were performed using a $2p$-$2h$ intruder configuration due to proton excitations across the Z=40 sub-shell [68]. For ^{98}Mo, in Fig. 5 in Ref. [52] the mixed and unmixed configurations are given and can be associated with a rather vibrational and a γ-soft nuclear shape. As a simple test for the potential influence of configuration mixing, IBM-1 Hamiltonians [15] of the U(5) limit and the O(6) limit was fitted to the corresponding unmixed configurations of ^{98}Mo, as derived in Ref. [52]. The Casimir notation was used for the eigenfunction of two configurations:

$$E = \alpha_I \, n_d + \beta_I \, (\tau(\tau+3)) + \gamma_I \, (J(J+1)) \tag{4.1}$$

$$E = \alpha_{II} \, \sigma(\sigma+4) + \beta_{II} \, (\tau(\tau+3)) + \gamma_{II} \, (J(J+1)) \tag{4.2}$$

where (I) denotes the U(5) limit representing the normal $0p$-$0h$ configuration, and (II) is the O(6) limit representing the intruder $2p$-$2h$ configuration. The U(6) Casimir operators are neglected as they only contribute to binding energy. Consistent with Ref. [52], ^{90}Zr was used as the core, thus the number of bosons are $N = 3$ and $N = 5$ for the normal and intruder configuration, respectively. The parameters obtained from the fit of Eq.s 4.1,4.2 to the unmixed configurations are given in table 4.3. The full Hamiltonian for the configuration mixing is similar to the one given in Eqs. 1.12 and 1.13. The parameters Δ, ω induce the mixing of the configurations and are determined from a fit to the low-lying states in ^{96}Mo. In Fig. 4.6 the calculated level scheme is compared to data obtained in this work. For clarity, not all states between 2000 keV and 2500 keV are shown in the figure, notably the 2^+ state at 2095 keV identified as the one phonon mixed symmetry state in Ref. [53], which cannot be discussed in the

Table 4.3: Parameters of the IBM-1 Hamiltonians in Eqs. 4.1, 4.2 and those responsible for configuration mixing in ^{96}Mo. Furthermore, $\omega = 0.1$ and $\Delta = 0.8$ MeV for the mixing of the configuration.

nucleus	configuration	$\alpha_{I,II}$ (MeV)	$\beta_{I,II}$ (MeV)	$\gamma_{I,II}$ (MeV)
^{96}Mo	normal	1.096	0.025	-0.023
	intruder	-0.10	0.11	-0.02

framework of IBM-1. The mixing of the configurations (on the right hand side of Fig. 4.6) will be discussed in more detail below. The configuration mixing results in a good description of the low-lying 0_2^+ state, while still conserving the $R_{4/2}$ ratio of approximately 2. The assumption, that the O(6) like intruder configuration is located at higher energies, i.e. shifted up by Δ, is essential, otherwise the 2_1^+ would be predicted too low. This agrees with an evolution of the nuclear shapes from deformed (N=60) to spherical (N=52), where ^{94}Mo shows vibrational character (see Fig. 4.7). However, with the used parameters it is not possible to describe the large energy gap between the 0_2^+ and 0_3^+ states of about 1500 MeV. To accommodate for this, the configurations would need to be adjusted to ^{96}Mo. Nevertheless, the overall agreement between the perturbed configuration and the experimental levels is reasonably good (left hand side of Fig. 4.6) and shows the importance of configuration mixing for ^{96}Mo. Beside level energies, transition strengths are important observables to obtain information on the wave function of states. In the IBM-1, the $E2$ operator is defined as

$$\hat{T}^{E2}_{\mu,i} = \epsilon_{i,b}[s^\dagger \times \widetilde{d} + d^\dagger \times \widetilde{s}]^{(2)}_\mu + \chi\, \epsilon_{i,b}[d^\dagger \times \widetilde{d}]^{(2)}_\mu, \tag{4.3}$$

where i denotes the different (normal, intruder) configurations and $\epsilon_{i,b}$ the effective boson charge of the configuration i. The total $E2$ transition operator for the perturbed configuration is defined as

$$\hat{T}^{E2}_\mu = \hat{T}^{E2}_{\mu,\text{normal}} + \hat{T}^{E2}_{\mu,\text{intruder}}. \tag{4.4}$$

The effective boson charge $\epsilon_{\text{normal},b}$ =$\epsilon_{\text{intruder},b}$=0.115 eb was chosen such that the B($E2$) strength of the $2_1^+ \xrightarrow{719} 0_1^+$ is reproduced. The comparison between calculated and observed B($E2$) values are shown in table 4.5 and reveal, that configuration mixing is needed to describe ^{96}Mo. Of major importance is hereby the $0_2^+ \xrightarrow{369} 2_1^+$ transition, as it connects the ground state of the intruder configuration with the first excited 2^+ state. To reproduce the B($E2$) value of 51 (7), which is not possible in a single configuration in the U(5) limit, the two configurations have to mix strongly. As the value is still smaller than the observed value, the mixing strength ω might have to be increased. But overall, the tran-

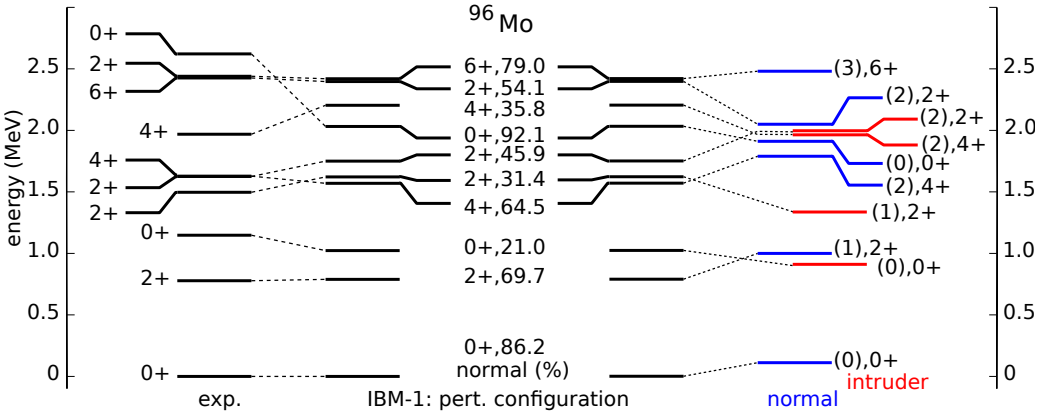

Figure 4.6: Low-energy level scheme of ^{96}Mo. The experimental (left) and the calculated spectra with mixing ("IBM-1: pert. configuration", center) and without mixing (right) labeled with its (τ) quantum number and spin. The number indicated next to spin value (center) represents the fraction of the normal configuration in the wave function of each state.

sition strengths are reproduced reasonably well, except for the $2_3^+ \rightarrow 2_1^+$ and $4_2^+ \rightarrow 4_1^+$ transitions, which are strongly over-predicted.

$M1$ transitions between fully symmetric states are forbidden in the IBM-1 configuration. However, our experiment reveals a significant B($M1$) value of 0.09 (1) μ_N^2 for the $2_2^+ \rightarrow 2_1^+$ transition. The angular correlation analysis for the $2_3^+ \xrightarrow{847} 2_1^+$ transition shows an even stronger $M1$ admixture, although only lower limit of the lifetime of the 2_3^+ state is known. The situation is similar to that in ^{112}Cd [68], where the second and third excited 2^+ states exhibit non negligible $M1$ strengths to the first excited 2^+ state.

Therefore, as shown in the next section, we attempt an IBM-2 calculation with intruders building on results from Ref. [52]. This allows to calculate $M1$ transition strengths, which are important observables for shape coexistence. Even though the PES derived from the EDF calculations for ^{96}Mo (see Fig. 4.7) does not show two distinguishable minima, the minimum is much more shallow than in ^{94}Mo and somewhat elongated in direction of the γ angle.

4.3.2 Shape coexistence within the microscopic IBM-2

In Fig. 4.7 we show the potential energy surfaces for the even-even $^{94-100}$Mo nuclei, calculated by the constrained Hartree-Fock plus BCS method with Skyrme SLy6 interaction. The PESs for ^{96,98,100}Mo nuclei in Figs. 4.7(b,c,d) are exactly the same as those already presented in Ref. [52], but here the PES for ^{94}Mo nucleus (see Fig. 4.7(a)) is also presented for comparison. The PES for

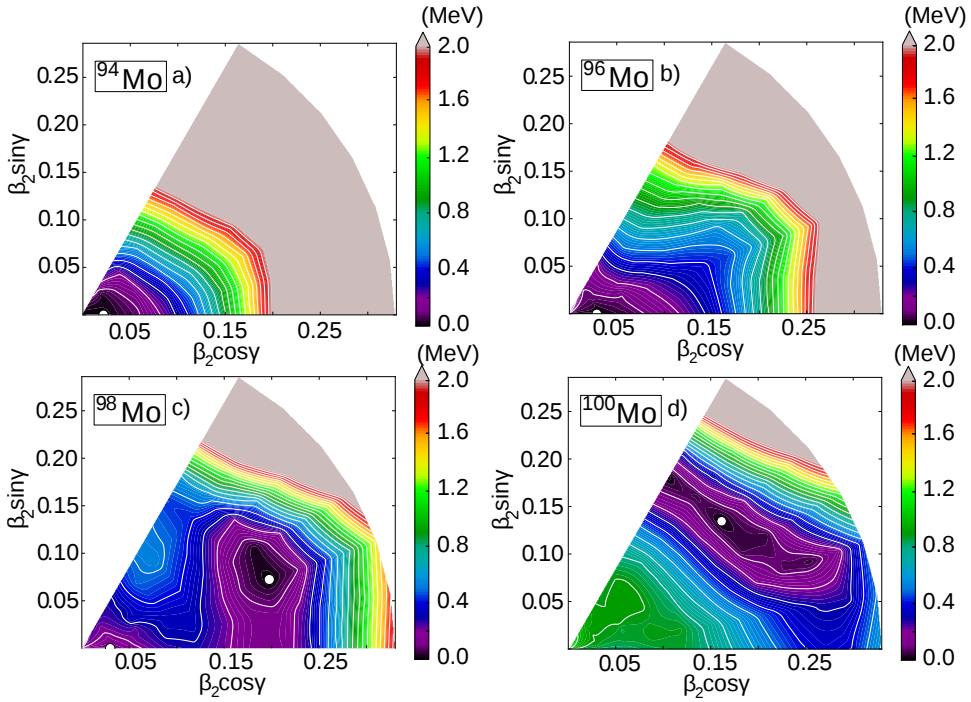

Figure 4.7: Contour plots of the microscopic energy surfaces in (β, γ) plane of $^{94-98}$Mo (a-d). The color code ranges from 0 (mean-field minimum) to 2 MeV, and the minima are identified by the solid white circles. The Skyrme SLy6 functional is used.

^{94}Mo nucleus exhibits almost pure spherical shape, while the topology of the PES for ^{96}Mo is flatter in β direction and is rather elongated in the γ direction. The second minimum is not visible in both nuclei. As discussed in [52], one can see two distinct minima for ^{98}Mo (c), one at spherical and the other at prolate region. Much pronounced deformation characterized by the deep minimum is found for ^{100}Mo (d).

When one tries to describe both shape coexistence and the mixed symmetry states at the same time in the framework of [69], there are two major problems. First, the $\xi_{1,2,3}$ parameters for the Majorana interaction are not determined by simply referring to the PES. One should then consider looking at some other quantities than the PES, which is beyond the scope of the present work. The second problem is that only one minimum is seen in the PES for ^{96}Mo, which makes it difficult to fix the Hamiltonian for the intruder configuration. For these reasons, we end up with taking an empirical way as follows: We take, for the parametrization of the Majorana interactions, the values used in the Sambataro-Molnár's phenomenological IBM-2 calculation, $\xi_1 = \xi_3 = -0.07$

MeV and $\xi_2 = -0.24$ MeV for the normal configuration while $\xi_1 = \xi_2 = \xi_3 = 0$ for the intruder configuration. Concerning the way of invoking the intruder configuration, we use the same intruder Hamiltonian as in [52] without any change but here the energy offset Δ is fixed so that the experimental energy level of the 0_2^+ intruder state is reproduced.

The employed parameters for the IBM-2 plus configuration mixing are presented in Tab. 4.4. Almost the same parameter values are used for the normal configuration of ^{96}Mo and ^{98}Mo, but for the χ_π parameter. The sum $\chi_\pi + \chi_\nu$ measures the γ softness. Indeed, the sum for the normal configuration is smaller in magnitude for the ^{98}Mo than for ^{96}Mo, as confirmed by the PES in Fig. 4.7. The striking difference from the phenomenologically determined parameters used in [66] is that the κ parameter for both configuration in the present study is twice as large in magnitude as in [66].

For completeness, we show in Fig. 4.8 the corresponding IBM-2 energy surfaces for ^{94,96,98}Mo nuclei. A reasonable agreement with the original PESs in Fig. 4.7 is obtained for all nuclei.

Figure 4.9 shows partial level scheme of the ^{96}Mo nucleus, where the IBM-2 calculations with and without the configuration mixing are compared with the experimental data. Apart from the fact that the energy offset Δ is fixed phenomenologically, the IBM-2 configuration mixing calculation reproduces well the experimental level structure. It is evident that the IBM-2 calculation with only a single configuration fails in reproducing the low-lying excited 0^+ state. It implies that the intruder configuration is necessary in this nucleus.

To obtain B(M1) and B(E2) values, the standard operators [15] are used:

$$\hat{T}^{M1} = \sqrt{\frac{3}{4\pi}} \sum\nolimits_{\rho,i} \hat{P}_i g_{\rho,i} \hat{J}_{\rho,i} \hat{P}_i \tag{4.5}$$

The effective charges are set as $e^\pi_{B,1} = e^\nu_{B,1} = 0.106$ eb and $e^\pi_{B,3} = e^\nu_{B,3} = 0.106$ eb are set so that a good overall agreement is obtained for the E2 transition from the 2_1^+ to the ground state. On the other hand, the standard notations for the effective g-factors $g_{\pi,1} = g_{\pi,3} = 1$ and $g_{\nu,1} = g_{\nu,3} = 0$ (in μ_N units) are employed.

The predicted states after mixing are shown in the middle column of Fig. 4.9, where the states drawn in blue represent mixed symmetry states and will be discussed in more detail in section 4.4. Considering, that only Δ is adjusted, compared to the configuration mixing in^{98}Mo, the improvement of the calculated states is remarkable and close to the predicted states from the IBM-1 calculation (cf. Fig. 4.6). $M1$ strengths are predicted for the $2_2^+ \xrightarrow{719} 2_1^+$ and $2_3^+ \xrightarrow{847} 2_1^+$. Since the calculated B($M1$(719))=0.004 value is too small, other changes to both configurations have to be made to accommodate for ^{96}Mo, i.e

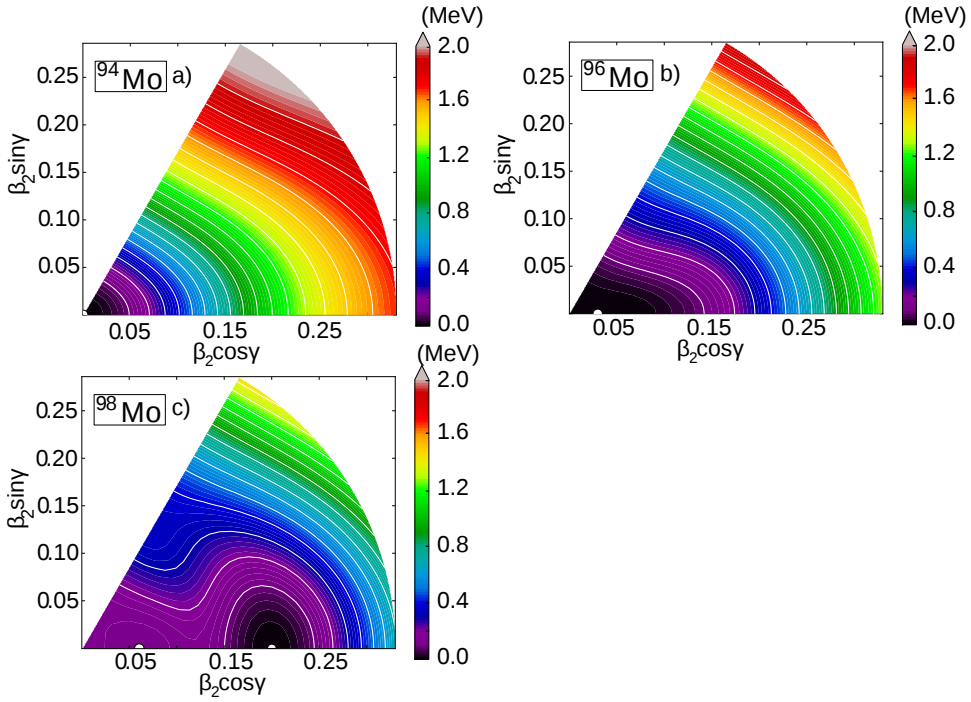

Figure 4.8: The IBM-2 energy surfaces in the (β, γ) plane for the ^{94}Mo (a), ^{96}Mo (b) and ^{98}Mo nuclei. The color code ranges from 0 to 2 MeV, and the minima are identified by the solid white circles.

Table 4.4: Parameters for the IBM-2 configuration mixing given in Eqs. 1.8-1.13. For ^{98}Mo the parameters are derived from the mapped PES (see Fig. 4.8, while parameters used to describe ^{96}Mo is based on ^{98}Mo but adjusted to reproduce the excitation energy of the second 0^+. Note, $\chi_{1,2,3}$ values are adopted from Ref. [66]).

nucleus	configuration	ϵ (MeV)	κ (MeV)	χ_ν (MeV)	χ_π (MeV)
^{96}Mo	normal	1.10	-0.368	-0.90	-0.50
	intruder	0.70	-0.335	-0.85	0.43
^{98}Mo	normal	1.05	-0.368	-0.80	0.18
	intruder	0.70	-0.335	-0.85	0.43
nucleus	configuration	$\xi_1 = \xi_3$	ξ_2	ω	Δ (MeV)
^{96}Mo	normal	-0.07	0.24	0.15	2.00
	intruder	0.00	0.00		
^{98}Mo	normal	-0.07	0.24	0.15	1.715
	intruder	0.00	0.00		

increasing the mixing interaction ω. This is also evident from the comparison of calculated and observed B($E2$) values given in table 4.5. While most values are reproduced, the B($E2$) strength of the $0_2^+ \xrightarrow{369} 2_1^+$ transition is predicted

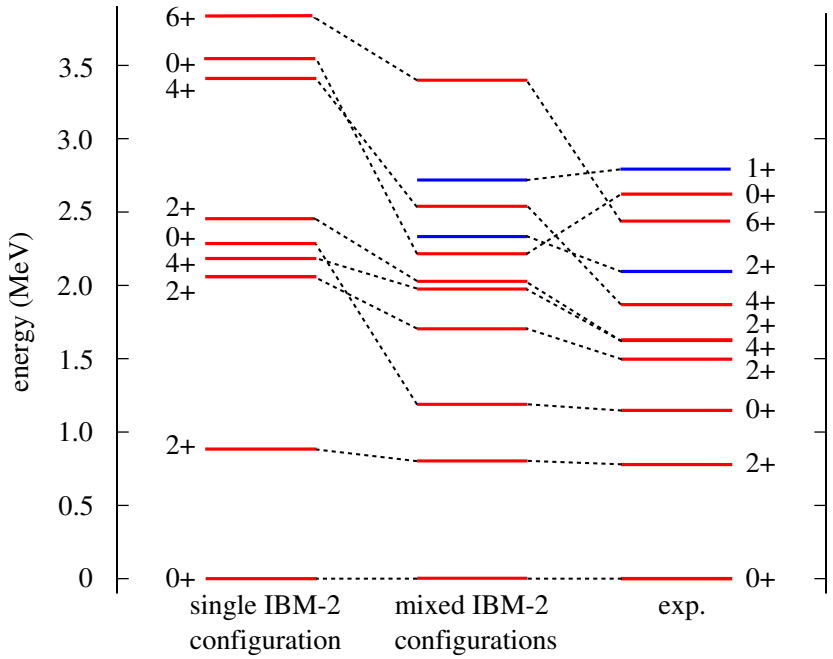

Figure 4.9: Low-energy part of the level scheme for ^{96}Mo, observed in the experiment ^{96}Zr(^{3}He,n)^{96}Mo. The IBM-2 calculations with single (left-hand side) and configuration mixing (middle) are compared with the experimental energy spectra (right-hand side).

too weak. This is due to the almost pure contributions of the intruder and normal configuration to the wave functions of the 0_2^+ and 2_1^+ state(see Fig. 4.11). Specifically the lowest states are rather weakly mixed. In particular a stronger contribution of a vibrational configuration to the second 0^+ state would lead to a stronger $E2$ transition to the first 2^+ state. However, while intricacies of the level scheme or transition strengths are not yet fully described well, this schematic calculation shows that it should be possible to obtain a description of ^{96}Mo in a two-space IBM-2 model.

4.4 Discussion

4.4.1 Conservation of boson seniority

One of the major advantages using the dynamical symmetry limits of the IBM-1 and its extensions is that the dynamical symmetries preserve quantum numbers, thus the Hamiltonian can be written in terms of Casimir operators of a set of nested algebras. This allows the analytical solvability of the quantum system. However, when configuration mixing occurs, an analytical solution is

Table 4.5: Theoretical E2 transition strengths (in W.u.) compared to experimental values given in table 4.1. Transition given in parentages are upper limits for relative intensities and not yet observed. States in bold are predicted to be of intruder nature in theory. The IBM-1 and IBM-2 values are discussed in section 4.3.1 and section 4.3.2, respectively.

E_{level} (keV)	J_I^π	E_γ (keV)	J_F^π	B(E2)$_{\text{IBM-2}}$	B(E2)$_{\text{IBM-1}}$	B(E2)$_{\text{exp}}$
778.23	2_1^+	778.23	0_1^+	20	20	20.7 (4)
1147.96	$\mathbf{0_2^+}$	369.73	2_1^+	6	34	51 (7)
1497.88	$\mathbf{2_2^+}$	(349)	$\mathbf{0_2^+}$	32	30	$<$93.2
		719.55	2_1^+	0	4	13.9 (28)
		1497.97	0_1^+	0.1	0.5	$1.0^{+0.2}_{-0.1}$
1625.92	$\mathbf{2_3^+}$	128.0[1]	$\mathbf{2_2^+}$	11	9	$<$46100
		477.61	$\mathbf{0_2^+}$	0.1	0	$<$18.7
		847.68	2_1^+	8	32	$<$1.4
		1626.00	0_1^+	0.5	0	$<$0.4
1628.22	4_1^+	849.99	2_1^+	25	31	41 (7)
1869.64	$\mathbf{4_2^+}$	241.33	4_1^+	0.4	20	0.2 (1)
		(243.6)	$\mathbf{2_3^+}$	1	5	$<$32
		371.71	$\mathbf{2_2^+}$	37	36	26 (11)
		1091.50	2_1^+	0.4	1	2 (1)

not possible as symmetries are broken. It turns out that in specific cases symmetries are partially preserved. For ^{96}Mo and ^{98}Mo the mixing configurations are associated with a vibrational U(5) like structure and a γ-soft O(6) like structure, so algebraic chains have the same irreps for the nested SO(5) and SO(3) algebras. The algebraic chain for the two limits are defined as

$$\mathrm{U}^{\pi\nu}(6) \supset \left\{ \begin{matrix} \mathrm{U}^{\pi\nu}(5) \\ \mathrm{SO}^{\pi\nu}(6) \end{matrix} \right\} \supset \mathrm{SO}^{\pi\nu}(5) \supset \mathrm{SO}^{\pi\nu}(3), \tag{4.6}$$

Since the mixing term is an O(5) scalar, the boson seniority associated to the O(5) group is preserved. This leads to interesting effects, as states with same spin and close in energy do not mix, if the seniority τ of these states differ [70]. In Fig. 4.6 (on the right hand side) both, the effect of level mixing and the preservation of the τ quantum number is observed. This is best illustrated for the unmixed 2^+ states with $\tau = 1, 2$ between 1.4 and 2.1 MeV. The $\tau = 2$, 2^+ states are in close proximity of 50 keV to each other, thus strongly repelling, leading to an energy gap of 700 keV in the perturbed configuration. If the O(5) quantum number is broken the repelling effect for the intruder 2^+ state would be cushioned by the lower-lying 2^+ state. Since the τ quantum numbers differ, such moderation of the repulsion is not observed. The best way to test the goodness of quantum numbers are transition strengths. As discussed

previously the 2^+ intruder and normal states with $\tau = 2$ heavily contribute to the wave function of the third 2^+ state in the perturbed configuration. The selection rule for $E2$ transitions states that $\Delta\tau > 1$ are forbidden if the O(5) symmetry is not broken. This is observed for the B(E2,$2_3^+ \rightarrow 0_1^+$) values and predicted for the $2_3^+ \rightarrow 0_2^+$ transition.
The used IBM-2 Hamiltonian does not fully conserve $U^{\pi\nu}(6)$ symmetry or the $O^{\pi\nu}(5)$ symmetry. However, since the symmetries are not strongly broken one can still approximately extract the τ and F-spin quantum numbers associated with a given state. This corresponds to the similarities between the calculated B(E2) values (cf. table 4.5) in the U(6) symmetry conserving IBM-1 formalism and the symmetry breaking IBM-2 Hamiltonian. Therefore, the IBM-2 Hamiltonian is treated as approximately O(5) symmetry conserving.

4.4.2 Conservation of F-spin and the one phonon mixed symmetry state

The O(6) like and U(5) like configurations assumed for the unmixed configurations for the IBM-2 calculations not only break the O(5) symmetry rather weakly, but the F-spin quantum number is nearly preserved as well. This can be tested by projecting the wave function of a state onto $F = F_{max}$. While low-lying states associated with fully symmetric states have more than 90% of F_{max}, mixed symmetry states are below 50% of F_{max} (see table 4.6). Similar to unmixed IBM-2 configurations in the O(6) and U(5) limit, the mixed IBM-2 calculation shows a strong $M1$ transition ($> 0.1\ \mu_N^2$) to the first excited 2^+ state.

The occurrence of mixed symmetry in ^{94}Mo has been well established [71]. Also in ^{96}Mo one and two mixed symmetry phonon states are observed [53]. In Fig. 4.10 the $M1$ strengths of 2^+ states to first excited 2^+ are plotted against the level energies of the depopulating transition for $^{94-98}$Mo. In all three cases, a state with a depopulating transition carrying the largest portion of this $M1$ strength is located at about 2100 keV. However, the absolute $M1$ strengths vary strongly. This can be analyzed in terms of configurations mixing. In ^{96}Mo the mixed symmetry states associated to the normal configuration is predicted at 2335 keV, well below the mixed symmetry state associated with the intruder configuration at 3236 keV. This energy gap between the mixed symmetry states is roughly half of the value of the shift Δ between the configurations. Due to the large energy gap the mixed symmetry state is almost unmixed with 86.7% contribution of the normal configuration to the wave function (see the state drawn in blue in Fig. 4.11). The calculated B($E2$) and B($M1$) values agree with the experimental values and confirm the near preservation of F-spin in ^{96}Mo.

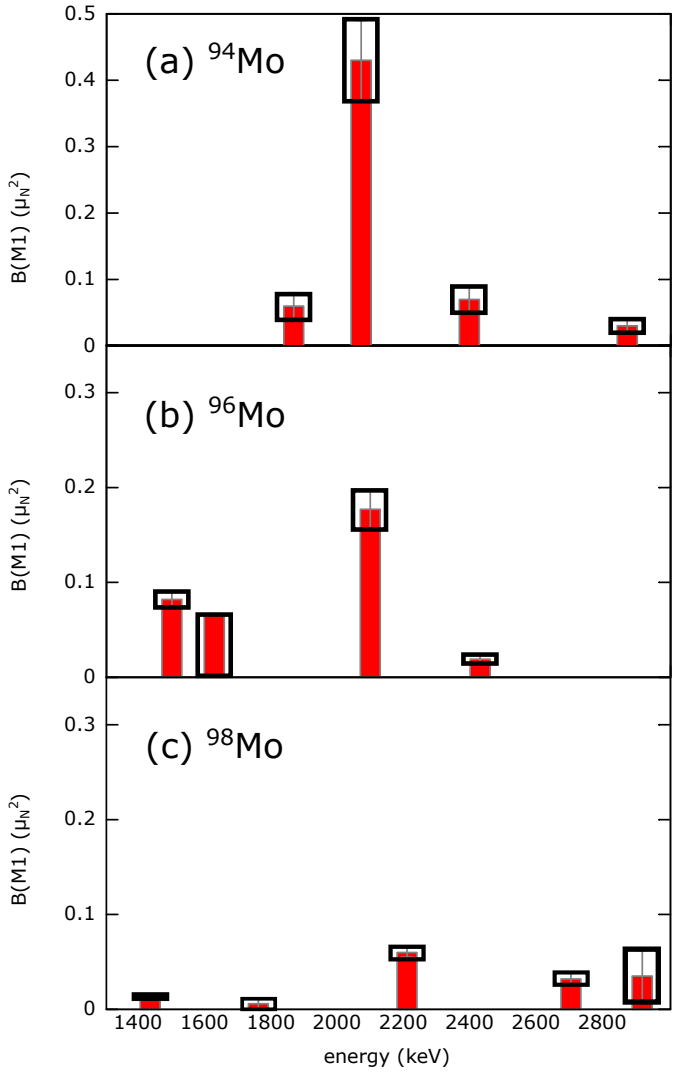

Figure 4.10: $M1$ strength of 2^+ states to the first excited 2^+ is plotted against excitation energy of the depopulating state. Top figure belongs to ^{94}Mo (a) and the values are adopted from Ref. [71], the middle figure (b) belong to ^{96}Mo and the bottom figure (c) belong to ^{98}Mo.

However, in ^{98}Mo the basic conditions are different. The shift Δ between the configurations is much smaller than in the neighboring ^{96}Mo. Thus, the calculation predicts one phonon mixed symmetry states which are strongly mixed (see Fig. 4.12) and comparatively close together. The one phonon mixed symmetry state related to the intruder configuration has a large $M1$ strength to the 2^+_1 state, while the mixed symmetry state related to the normal configuration decays strongly with large $M1$ strength to the 2^+_2 state. Our in-beam experi-

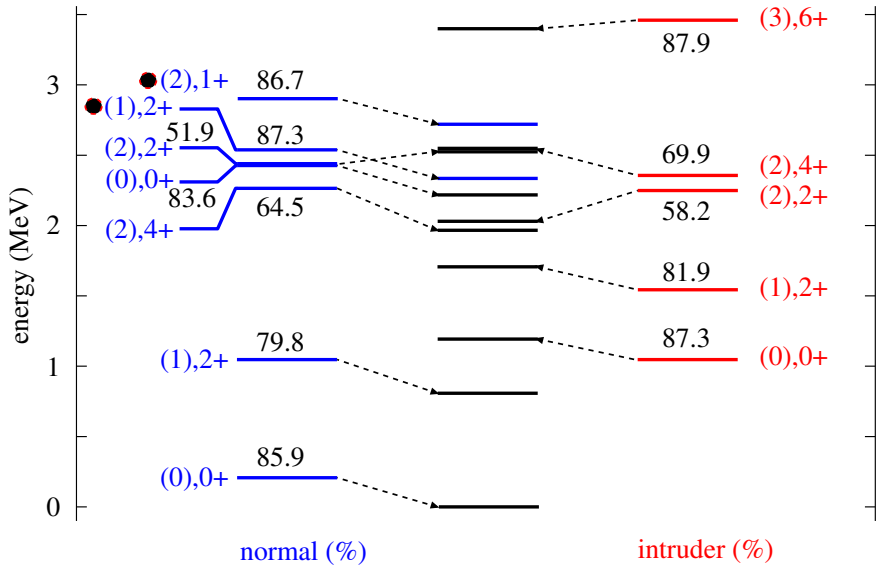

Figure 4.11: Theoretical level scheme for ^{96}Mo is shown with the normal(blue) and intruder (red) configuration. In the parentages the O(5) quantum number τ (seniority) is given. Above or below unmixed state the contribution of a configuration to the wave function of the mixed state is given. Some states in the middle are colored blue, representing mixed symmetry states. Furthermore, next to the quantum numbers of unmixed states associated with the mixed symmetry states, are placed black dots.

ment revealed two candidates for the one phonon mixed symmetry states of either configuration. The candidates are shown in table 4.7, which compares calculated and experimental values. Note, that in some cases the parity could not be determined, as small $M1/E2$ mixing ratios could also indicate E1 transitions. It is assumed that these states are of positive parity, however, as the depopulating transitions only feed positive parity states. In table 4.7, especially the B($M1, 2^+_{ms} \rightarrow 2^+_2$) value is not reproduced. Therefore, either one phonon mixed symmetry state related to the intruder configuration is not populated in the in-beam experiment or it fragments strongly. Still, one can observe fragments of the $M1$ strength to the first excited 2^+ roughly at the expected energy of 2100 keV in ^{98}Mo. The $M1$ strength of the transitions depopulating the one phonon mixed symmetry state related to the normal configuration is reproduced by the sum of the $M1$ strengths of the 900 keV transition and the 1093 keV transition. This suggests, that the mixed symmetry state of the normal configuration fragments into two states at 2333 keV and 2525 keV.

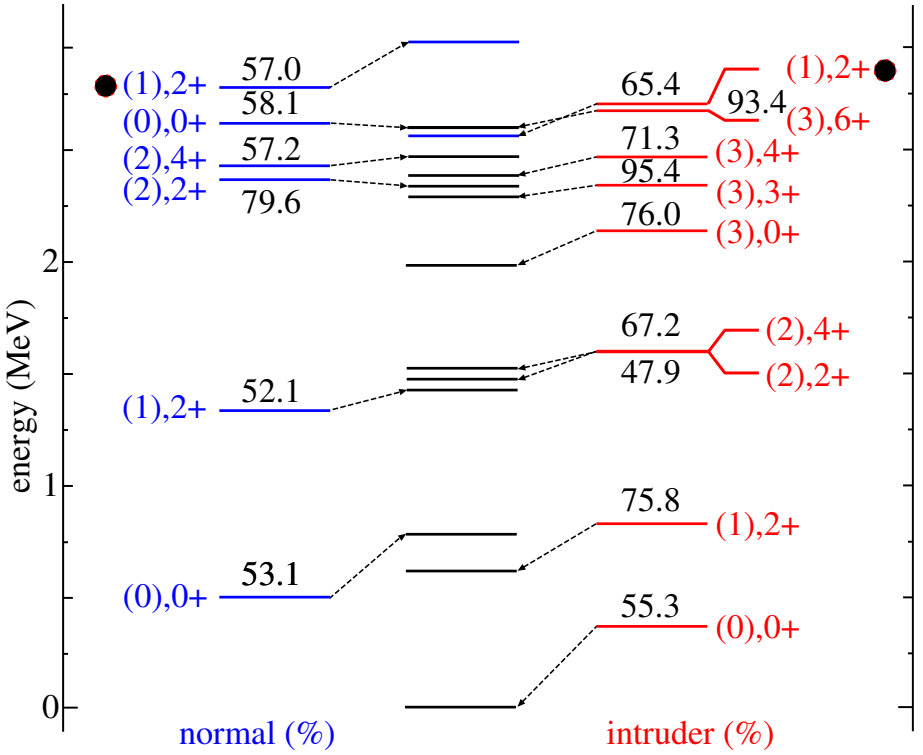

Figure 4.12: Theoretical level scheme for ^{98}Mo is shown with the normal(blue) and intruder (red) configuration. In the parentages the O(5) quantum number τ (seniority) is given. Above or below unmixed state the contribution of a configuration to the wave function of the mixed state is given. Some states in the middle are colored blue, representing mixed symmetry states. Furthermore, next to the quantum numbers of the unmixed state associated with the mixed symmetry state, is placed a black dot.

Table 4.6: Calculated and experimental B($E2$) and B($M1$) values for ^{96}Mo are shown for the one phonon mixed symmetry state and the next 2^+. The lifetimes are adopted from [53] and the remaining values necessary for the calculation of transition strength are taken from this experiment. The exception are those values labeled with ** and are adopted from NDS [55].

$J_i \xrightarrow{E(\text{keV})} J_f$	$F_{max,i}$	% $F_{max,if}$ %	B($M1$)$_{\text{IBM2}}$ (μ_N^2)	B($M1$)$_{exp}$ (μ_N^2)
$2_4^+ \xrightarrow{1317} 2_1^+$	42	98	0.24	0.17 (2)
$2_4^+ \xrightarrow{597} 2_2^+$	42	95	0	<0.08
$2_5^+ \xrightarrow{1648} 2_1^+$	80	98	0.02	$0.0056^{+19,**}_{-21}$
$2_5^+ \xrightarrow{928} 2_2^+$	80	95	0.06	0.0003 (3)**
			B($E2$)$_{\text{IBM2}}$ (W.u.)	B($E2$)$_{exp}$ (W.u.)
$2_4^+ \xrightarrow{2095} 0_1^+$	42	98	0	0.080 (11)
$2_4^+ \xrightarrow{1317} 2_1^+$	42	98	1	0
$2_4^+ \xrightarrow{947} 0_2^+$	42	94	0	5.0^{+22}_{-17}
$2_4^+ \xrightarrow{597} 2_2^+$	42	95	0	0
$2_5^+ \xrightarrow{1648} 2_1^+$	80	98	0	$2.9^{+8,**}_{-9}$
$2_5^+ \xrightarrow{928} 2_2^+$	80	95	21	$6.1^{+11,**}_{-14}$

Table 4.7: Calculated and experimental B($E2$) and B($M1$) values for ^{98}Mo are shown for the one phonon mixed symmetry state and the next 2^+. Values necessary for the calculation of transition strength are taken from this experiment. The B($E2$) values are given in W.u. and B($M1$) values in μ_N^2.

$E_{\text{level},i}$ (keV)	$J_i \xrightarrow{E(\text{keV})} J_f$	$F_{max,i}$ %	$F_{max,f}$ %	B($M1$)$_{\text{IBM2}}$	B($M1$)$_{exp}$
2206	$2_4^+ \xrightarrow{1419} 2_1^+$	54	97	0.27	0.059^{+7}_{-6}
2700	$(2_9^+) \xrightarrow{1913} 2_1^+$				0.031^{+9}_{-6}
2333	$2_5^{(+)} \xrightarrow{900} 2_2^+$	47	94	0.27	0.153^{+87}_{-41}
2525	$2_7^{(+)} \xrightarrow{1093} 2_2^+$				0.094 (12)
				B($E2$)$_{\text{IBM2}}$	B($E2$)$_{exp}$
2206	$2_4^+ \xrightarrow{1419} 2_1^+$	54	97	0	1.7 (2)
2700	$(2_9^+) \xrightarrow{1913} 2_1^+$				0.009 (2)
2333	$2_5^{(+)} \xrightarrow{900} 2_2^+$	47	94	1	1.6^{+9}_{-4}
2525	$2_7^{(+)} \xrightarrow{1093} 2_2^+$				0.0043 (6)

4.5 Brief summary

The data obtained from the ^{96}Mo experiment and the performed IBM-1/IBM-2 calculations are discussed and summarized in more detail in the next chapter 5 together with the results from the previous experiments. Thus, in this section the results are only briefly summed up.
The full results obtained from two in-beam experiments on ^{96}Mo and ^{98}Mo are reported in the table 4.1 and 4.2. The angular correlation analyses allowed to determine spins and multipole mixing ratios, in particular the $E2/M1$ mixing ratio of the $2_3^+ \xrightarrow{847} 2_1^+$ transition. This and the $M1$ strength of the $2_2^+ \xrightarrow{719} 2_1^+$ transition together with the drop of the 0_2^+ state indicates, that configuration mixing might have to be considered. This is emphasized by single configuration IBM-2 calculations which only poorly agree with the observed level energies and are shown in Fig 4.9. IBM-1 configuration mixing calculations (see Fig. 4.11) and IBM-2 configuration mixing were performed as well and show a much better agreement with the obtained data.
The IBM-1 calculation also allowed to investigate whether the O(5) quantum number is conserved. Furthermore, in the framework of IBM-2 using configuration mixing, the one phonon mixed symmetry state was investigated. While the used IBM-2 Hamiltonian with configuration mixing does not fully conserve the F-spin quantum number and seniority, both quantum numbers are only slightly broken. The comparison of $M1$ strength of the transition depopulating the one phonon mixed symmetry state to the first 2^+ state shows (see table 4.6), that the predicted $M1$ strength is only marginally stronger than the observed value. For ^{98}Mo, two one phonon mixed symmetry states for either configuration are predicted (see Fig. 4.12), one exhibiting a strong $M1$ transition to the first excited 2^+ state and another exhibiting a strong $M1$ transition to the second excited 2^+ state. Especially the strength of the latter transition is reproduced by two fragments in the experimental data (see table 4.7).

Chapter 5

Summary and conclusion

In this thesis the even-even molybdenum isotopes in the A=100 mass region and the odd-even gold isotopes in the A=200 mass region were investigated. The aim of this thesis was to test whether the Spin(5)/O(5) quantum numbers are conserved.

For ^{193}Au Interacting Boson Fermion Model calculations were performed including all possible proton orbitals between the Z=50 and Z=82 shell closure. The calculation shows that the dominant contribution to the wave function of the lowest states stems from the $d_{\pi,3/2}$ orbital. At higher excitation energies, contribution from the $s_{\pi,1/2}$ orbital has to be considered. On that basis, IBFM calculations were performed employing the Spin(5) Bose-Fermi symmetry which specifically accounts only for a proton in the $d_{\pi,3/2}$ orbital. Using the newly obtained data from an in-beam experiment, a detailed comparison between the two IBFM calculations and experiment is done. Both IBFM calculations agreed reasonably well with the relative transition strengths observed in the experiment. Considering that in the framework of the Spin(5) Bose-Fermi symmetry only two parameters were used to describe the level energies in ^{193}Au, it was established that the τ_1 quantum number for states belonging to the first three multiplets ($\tau_1 = 1/2, 3/2, 5/2$) is conserved.

Based on the results of Ref. [72], the Interacting Boson Fermion Model using the Spin(5) Bose-Fermi symmetry is extended to other neighboring odd-even gold nuclei. It turns out, that the low-lying states in the odd-even gold nuclei exhibit a rather gradual evolution of levels. This agrees with the prediction of the Nilsson Model (see Fig. 5.1) of a rather smooth behavior of the two most dominant orbitals for the odd-even gold nuclei, the $d_{\pi,3/2}$ and the $s_{\pi,1/2}$ orbitals.

Using the eigenfunction derived from the Bose Fermi symmetry and the simple expression given in Eq. (6) in sect. 3 [74], the smooth evolution of the

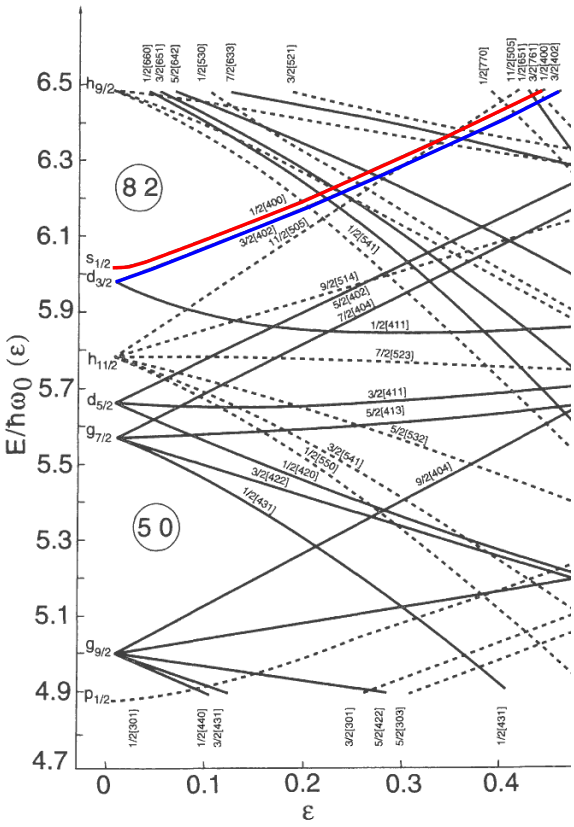

Figure 5.1: (Color online) The energy of the proton Nilsson orbits are plotted against deformation parameter ϵ (similar to β). The evolution of $d_{\pi,3/2}$ orbital (blue curve) and the $s_{\pi,1/2}$ orbital (red curve) with growing deformation is shown. The figure is adopted from Ref. [73].

level energies throughout the odd-even gold isotopes is described well. For this evolution the switch of the ground state from $1/2^+$ to $3/2^+$ from ^{189}Au to ^{191}Au is of major importance and is reproduced in the framework of the Bose-Fermi symmetry. This indicates that it is sufficient to change the ordering of the $\tau_1 = 1/2$ and the $\tau_1 = 3/2$ multiplet, rather than rearrange the ordering of the $d_{\pi,3/2}$ and $s_{\pi,1/2}$ orbitals which are not described by the Nilsson Model. Beside the level energies, other important observables are transition strengths. The agreement between the absolute $E2$ transition strengths and data (see table 4 in sect. 3) throughout the odd-even gold isotopes is rather good, considering that the same effective boson and effective fermion charge was applied for all the investigated nuclei. The notable exception is the strength of the $3/2_2^+ \rightarrow 3/2_1^+$ $E2$ transition. In the Bose-Fermi symmetry this $E2$ transition is forbidden, however, the full IBFM calculation (with the all five proton orbitals) show comparatively more contribution from the $d_{\pi,5/2}$ and $s_{\pi,1/2}$

orbitals to the wave function of the $3/2_2^+$ state than for other members of the $\tau_1 \leq 5/2$ multiplets. Altogether, the good agreement between the predictions of the Spin(5) Bose-Fermi symmetry and available data suggests, that the Spin(5) quantum number is conserved for $^{189-199}$Au.

In contrast to the odd-even gold isotopes, the evolution of the nuclear structure in the even-even molybdenum isotopes is much more complicated. In sect. 4, the different signatures for shape coexistence in ^{98}Mo are discussed, the most obvious one being that the first excited state is a 0^+ state which is rarely observed in even-even nuclei. The description of nuclei exhibiting configuration mixing is particularly challenging as such models require to fix a lot of parameters. Thus, the mapping technique described in sect. 4 [52] is of major importance. This way, one avoids to use the level scheme to adjust parameters, instead the parameters are extracted from a potential energy surface calculated by a microscopic model. The PES of ^{98}Mo calculated using constrained Hartree-Fock plus BCS method with Skyrme SLy6 interaction shows two distinct minima, where one minimum can be associated with a rather vibrational configuration and the second minimum can be associated with a rather γ-soft configuration. Indeed, the mixing of these two configurations reproduces many features observed in the ^{98}Mo. Most importantly, the quadrupole moments and the β deformation of the lowest excited 2^+ states are in good agreement with experimental values. The successful application of the mapping technique motivated to extend this procedure to the neighboring ^{96}Mo, where the microscopic PES shows one distinct minimum (see Fig. 4 in sect. 4 and Ref. [52]).
In sect. 4.2 the result of a single configuration IBM-2 calculation mapped onto the microscopic PES (exhibiting a rather vibrational nuclear shape) is compared with data obtained from an in-beam experiment on ^{96}Mo (cf. Fig. 4.9). The agreement between calculated and observed level energies is poor. Indeed, the obtained data again show characteristics associated with shape coexistence. The angular correlation analyses of the $2_2^+ \xrightarrow{719} 2_1^+$ and $2_3^+ \xrightarrow{847} 2_1^+$ transitions show small $E2/M1$ multipole mixing ratios, which cannot be described in a purely vibrational model. Here, transitions exhibiting $M1$ characteristics are forbidden. Such transitions between the low-lying 2^+ states are found in the ^{112}Cd as well, where shape coexistence was observed. Another indication of configuration mixing is the drop of the level energy of the second 0^+ from ^{94}Mo to ^{96}Mo (see Fig. 4.5).
Thus, based on the unmixed configurations of the calculations for ^{98}Mo, two IBM-1 configurations, one in the U(5) limit and one in the O(6) limit, were derived. These configurations were mixed such, that the level ener-

gies in ^{96}Mo were reproduced. The schematic calculations show a much enhanced agreement with the data. Particularly, the calculations show that the $E2$ strength of the $0_2^+ \xrightarrow{947} 2_1^+$ transition depends on the strength of the configuration mixing. Since the IBM-1 calculations were specifically carried out for a vibrational and a γ-soft configuration, the O(5) quantum numbers are preserved and discussed for selected transitions obeying $E2$ selection rules associated with τ quantum numbers. Another schematic calculation of configuration mixing was carried out for ^{96}Mo, this time using the IBM-2 formalism. The same parameters as those used for the calculations in ^{98}Mo [52] were adopted. Only the parameter Δ, which controls the shift between the two configurations was varied such that the second 0^+ in ^{96}Mo is reproduced. While this is not sufficient to fully reproduce transition strengths, the concept of configuration mixing seems to be required to describe the low-lying states in ^{96}Mo. For example, due to configuration mixing, $M1$ strengths are predicted between the lowest 2^+ states and correspond to experimental observations. Also, the PES of the IBM-2 calculation shows remarkable agreement with the microscopic PES. Furthermore, the agreement of the $M1$ strength from the mixed symmetry state to the first excited 2^+ state suggests that F-spin and O(5) quantum numbers are approximately conserved.

Appendix A

A.1 $\gamma\gamma$ angular correlation analysis

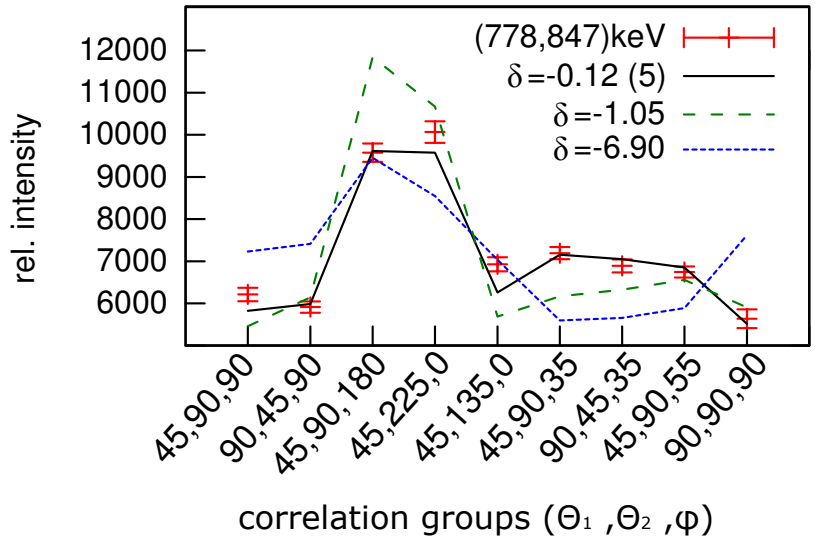

Figure A.1: Comparison of theoretical angular correlations with different spin hypotheses (black solid, green dashed line and blue dashed line) with relative intensities obtained from eleven correlation groups at the OSIRIS setup for the 778-847 keV $\gamma\gamma$ coincidence. The multipole mixing ration $\delta = -0.12(5)$ is favored. See text in sect. 4.2 for more detail.

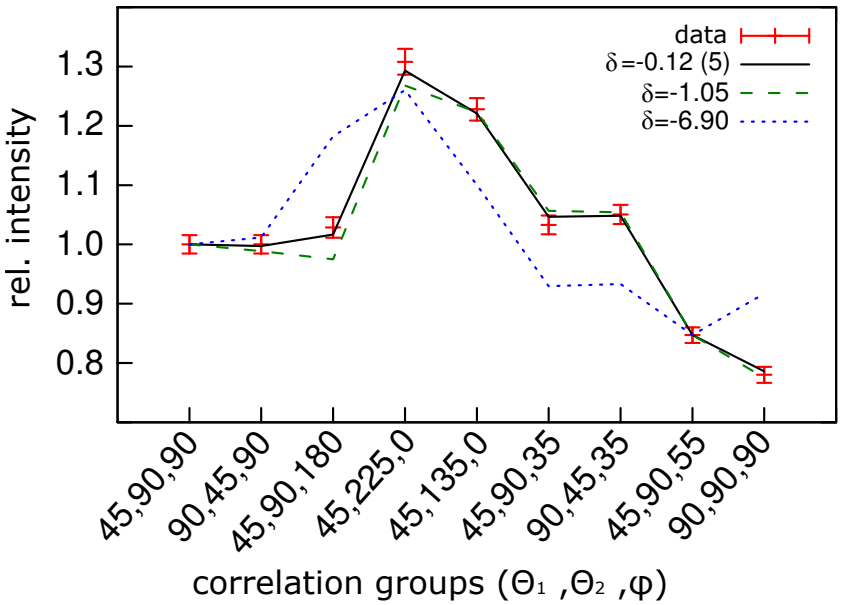

Figure A.2: The integrated volumes of the 847 and 849 keV γ lines in coincidence with the 778 keV transition in the correlation groups are compared to superposed theoretical spin hypotheses (see discussion of the state at 1625 keV in the text 4.2.1 for details).

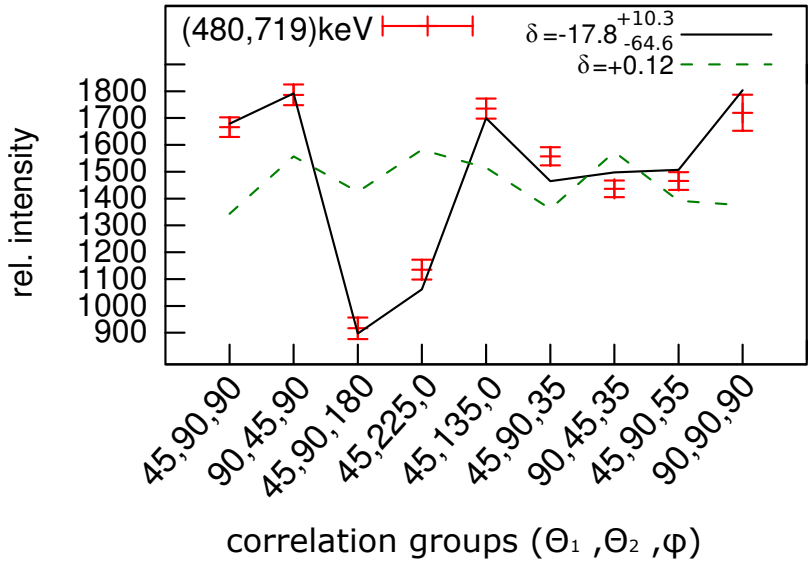

Figure A.3: The spin hypothesis $3 \xrightarrow{480,\delta_{480}} 2 \xrightarrow{719,\delta_{719}=-0.12} 2$ is compared to relative intensities obtained from nine correlation groups at the OSIRIS setup for the 719-480 keV $\gamma\gamma$ coincidences. The multipole mixing ratio $\delta_{480} = -17.8^{+10.3}_{-64.6}$ (black solid) obtained from a least-square fit is favored to $\delta_{480} = -0.12$ (4) (green dashed line) reported in Ref. [53].

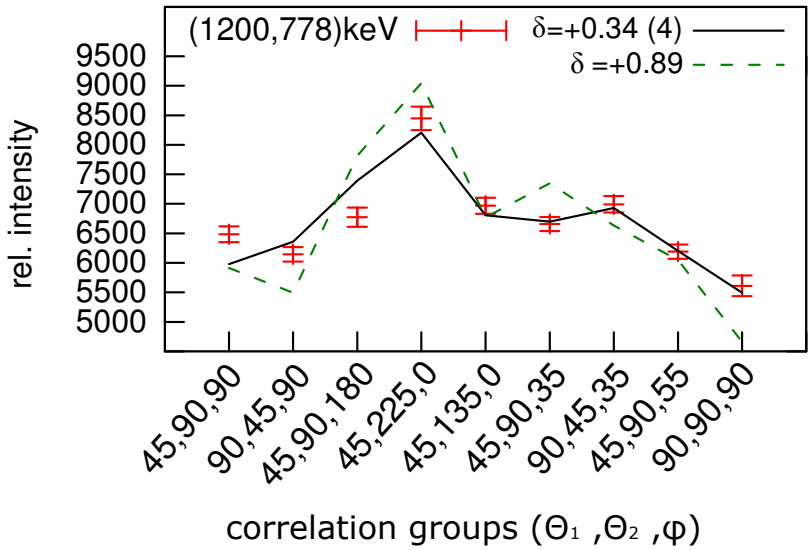

Figure A.4: Comparison of theoretical angular correlations $3 \xrightarrow{1200,\delta_{1200}} 2 \xrightarrow{778,\delta_{778}=+0.0} 2$ with relative intensities obtained from nine correlation groups at the OSIRIS setup. The multipole mixing ratio $\delta_{1200} = 0.34$ (4) (black solid line) is favored to the $E2/M1$ mixing ratio $\delta_{1200} = 0.89$ (10) reported in Ref. [53].

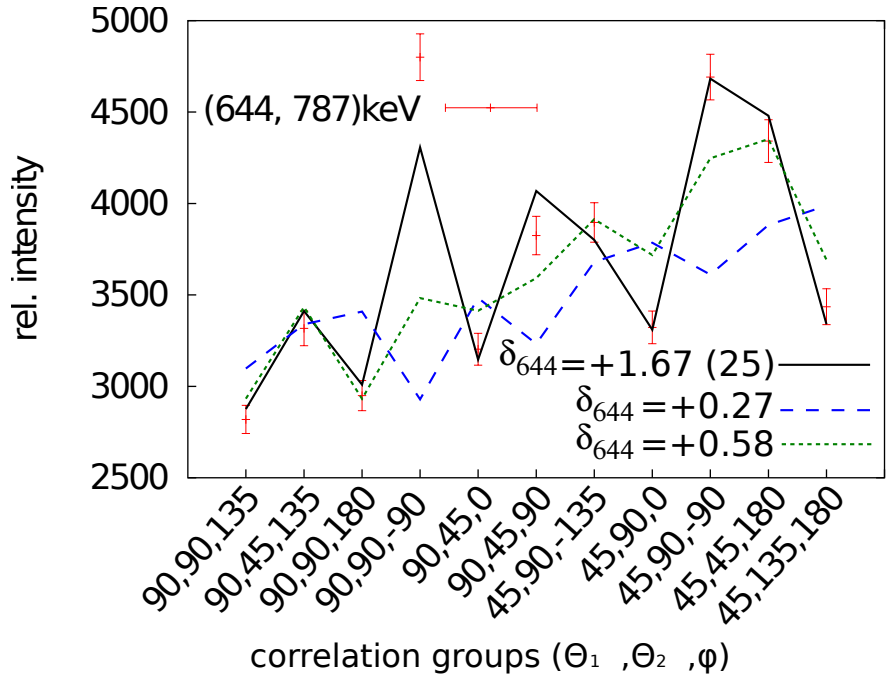

Figure A.5: The spin hypothesis $2 \xrightarrow{644,\delta_{644}} 2 \xrightarrow{787,\delta_{787}=+0.0} 0$ is compared to relative intensities obtained from eleven correlation groups at the YRAST Ball setup. The multipole mixing ratio $\delta_{644} = +1.67\ (25)$ (black solid) obtained from a least-square fit is favored to $\delta_{644} = +0.27\ (2)$ (blue dashed line) reported in Ref. [60] and $\delta_{644} = +0.58\ (5)$ (green dashed line) reported in Ref. [61].

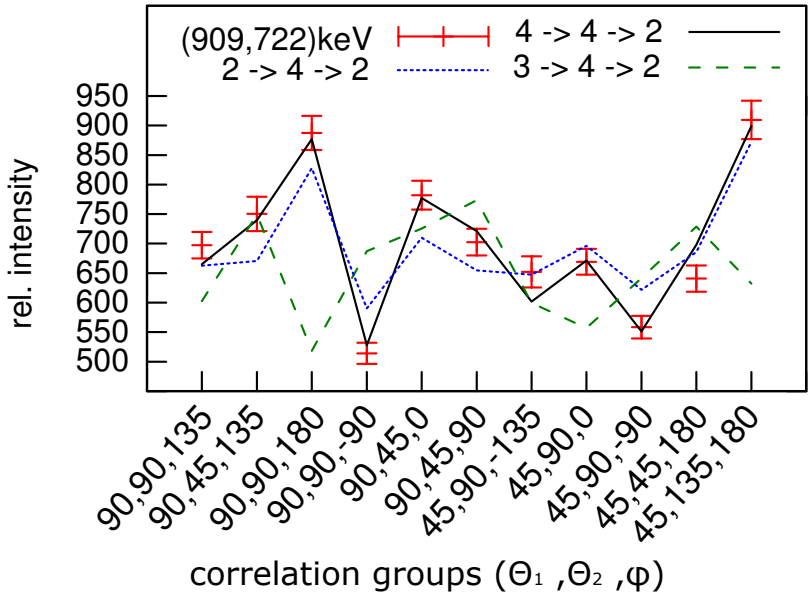

Figure A.6: Three different spin hypotheses (black solid and green dashed line, and blue dashed line) were tested with data obtained at the Yrast Ball setup for the 722-909 keV $\gamma\gamma$ cascade. A spin assignment of 4^+ with $E2/M1$ mixing ratio $\delta_{909} = -0.64$ (10) is favored.

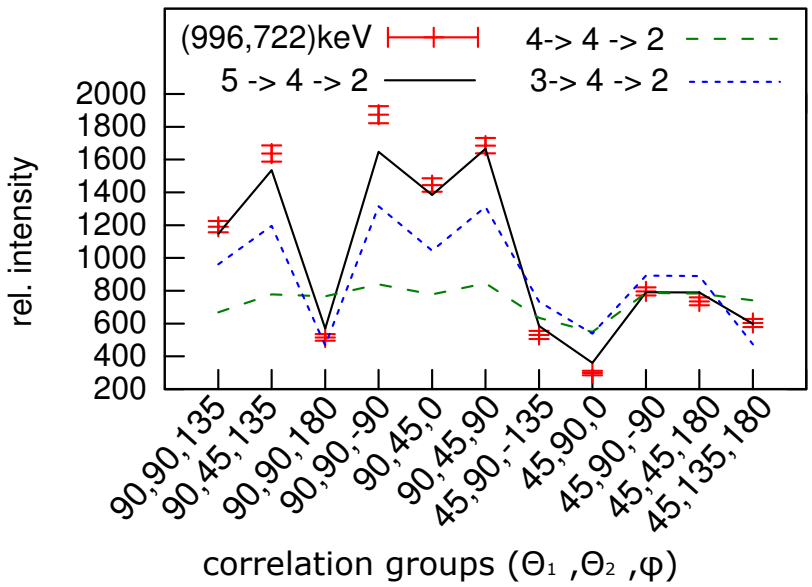

Figure A.7: Three different different spin hypotheses (black solid and green dashed line, and blue dashed line) were tested with data obtained at the Yrast Ball setup for the 722-909 keV $\gamma\gamma$ cascade. A spin assignment of 5^+ with the multipole mixing ratio $\delta = -0.96$ (10) is favored.

List of Figures

List of Tables

Bibliography

[1] T. Lee, *Particle Physics and Introduction to Field Theory*. Chur, Switzerland: Harwood Acadamic Publishers GmbH, 1981.

[2] E. Noether, "Invariante Variationsprobleme," *Nachr. D. König. Gesellsch. D. Wiss. Zu Göttingen*, pp. 235–257, 1918.

[3] P. Ehrenfest, "Bemerkung über die angenäherte Gültigkeit der klassischen Mechanik innerhalb der Quantenmechanik," *Zeitschrift für Physik*, vol. 45, no. 7-8, pp. 455–457, 1927.

[4] G. Sterman, *An Introduction to Quantum Field Theory*. Cambridge, UK: Cambridge University Press, 1993.

[5] I. Joliot-Curie and F. Joliot, "The Emission of High energy Photons from Hydrogenous Substances Irradiated with Very Penetrating Alpha Rays," *Comptes Rendus*, vol. 194, p. 273, 1932.

[6] J. Chadwick, "Possible Existence of a Neutron," *Nature*, vol. 129, p. 312, 1932.

[7] W. Heisenberg, "Über den Bau der Atomkern," *Zeitschrift für Physik*, vol. 77, no. 1-2, pp. 1–11, 1932.

[8] A. Frank, J. Jolie, and P. V. Isacker, *Symmetries in Atomic Nuclei*. Springer, 2009.

[9] A. Frank and P. V. Isacker, *Algebraic Methods in Molelcular & Nuclear Structure Physics*. John Wiley & Sons, 1994.

[10] D.Dubbers and H.-J. Stöckmann, *Quantum Physics: The Bottom-Up Approach*. Springer, 1993.

[11] F. Ajzenberg-Selove, "Energy levels of light nuclei A = 11–12 ," *Nuclear Physics A*, vol. 433, no. 1, pp. 1 – 157, 1985.

[12] E.P.Wigner, "Proceedings of the Robert A Welch Foundation Conferences on Chemical Research. I The Structure of the Nucleus," 1957.

[13] K.Baum *et al.*, "Masses of ^{32}Ar and ^{33}Ar for Fundamental Tests," *Phys. Rev. Lett.*, vol. 91, p. 260801, 2003.

[14] K.Baum, "High-accuracy mass spectrometry with stored ions," *Phys. Reports*, vol. 425, p. 1, 2006.

[15] F. Iachello and A. Arima, *The Interacting Boson Model*. Cambridge University Press, Cambridge, 1987.

[16] A. Arima and F. Iachello, "Interacting Boson Model of Collective Nuclear States I. The Vibrational Limit," *Ann. Phys*, vol. 99, pp. 253–317, 1976.

[17] A. Arima and F. Iachello, "Interacting Boson Model of Collective Nuclear States II. The Rotational Limit," *Ann. Phys*, vol. 111, pp. 201–238, 1978.

[18] A. Arima and F. Iachello, "Interacting Boson Model of Collective Nuclear States IV. The $O(6)$ Limit," *Ann. Phys*, vol. 123, pp. 468–492, 1979.

[19] M.Göppert-Mayer, "Nuclear configurations in the spin-orbit coupling model. I. Empirical Evidence," *Phys. Rev.*, vol. 78, p. 16, 1950.

[20] M.Göppert-Mayer, "Nuclear configurations in the spin-orbit coupling model. II. Theoretical Considerations," *Phys. Rev.*, vol. 78, p. 22, 1950.

[21] O.Haxel, H.E.Suess, and J.H.D.Jensen, "Zur Interpretation der ausgezeichneten Nukleonenzahlen im Bau des Atomkerns," *Phys. Rev.*, vol. 75, p. 1766, 1949.

[22] A.Bohr and B.R.Mottelson, *Nuclear Structure Volume II*. W.A Benjamin Inc. Massachusetts, 1975.

[23] G. Gneuss and W. Greiner, "Collective potential energy surfaces and nuclear structure ," *Nuclear Physics A*, vol. 171, no. 3, pp. 449 – 479, 1971.

[24] L. Cooper, "Bound Electron Pairs in a Degenerate Fermi Gas," *Phys. Rev.*, vol. 104, p. 1189, 1956.

[25] L. Cooper, "Microscopic Theory of Superconductivity," *Phys. Rev.*, vol. 106, p. 162, 1957.

[26] F. Iachello and P. V. Isacker, *The Interacting Boson-Fermion Model*. Cambridge University Press, Cambridge, 1991.

[27] N. Pietralla, P. von Brentano, and A. F. Lisetskiy, "Experiments on multiphonon states with proton neutron mixed symmetry in vibrational nuclei," *Prog. Part. Nucl. Phys.*, vol. 60, p. 225, 2013.

[28] A. Richter, "Probing the nuclear magnetic dipole response with electrons, photons and hadrons ," *Progress in Particle and Nuclear Physics*, vol. 34, no. 0, pp. 261 – 284, 1995. Electromagnetic Probes and the Structure Hadrons and Nuclei.

[29] R. Mohan, M. Danos, and L. C. Biedenharn, "Three-Fluid Hydrodynamical Model of Nuclei," *Phys. Rev. C*, vol. 3, pp. 1740–1749, May 1971.

[30] D. Savran, T. Aumann, and A. Zilges, "Experimental studies of the Pygmy Dipole Resonance ," *Progress in Particle and Nuclear Physics*, vol. 70, no. 0, pp. 210 – 245, 2013.

[31] J. Wood, K. Heyde, W. Nazarewicz, M. Huyse, and P. van Duppen, "Coexistence in even-mass nuclei ," *Physics Reports*, vol. 215, no. 3–4, pp. 101 – 201, 1992.

[32] K. Heyde and J. L. Wood, "Shape coexistence in atomic nuclei," *Rev. Mod. Phys.*, vol. 83, pp. 1467–1521, Nov 2011.

[33] V. Werner, D. Belic, P. von Brentano, C. Fransen, A. Gade, H. von Garrel, J. Jolie, U. Kneissl, C. Kohstall, A. Linnemann, A. Lisetskiy, N. Pietralla, H. Pitz, M. Scheck, K.-H. Speidel, F. Stedile, and S. Yates, "Proton–neutron structure of the N=52 nucleus ^{92}Zr ," *Physics Letters B*, vol. 550, no. 3–4, pp. 140 – 146, 2002.

[34] G. S. Simpson, J. A. Pinston, D. Balabanski, J. Genevey, G. Georgiev, J. Jolie, D. S. Judson, R. Orlandi, A. Scherillo, I. Tsekhanovich, W. Urban, and N. Warr, "High-spin mus isomer in ^{98}Zr," *Phys. Rev. C*, vol. 74, p. 064308, Dec 2006.

[35] A. Chakraborty, E. E. Peters, B. P. Crider, C. Andreoiu, P. C. Bender, D. S. Cross, G. A. Demand, A. B. Garnsworthy, P. E. Garrett, G. Hackman, B. Hadinia, S. Ketelhut, A. Kumar, K. G. Leach, M. T. McEllistrem, J. Pore, F. M. Prados-Estévez, E. T. Rand, B. Singh, E. R. Tardiff, Z.-M. Wang, J. L. Wood, and S. W. Yates, "Collective Structure in ^{94}Zr and Subshell Effects in Shape Coexistence," *Phys. Rev. Lett.*, vol. 110, p. 022504, Jan 2013.

[36] W. Urban, M. Jentschel, R. F. Casten, J. Jolie, C. Bernards, B. Maerkisch, T. Materna, P. Mutti, L. Prochniak, T. Rzkaca-Urban, G. S. Simpson,

V. Werner, and S. Ahmed, "0+2 band in ^{102}Ru and the evolution of nuclear deformation in Ru isotopes," *Phys. Rev. C*, vol. 87, p. 031304, Mar 2013.

[37] K. Nomura, N. Shimizu, and T. Otsuka, "Mean-Field Derivation of the Interacting Boson Model Hamiltonian and Exotic Nuclei ," *Phys. Rev. Lett.*, vol. 101, p. 142501, Sep 2008.

[38] J. Ginocchio and M. Kirson, "An intrinsic state for the interacting boson model and its relationship to the Bohr-Mottelson model ," *Nuclear Physics A*, vol. 350, no. 1–2, pp. 31 – 60, 1980.

[39] K. Nomura, N. Shimizu, and T. Otsuka, "Formulating the interacting boson model by mean-field methods ," *Phys. Rev. C*, vol. 81, p. 044307, Apr 2010.

[40] E. Chabanat, P. Bonche, P. Haensel, J. Meyer, and R. Schaeffer, "A Skyrme parametrization from subnuclear to neutron star densities Part II. Nuclei far from stabilities ," *Nuclear Physics A*, vol. 635, no. 1–2, pp. 231 – 256, 1998.

[41] P. Bonche, H. Flocard, and P. Heenen, "Solution of the Skyrme HF and BCS equation on a 3D mesh ," *Computer Physics Communications*, vol. 171, no. 1, pp. 49 – 62, 2005.

[42] A. Bohr and B. R. Mottelson, *Nuclear Structure Vol. II* . Benjamin, New York, 1975.

[43] M. Bender, P.-H. Heenen, and P.-G. Reinhard, "Self-consistent mean-field models for nuclear structure ," *Rev. Mod. Phys.*, vol. 75, pp. 121–180, Jan 2003.

[44] A. Linnemann, *Das HORUS-Würfelspektrometer und Multiphononenanregungen in ^{106}Cd*. PhD thesis, Universität zu Köln, 2005.

[45] K. Krane and R. Steffen, "Determination of the E2/M1 Multipole Mixing Ratios of the Gamma Transitions in ^{110}Cd," *Phys. Rev. C*, vol. 2, pp. 724–734, 1970.

[46] K. Krane, R. Steffen, and R. Wheeler, "Directional Correlations of Gamma Radiations Emitted from Nuclear States Orientated by Nuclear Reactions or Cryogenic Methods," *Nucl. Data Tab.*, vol. 11, pp. 351–406, 1973.

[47] I. Wiedenhöver, "Programm CORLEONE," 1995. Universität zu Köln.

[48] I. Wiedenhöver, O. Vogel, H. Klein, A. Dewald, P. von Brentano, J. Gableske, R. Krücken, N. Nicolay, A. Gelberg, P. Petkov, A. Gizon, J. Gizon, D. Bazzacco, C. Rossi Alvarez, G. de Angelis, S. Lunardi, P. Pavan, D. R. Napoli, S. Frauendorf, F. Donau, R. V. F. Janssens, and M. P. Carpenter, "Detailed angular correlation analysis with 4pi spectrometers: Spin determinations and multipolarity mixing measurements in 128Ba," *Phys. Rev. C*, vol. 58, pp. 721–728, Aug 1998.

[49] H. Duckwitz, "Programm Mammel ," 2013. Universität zu Köln.

[50] R. Wirowski, M. Schimmer, L. Eßer, S. Albers, K. Zell, and P. von Brentano, "gamma-spectroscopy of ^{114}Sn with the OSIRIS-cube-spectrometer ," *Nuclear Physics A*, vol. 586, no. 3, pp. 427 – 444, 1995.

[51] C. Beausang, C. Barton, M. Caprio, R. Casten, J. Cooper, R. Krücken, B. Liu, J. Novak, Z. Wang, M. Wilhelm, A. Wilson, N. Zamfir, and A. Zilges, "The YRAST Ball array ," *Nuclear Instruments and Methods in Physics Research Section A: Accelerators, Spectrometers, Detectors and Associated Equipment*, vol. 452, no. 3, pp. 431 – 439, 2000.

[52] T. Thomas, K. Nomura, V. Werner, T. Ahn, N. Cooper, H. Duckwitz, M. Hinton, G. Ilie, J. Jolie, P. Petkov, and D. Radeck, "Evidence for shape coexistence in ^{98}Mo," *Phys. Rev. C*, vol. 88, p. 044305, Oct 2013.

[53] S. R. Lesher, C. J. McKay, M. Mynk, D. Bandyopadhyay, N. Boukharouba, C. Fransen, J. N. Orce, M. T. McEllistrem, and S. W. Yates, "Low-spin structure of ^{96}Mo studied with the (n,n'gamma) reaction ," *Phys. Rev. C*, vol. 75, p. 034318, Mar 2007.

[54] E. Williams, R. J. Casperson, V. Werner, H. Ai, P. Boutachkov, M. Chamberlain, G. Gurdal, A. Heinz, E. A. McCutchan, J. Qian, and R. Winkler, "Candidates for low-lying mixed-symmetry states in ^{140}Nd ," *Phys. Rev. C*, vol. 80, p. 054309, Nov 2009.

[55] D. Abriola and A. A. Sonzogni, "Nuclear Data Sheets A=96," *Nuclear Data Sheets*, vol. 109, p. 2501, 2008.

[56] B. Sing, "Nuclear Data Sheets A=98," *Nuclear Data Sheets*, vol. 98, p. 335, 2003.

[57] P. Petkov, J. Gableske, O. Vogel, A. Dewald, P. von Brentano, R. Krücken, R. Peusquens, N. Nicolay, A. Gizon, J. Gizon, D. Bazzacco, C. Rossi-Alvarez, S. Lunardi, P. Pavan, D. Napoli, W. Andrejtscheff, and R. Jolos, "In-band {M1} and {E2} transition rates and collective structures in ^{128}Ba ," *Nuclear Physics A*, vol. 640, no. 3–4, pp. 293 – 321, 1998.

[58] D. Heck, N. Ahmed, U. Fanger, W. Michaelis, H. Ottmar, and H. Schmidt, "Untersuchung Der Anregungszustande Des ^{96}Mo Kernes über Die Reaktion ^{95}Mo(n, gamma)^{96}Mo ," *Nuclear Physics A*, vol. 159, no. 2, pp. 49 – 80, 1970.

[59] R. A. Meyer, J. Lin, G. Molnár, B. Fazekas, A. Veres, and M. Sambataro, "Influence of cross subshell excitations on the collective states of ^{98}Mo observed by beta decay and (n,n'gamma) reaction spectroscopy ," *Phys. Rev. C*, vol. 29, pp. 1839–1858, May 1984.

[60] M. Zielińska, T. Czosnyka, J. Choiński, J. Iwanicki, P. Napiorkowski, J. Srebrny, Y. Toh, M. Oshima, A. Osa, Y. Utsuno, Y. Hatsukawa, J. Katakura, M. Koizumi, M. Matsuda, T. Shizuma, M. Sugawara, T. Morikawa, H. Kusakari, A. Efimov, and V. Mikhajlov, "Electromagnetic structure of ^{98}Mo ," *Nuclear Physics A*, vol. 712, no. 1–2, pp. 3 – 13, 2002.

[61] D. Heck, U. Fanger, W. Michaelis, H. Ottmar, and H. Schmidt, "Energy levels of ^{98}Mo excited in the (n, gamma) reaction ," *Nuclear Physics A*, vol. 165, no. 2, pp. 327 – 352, 1971.

[62] M. Pignanelli, N. Blasi, S. Micheletti, R. D. Leo, L. LaGamba, R. Perrino, J. Bordewijk, M. Hofstee, J. Schippers, S. van der Werf, J. Wesseling, and M. Harakeh, "Hexadecapole strength distributions of vibrational nuclei in the A = 100 mass region ," *Nuclear Physics A*, vol. 540, no. 1–2, pp. 27 – 56, 1992.

[63] H. L. Sharma, R. Seltz, and N. M. Hintz, "Search for an Excited Rotational Band in ^{98}Mo with the (p,t) Reaction ," *Phys. Rev. C*, vol. 7, pp. 2567–2574, Jun 1973.

[64] E. R. Flynn, F. Ajzenberg-Selove, R. E. Brown, J. A. Cizewski, and J. W. Sunier, "^{92},^{94},^{97},^{98}Mo(t,p) reactions at Et=17MeV ," *Phys. Rev. C*, vol. 24, pp. 2475–2498, Dec 1981.

[65] C. Lederer, J. Jaklevic, and J. Hollander, "In-beam gamma-ray spectroscopy of even Mo and Ru isotopes ," *Nuclear Physics A*, vol. 169, no. 3, pp. 449 – 488, 1971.

[66] M. Sambataro and G. Molnar, "Configuration mixing in Mo isotopes ," *Nuclear Physics A*, vol. 376, no. 2, pp. 201 – 212, 1982.

[67] G. Rusev, R. Schwengner, F. Donau, S. Frauendorf, L. Kaubler, L. K. Kostov, S. Mallion, K. D. Schilling, A. Wagner, E. Grosse, H. von Garrel, U. Kneissl, C. Kohstall, M. Kreutz, H. H. Pitz, M. Scheck, F. Stedile, P. von

Brentano, J. Jolie, A. Linnemann, N. Pietralla, and V. Werner, "Decay of States 1+ as a New Probe of the Structure of 0+ Shape Isomers ," *Phys. Rev. Lett.*, vol. 95, p. 062501, Aug 2005.

[68] C. D. Coster, K. Heyde, B. Decroix, P. V. Isacker, J. Jolie, H. Lehmann, and J. Wood, "Particle-hole excitations in the interacting boson model (I) General structure and symmetries ," *Nuclear Physics A*, vol. 600, no. 2, pp. 251 – 271, 1996.

[69] K. Nomura, R. Rodriguez-Guzman, L. M. Robledo, and N. Shimizu, "Shape coexistence in lead isotopes in the interacting boson model with a Gogny energy density functional ," *Phys. Rev. C*, vol. 86, p. 034322, Sep 2012.

[70] J. Jolie and H. Lehmann, "On the influence of the O(5) symmetry on shape coexistence in atomic nuclei ," *Physics Letters B*, vol. 342, no. 1–4, pp. 1 – 5, 1995.

[71] C. Fransen, N. Pietralla, Z. Ammar, D. Bandyopadhyay, N. Boukharouba, P. von Brentano, A. Dewald, J. Gableske, A. Gade, J. Jolie, U. Kneissl, S. R. Lesher, A. F. Lisetskiy, M. T. McEllistrem, M. Merrick, H. H. Pitz, N. Warr, V. Werner, and S. W. Yates, "Comprehensive studies of low-spin collective excitations in ^{94}Mo ," *Phys. Rev. C*, vol. 67, p. 024307, Feb 2003.

[72] T. Thomas, C. Bernards, J.-M. Régis, M. Albers, C. Fransen, J. Jolie, S. Heinze, D. Radeck, N. Warr, and K.-O. Zell, "The structure of ^{193}Au within the Interacting Boson Fermion Model ," *Nuclear Physics A*, vol. 922, pp. 200 – 224, 2014.

[73] R. Casten, *Nuclear Structure from a Simple Perspective*. Oxford University Press Inc., New York, 1990.

[74] T. Thomas, J.-M. Régis, J. Jolie, S. Heinze, M. Albers, C. Bernards, C. Fransen, and D. Radeck, "Bose–Fermi symmetry in the odd–even gold isotopes ," *Nuclear Physics A*, vol. 925, pp. 96 – 111, 2014.

Acknowledgments - Danksagung

An dieser Stelle möchte ich mich an die vielen Menschen wenden, denen ich die Vervollständigung dieser Arbeit verdanke.
Ich möchte Herrn Prof. Dr. J.Jolie danken für die sehr gute Zusammenarbeit, die intensive Betreuung und die Freiheit, die mir während meiner Zeit am Institut für Kernphysik gewährt wurde.
Bei Prof. Dr. A.Zilges bedanke ich mich für das Erstellen des Zweitgutachtens.
Weiterhin möchte ich mich bei Prof. Dr. V.Werner für die Gelegenheit bedanken, als Forscher über drei Monate an der Yale University arbeiten zu dürfen. Nicht nur den vielen Diskussionen habe ich viel für die Doktorarbeit zu verdanken, auch empfand ich die Zeit in New Haven als persönlich sehr bereichernd.
Ein herzliches Danke an Dr. Ch.Bernards, der mich so fürsorglich durch die Diplomarbeitszeit geführt hat. Die Summer School in Prag werde ich nie vergessen.
Ein besonderer Dank gilt Dr. St.Heinze für die vielen interessanten Diskussionen, der gemeinsamen Arbeit an den Publikationen und für arbmodel. I sincerely thank K.Nomura for his great help to calculate the molybdenum isotopes and for working together on the publications.
Bei Dr. J.-M.Régis und Dr. Ch.Fransen bedanke ich mich für die Hilfe und den Aufbau der verschiedenen Experimente in Köln und auswärts.
Bei Dr. N.Warr bedanke ich mich für die Einführung in die verschiedenen Programme und die vielen hilfreichen Ratschläge.
Für das Korrekturlesen der Doktorarbeit möchte ich mich bei Dr. Ch.Fransen, Dr. St.Heinze, D.Wilmsen und M.Dewald bedanken.
Ein großer Dank geht an meine jetzigen und ehemaligen Bürokollegen Dr. Cl.Scholl, Dr. G.Ilie, Dr. Ch.Bernards, Dr. D.Radeck, H.Duckwitz, Dr. G.Friessner für die produktiven Diskussionen und Anregungen.
Bei Prof. Dr. P. von Brentano möchte ich mich sowohl für die interessanten Diskussionen als auch für das Heranführen an die Kernstrukturphysik bedanken.
Ich danke den jetzigen und ehemaligen Mitarbeitern der Arbeitsgruppe für die tolle Atmosphäre und die gemeinsame Zeit am Institut für Kernphysik, speziell Dr. M.Hackstein, Cl.Feuerstein, Cl.Müller-Gattermann, J.Litzinger, K.Moschner, P.Thöle, D.Wilhmsen, Dr. M.Rudigier, Dr. H.Hess, Dr. B.Birkenbach, B.Siebeck, Dr. M.Pfeiffer, M.Dannhoff, M.Dewald, A.Hennig, V.Derya und Dr. A.Blazhev.
I also thank T.Ahn, M.Hinton, N.Cooper, G.Ilie for the great time in New Haven.

Großer Dank gebührt Manfred und Hildegard Wilke für die Anteilnahme an der Doktorarbeit und die Betreuung meiner Tochter in der nicht immer ganz einfachen Zeit.
Bei meinen Eltern und meiner Schwester möchte ich mich für die große Unterstützung während meiner Studienzeit und in der Endphase der Doktorarbeit bedanken.
Und bedanken möchte ich mich insbesondere bei meiner Verlobten Katharina Wilke für die gemeinsame Zeit, unsere gemeinsame Tochter und die liebevolle Unterstützung.

List of publications

"Bose-Fermi Symmetry in the Odd-even Gold Isotopes, **T. Thomas**, J.-M. Régis, J. Jolie, S. Heinze, C. Bernards, M. Albers, C. Fransen, D. Radeck, Nucl. Phys. A, in press,
DOI: 10.1016/j.nuclphysa.2014.02.002.

"Nuclear Structure of ^{193}Au within the IBFM", **T. Thomas**, C. Bernards, J.-M. Régis, M. Albers, C. Fransen, J. Jolie, S. Heinze, D. Radeck, N. Warr, K.-O. Zell, Nucl. Phys. A922, 200 (2014).

"Evidence for shape coexistence in ^{98}Mo", **T. Thomas**, K. Nomura, V. Werner, T. Ahn, N. Cooper, H. Duckwitz, M. Hinton, G. Ilie, J. Jolie, P. Petkov, D. Radeck, Phys. Rev. C88, 044305 (2013).

"Delayed gamma-ray and conversion-electron spectroscopy of A=97 fission fragments", M. Rudigier *et al.*, Phys. Rev. C87, 064317 (2013).

"Study of vibrational signatures in Ru-102", H. Duckwitz, M. Pfeiffer, M. Albers, C. Bernards, C. Fransen, J. Jolie, P. Petkov, D. Radeck, **T. Thomas**, K. Zell, Nucl. Phys. A903, 18 (2013).

"Shape dynamics in neutron-rich Kr isotopes: Coulomb excitation of Kr-92, Kr-94 and Kr-96", M. Albers *et al.*, Nucl. Phys. A899, 1 (2013).

"β-delayed γ-ray spectroscopy of 196Hg", C. Bernards, M. Elvers, D. Radeck, J. Jolie, **T. Thomas**, K. O. Zell, T. Ahn, A. Heinz, G. Illie, D. Savran, V. Werner, T. Ahmed, C. Deng, E. Jiang, R. Lee, N. Shenkov, American Physical Society, 2012 Fall Meeting of the APS Division of Nuclear Physics, 2012.

"Evidence for a Smooth Onset of Deformation in the Neutron-Rich Kr Isotopes", M. Albers *et al.*, Phys. Rev. Lett. 108, 062701 (2012).

"Recent advances in the application of dynamical supersymmetry to describe atomic nuclei", J. Jolie, Ch. Bernards, S. Heinze, J. Regis, **T. Thomas**, Journal of Physics Conference Series 366, 012023 (2012).

"Gamma gamma angular-correlation analysis of Hg-200 after cold-neutron capture", C. Bernards, W. Urban, M. Jentschel, B. Maerkisch, J. Jolie, C. Fransen, U. Koester, T. Materna, G. Simpson, **T. Thomas**, Phys. Rev. C84, 047304 (2011).

Contribution to publications essential for this thesis

Evidence for shape coexistence in ^{98}Mo:

- T.Thomas and V.Werner conceived the experiment
- T.Thomas, carried out the experiment together with T.Ahn N.Cooper, M.Hinton, and G.Ilie
- T.Thomas carried out the data analysis with V.Werner, H.Duckwitz, P.Petkov, and D.Radeck
- K.Nomura performed the model calculations
- T.Thomas wrote the paper, K.Nomura, J.Jolie, and V.Werner cowrote the paper

Nuclear Structure of ^{193}Au within the IBFM:

- J.M.Regis conceived the experiment
- J.M.Regis carried out the experiment together with M.Albers, C.Bernards, C.Fransen, D.Radeck
- T.Thomas, C.Bernards, and J.M.Regis carried out the data analysis
- T.Thomas performed the model calculations together with J.Jolie, S.Heinze, and N.Warr
- T.Thomas wrote the paper

Bose-Fermi Symmetry in the Odd-even Gold Isotopes:

- J.M.Regis conceived the experiment
- J.M.Regis carried out the experiment together with M.Albers, C.Bernards, C.Fransen, D.Radeck
- T.Thomas,J.M.Regis carried out the data analysis
- T.Thomas performed the model calculations together with J.Jolie and S.Heinze
- T.Thomas wrote the paper

Erklärung

Ich versichere, dass ich die von mir vorgelegte Dissertation selbständig angefertigt, die benutzten Quellen und Hilfsmittel vollständig angegeben und die Stellen der Arbeit - einschließlich Tabellen, Karten und Abbildungen -, die anderen Werken im Wortlaut oder dem Sinn nach entnommen sind, in jedem Einzelfall als Entlehnung kenntlich gemacht habe; dass diese Dissertation noch keiner anderen Fakultät oder Universität zur Prüfung vorgelegen hat; dass sie - abgesehen von unten angegebenen Teilpublikationen - noch nicht veröffentlicht worden ist, sowie, dass ich eine solche Veröffentlichung vor Abschluss des Promotionsverfahrens nicht vornehmen werde. Die Bestimmungen der Promotionsordnung sind mir bekannt. Die von mir vorgelegte Dissertation ist von Herrn Prof. Dr. Jan Jolie betreut worden.

Teilpublikationen

"Bose-Fermi Symmetry in the Odd-even Gold Isotopes", T. Thomas *et al.*, Nucl. Phys. A925, 96 (2014).

"Nuclear Structure of ^{193}Au within the IBFM", T. Thomas *et al.*, Nucl. Phys. A922, 200 (2014).

"Evidence for shape coexistence in ^{98}Mo", T. Thomas *et al.*, Phys. Rev. C88, 044305 (2013).

"Recent advances in the application of dynamical supersymmetry to describe atomic nuclei", J. Jolie, Ch. Bernards, S. Heinze, J. Regis, T. Thomas, Journal of Physics Conference Series 366, 012023 (2012).